Novel Lanthanide Containing Polymers for Nucleic Acid Delivery and Study of Polyplex Dynamics

Sneha Sanjay Kelkar

Dissertation submitted to the faculty of the Virginia Polytechnic Institute and State University in partial fulfillment of the requirements for the degree of

Doctor of Philosophy

In

Chemistry

Theresa M. Reineke

S. Richard Turner

Kevin J. Edgar

Robert B. Moore

Webster L. Santos

12/07/2012
Blacksburg, Virginia

Keywords: lanthanide polymers, NMR, LRET, nucleic acid delivery, theranostic agents, polyplexes

Novel Lanthanide Containing Polymers for Nucleic Acid Delivery and Study of Polyplex Dynamics

Sneha Sanjay Kelkar

ABSTRACT

Nucleic acid therapy holds real promise to offer less severe (lower side effects) as a treatment for life threatening and difficult to treat diseases such as cancer, heart disease or Alzheimer's disease. Theranostic nanomaterials that combine diagnostic imaging and therapeutic delivery, have potential to minimize the amount of time and dosage required for the treatment. This is achieved *via* delivery of nanoparticles that carry therapeutic payload as well as imaging agents; these agents need to circulate in the body longer due to its (larger) size and selectively accumulate in the tumor regions through the enhanced permeability and retention (EPR) effect.

We have designed novel lanthanide (Gd, Tb or La) containing polymers with oligoethyleneamine and lanthanide chelating units to incorporate DNA binding and imaging agent functionality. Protonable amines along the polymer backbone electrostatically interact with DNA and compact it into a nanoparticle. These nanoparticles can be imaged both *in vivo* (Gd analogues, magnetic resonance imaging) and intracellularly (Tb chelation, fluorescence spectroscopy). Polymers were synthesized via step-growth polymerization to achieve a degree of polymerization of 18-24 for different analogues with varying amine number (three to six, N3-N6) along the backbone.

Dynamic light scattering performed on the polyplexes (polymer-DNA complexes) indicate that they are in nanometer size range (50-80nm). All the polymers used to form polyplexes exhibited low toxicity to cultured human Glioblastoma cells (U-87) and showed variable transfection efficiency dependent on structure, comparable to G4 (sold as Glycofect™), a commercial transfection agent previously developed in our lab.

This dissertation describes the first studies by the Reineke lab to monitor polyplex formation and destabilization using lanthanide resonance energy transfer (LRET). Polyplexes were formulated with Tb chelated N5 polymer and tetramethyl rhodamine (TMR) labeled pDNA, which are "LRET pairs". We observed decrease in luminescence intensity of Tb polymer (donor) in close proximity of TMR DNA (acceptor) in an intact polyplex at different N/P ratios. However, upon destabilization of polyplexes by addition of salt or heparin solution, the increase in distance between donor and acceptor resulted in increase in the luminescence intensity of Tb polymer. With the LRET technique, we are able to monitor formation and destabilization of polyplexes by monitoring change in luminescence of the donor chromophore (Tb).

Polyplexes formulated with non-paramagnetic analogues (La chelated) of N4, polyethyleneimine (PEI) and G4 were studied using NMR to quantify free vs. bound polymer in a formulation. The amount of free polymer was measured by integrating the broad resonances from nanometer-sized particles (polyplexes) with narrow peaks from free polymer chains. This was supported by using an internal reference method to quantify free polymer amount from known internal reference concentration. We observed an increase in the amount of free polymer with N/P ratio for all three systems and both the methods showed comparable results.

Acknowledgements

First, I would like to thank my advisor Dr. Theresa Reineke, for her great mentorship and advising in my research. I would like to thank her for pushing me through tough times and having faith in my abilities and me. My co-advisor Dr. Richard Turner has been a great mentor to me as well, I learned a lot about polymer chemistry as well as professional leadership from him. It was great experience working with Turner group for past one and half year and thanks to Alice, Xu, Julie, Bin, Kevin and Jermaine for daily help and discussions. The past one year would have been difficult without labmates like you guys!

I would also like to thank my committee members Dr. Kevin Edgar, Dr. Robert Moore, and Dr. Webster Santos for their constructive comments and encouragement on my research and technical skills. Thanks to Dr. Lou Madsen for being great advisor on NMR project and for helping me understand fundamentals of NMR and MRI. It has been pleasure working with Cocoa; she is a dedicated and hard working student.

Special thanks to Dr. Paul Deck, my academic graduate advisor, Angie Miller, Joli Hyunh and entire chemistry department staff for all the help on countless occasions during past five years. Senior and former graduate students- Josh, Anton, Karina, Giovanna, Patrick and Vijay from Reineke lab were great mentors to me and have taught me hundreds of things. Special thanks to Nilesh and Swapnil for helping me from University of Minnesota whenever I needed some lab supplies. Younger and newer members of the Reineke group hold great promise for our research. Good luck to Yaoying, Dustin, Lian. Haley, Will, Jeff and Swapnil for leading our research in future

direction. Our postdocs- Kevin, Nilesh, Mallory, Zach and Tushar have been great with their suggestions and willingness to help. I would like to thank former members of our group Daniel and Hao for their great friendship.

My family and friends have provided very strong support in life and in my career. I cannot thank them enough! I will always be grateful to my parents, Kamal and Sanjay Kelkar and my brother Kaustubh for their tremendous support in every endeavor of my life. Special thanks to Sidd for tremendous friendship, care and support he always gave me. Thanks for always being there for me. Finally, I would like to thank funding agencies- National Science Foundation, Camille Dreyfus Teacher Scholar Award Program and Department of Chemistry at Virginia Tech for funding my research and academic studies.

Table of Content

Table of Figures

List of Tables

Table of Abbreviations

CT: computed tomography
DLS: Dynamic Light Scattering
DMEM: Dulbecco's Modified Eagle Medium
DMSO: Dimethyl sulfoxide
DOX: doxorubicin
DTPA: Diethylene triamine pentaacetic acid
EDTA: Ethylene diamine tetraacetic acid
EGFP: enhanced green fluorescent protein
EPR: Enhanced permeability and retention
FBS: Fetal bovine serum
FCS: fluorescence correlation spectroscopy
FRET: Fluorescence resonance energy transfer
HER: human epidermal growth factor receptor
LRET: Lanthanide resonance energy transfer
MRI: magnetic resonance imaging
MTBE: Methyl-tert butyl ether
NMR: nuclear magnetic resonance
ON: Oligonucleotide
PDI: polydispersity index
PDT: Photodynamic therapy
PEG: polyethyleneglycol
PEI: polyethyleneimine
PET: positron emission tomography
PGAA: poly(glycoamidoamine)
PLA: Poly(L-lactide)
PLL: poly(L-lysine)
QD: quantum dots
QELS: Quasi elastic light scattering
RLU: relative light unit
SEC: size exclusion chromatography
SPECT: Single-photon emission computed tomography
TAE: Tris-acetate EDTA
TMR: tetramethyl rhodamine

Chapter 1 : Theranostics: Combining Imaging and Therapy*

*This chapter is published in **Bioconjugate Chemistry** (2011), 22(10), 1879-1903.

Abstract

Employing theranostic nanoparticles that combine both therapeutic and diagnostic capabilities in one dose, for the treatment of debilitating diseases has promise to propel the biomedical field towards personalized medicine. This review presents an overview of different theranostic strategies developed for the diagnosis and treatment of disease and we have focused on cancer. Here in, therapeutic strategies such as nucleic acid delivery, chemotherapy, hyperthermia (photothermal ablation), photodynamic, and radiation therapy that are combined with one or more imaging functionalities are discussed for both *in vitro* and *in vivo* studies. Different imaging probes such as MRI contrast agents (T_1 and T_2 agents), fluorescent markers (organic dyes and inorganic quantum dots), and nuclear imaging agents (PET/SPECT agents) can be decorated onto therapeutic agents or therapeutic delivery vehicles in order to image and gain information about the trafficking pathway, kinetics of delivery, and therapeutic efficacy and several strategies are outlined. The creative approaches being developed for these classes of therapies and imaging modalities are discussed, and the recent developments in this field along with examples of technologies that hold promise for the future of cancer medicine are highlighted.

1.1 Introduction

The term "theranostic" was coined in 2002 by Funkhouser[1] and is defined as materials that combine the modalities of therapy and diagnostic imaging, meaning that theranostics deliver therapeutic drug and diagnostic imaging agents at the same time within the same dose. Before initiating treatment of various diseases such as cancer, it is essential to carry out diagnostic

imaging to understand the cellular phenotype(s) and heterogeneity of the tumor.[2-4] In contrast to the development and use of separate materials for these two objectives, theranostics combine these features into one 'package', which has the potential to overcome undesirable differences in biodistribution and selectivity that currently exist between distinct imaging and therapeutic agents. The ultimate goal of the theranostic field is to gain the ability to image and monitor the diseased tissue, delivery kinetics, and drug efficacy with the long-term hope of gaining the ability to tune the therapy and dose with heretofore unattainable control. Individualizing medicine, as opposed to adopting a 'one size fits all' approach, can move the field of nanomedicine forward towards an era of more personalized treatment approaches.[5]

One of the most promising aspects of utilizing nanoparticles for therapeutics, diagnostics, and theranostics is their potential to localize (or be targeted) in a specific manner to the site of disease and circumvent the possible numerous side effects. The nanoscopic size of these materials precludes them from being readily cleared through the kidneys, thereby extending circulation in the blood pool depending on their surface functionalization characteristics. Also, when considering novel cancer treatments, the blood vessels in many tumors types have been found to be irregular in shape, dilated, leaky, and the endothelial cells have large fenestrations. Due to altered anatomy of the tumor vessels, nanosized particles can easily permeate through the tumor tissues from the blood pool and be retained in the tumor due to poor lymphatic drainage. This phenomenon of selective accumulation of nanosized particles near tumor tissues compared to healthy ones is termed as the enhanced permeability and retention effect (or EPR effect).[6,7] Additionally, nanoparticles have high surface area-to-volume ratios, and yield in their high loading capacity for therapeutic drugs and imaging agents. They can also be surface functionalized with targeting ligands and cloaking agents like poly(ethylene glycol) (PEG).

Introduction of a targeting ligand may help to increase the target-to-background contrast in imaging and can improve the local concentration of the therapeutic at the target of interest, with the goal of reducing systemic toxicity.

In this review, we present an overview of some of the theranostic strategies developed for different types of cancer treatments, such as nucleic acid therapy, chemotherapy, hyperthermia treatment, photothermal ablation, photodynamic therapy, and radiation therapy. This review discusses syntheses and developmental studies of the novel multifunctional materials employed in this work, including linear and branched polymers, dendrimers, micelles, inorganic nanoparticles, and protein conjugates. In addition to their therapeutic uses, these materials have been functionalized with imaging agents to promote one or more diagnostic imaging techniques, such as magnetic resonance imaging, nuclear imaging (PET/SPECT/CT), and/or fluorescence imaging/optical imaging.

1.2. Theranostic Delivery Vehicles for Nucleic Acid Therapeutics

Nucleic acid therapy holds promise in the treatment of both acquired and inherited diseases like Alzheimer's disease, cancer, adenosine deaminase deficiency, and cystic fibrosis. In addition to traditional 'gene therapy,' in which a defective copy of a gene is replaced with a functional (therapeutic one), other forms of nucleic acids exist as current and potential therapeutics, such as plasmids, antisense oligonucleotides, ribozymes, DNAzymes, aptamers, and small interfering RNA (siRNA). These polynucleotides can alter gene expression at the transcriptional or post-transcriptional level and may be effective to treat cancer, cardiovascular, inflammatory and some forms of infectious diseases. The success of polynucleotide therapeutic modalities relies on their efficient delivery to the site of disease. Nucleic acids are large, negatively-charged molecules that are highly susceptible to enzymatic degradation; they are not

easily internalized by cells that contain a negatively-charged plasma membrane. Injection of naked nucleic acids directly to the diseased areas (such as skeletal muscles, liver, thyroid, heart muscle, urological organs, skin, and tumor) via a physical method—such as electroporation, a 'gene gun,' or ultrasound—can be an effective mode of delivery.[8] However, systemic injection of naked DNA is largely ineffective due to the minimal amount of intact polynucleotide reaching the final intracellular destination. Direct injection of naked DNA holds limited promise towards efficient delivery, especially to the targets that are anatomically inaccessible (e.g., solid tumors).

Over the last several decades, tremendous effort has been put forth to design and develop delivery methods to produce highly efficient and efficacious delivery vehicles. These methods involve both viral and non-viral delivery vehicles. Virus-based therapeutic delivery involves the inactivation of viral genes that cause disease and incorporation of a copy of the therapeutic gene of interest—as RNA for retroviral and lentiviral vectors or as DNA for adenoviral or adeno-associated viral vectors.[9] Viral vectors can achieve high transfection efficiency and can achieve integration of the target gene into the chromosomal DNA of the recipient cell(s). Several clinical trials[10,11] with viral vectors have raised concerns due to undesirable interference with the host genome and the potential to elicit a severe immune response. To this end, in recent years, many researchers have focused on development of new synthetic, non-viral vehicles, which have the potential to be non-toxic, less immunostimulatory, and can be more versatile for modification and carrying different types of drug payloads. Non-viral vehicles based on synthetic polymers, dendrimers, liposomes, cell-penetrating peptides and inorganic nanoparticles have been developed and studied in detail.[8,12,13] These types of vehicles also possess the advantageous ability to be easily modified for theranostic purposes.

To design highly efficient gene delivery vectors, identification of the rate-limiting steps involved in the path of the delivery vehicle from its site of administration to the target of interest is crucial for success. Understanding trafficking of a nucleic acid from extracellular matrix, through the cell, and into the nucleus has traditionally been done by labeling the nucleic acid with one or more fluorescent dyes and monitoring co-localization signals with a fluorescent-labeled organelle at different time points. For example, Godbey et al.[14] investigated the intracellular trafficking of poly(ethyleneimine) (PEI) and PEI-DNA complexes (polyplexes) to the nucleus with the help of confocal laser scanning microscopy. PEI and DNA were labeled with Oregon Green® 488 and rhodamine, respectively, and the yellow signal resulting from co-localization of green (PEI) and red (DNA) was monitored to understand trafficking of PEI-DNA complexes. They also studied trafficking of PEI and DNA individually by monitoring green and red fluorescence signals, respectively. They investigated the PEI-DNA polyplexes after endocytosis as well, revealing that, for example, PEI enters the nucleus along with the DNA. One of the major limitations of this approach for visualization (that is, separate labeling of polymer and DNA with fluorescent dyes and monitoring co-localization signal with fluorescent spectroscopy) is inherently low spatial resolution associated with the confocal microscopy technique. Fluorescence signals from each fluorophore may overlap in spite of the polymer and DNA not actually being associated with each other; that is, this approach is unable to provide potentially valuable details, such as more precise, real-time information about association-dissociation of the polymer from the polynucleotide.[15,16]

Recent studies in which both the delivery vehicle and DNA were labeled with organic dyes have allowed the use of more sophisticated imaging techniques, such as time-lapse microscopy, fluorescence resonance energy transfer (FRET),[17,18] and fluorescence correlation

spectroscopy (FCS).[19] These approaches hold promise to provide more precise information regarding polyplex trafficking and dissociation and towards development of theranostic systems. For example, Lucas et al.[16] used dual-color fluorescence fluctuation spectroscopy (FFS) to monitor complexes comprised of Cy5-labeled poly(L-lysine) (PLL) and rhodamine-labeled oligonucleotide (ON). FFS possesses high spatial and temporal resolution, which permits an enhanced ability to differentiate between associated and dissociated polyplexes. The authors' use of FFS led to novel and interesting findings, such as the observation that high molecular weight PLL (1700 kDa) dissociates from ON within the cytoplasm without entering the nucleus, whereas low molecular weight PLL (30 kDa) releases ON after nuclear entry.

Despite successes such as this, there remain several limitations associated with the use of fluorescent dyes for labeling the polymeric vehicle—such as photobleaching, fast fluorescence decay, and non-uniform labeling of the polymer.[20] Further, some research has also indicated that labeling the polymer with a fluorescent label can change its physiochemical properties. For example, Remaut et al.[21] have shown with the help of fluorescence corelational spectroscopy (FCS) that diblock PEI-PEG polymers lose their ability to bind to nucleic acids when labeled with a fluorescent dye, such as Cy5. For these reasons, other labeling strategies are being widely investigated to further improve understanding of delivery vehicle trafficking.

One set of well-studied alternative labeling agents are quantum dots (QDs). Advantages of QDs over fluorescent dyes include their high extinction coefficients, strong control over optical properties, and reduced susceptibility to photobleaching.[20,22] Many QDs form FRET pairs with fluorescent organic dyes and are useful for monitoring polyplex trafficking *in vitro*. FRET is a highly sensitive technique that provides information about intracellular interactions on the nanometer scale. Upon its excitation, the emission of one fluorescent species serves to excite

a second species. Given the short distance over which the emission can propagate detection of emission from the second species serves as a strong indicator of the close proximity (that is, molecular interaction) between the two indicators. When these two indicators are attached to separate molecules, a positive FRET signal (emission of the second indicator) is evidence of physical association of these two molecules at the time of signaling.

As an example, Ho et al.[15] have demonstrated that the intracellular dissociation of polymer-pDNA complexes can be monitored via QD-FRET (Figure 1.1). In this study, streptavidin-functionalized, Cy5-labeled chitosan was conjugated to QD-labeled pDNA via biotin-streptavidin binding. QD-FRET analysis was performed using electron and confocal microscopy at 24, 48 and 72 h post transfection in HEK293 cells to study unpackaging of chitosan-pDNA complexes. Their investigation indicated that at 24 h after transfection, polyplexes were localized in the perinuclear region, whereas at 72 h post-transfection, polyplexes were dissociated and DNA was located in the nucleus without any signal from chitosan (Cy5).

(a) (b)

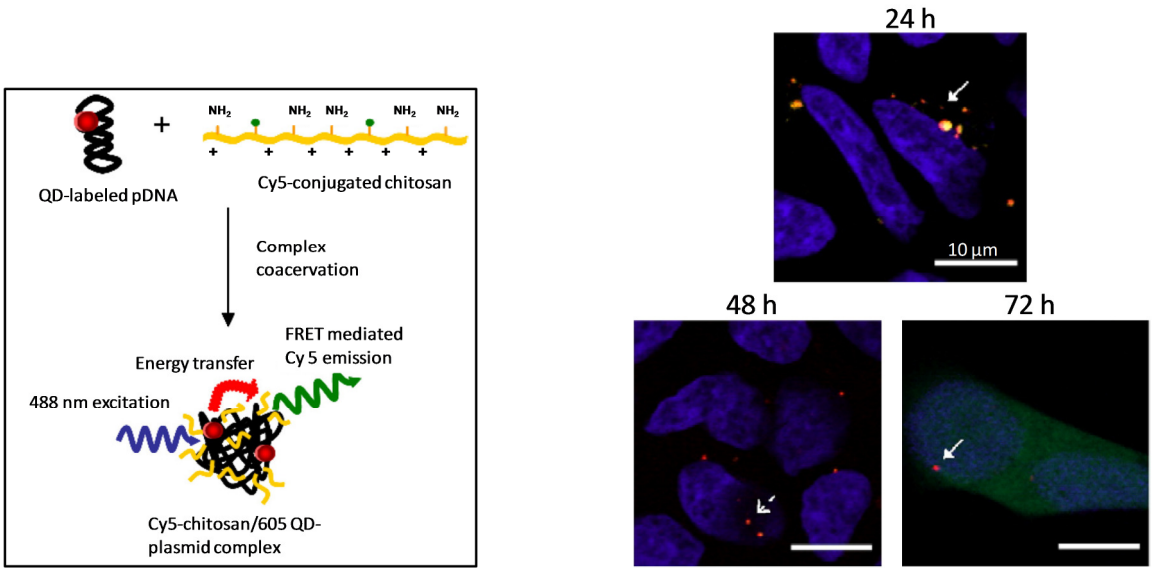

Figure 1-1:(a) Condensation of DNA and chitosan polymer to form compact nanocomplexes. Association of DNA and polymer was indicated by sensitized FRET signal from Cy5 upon excitation of QD-labeled DNA. (b) Confocal images showed localization of intact chitosan-DNA complexes (indicated by sensitized FRET signal from Cy5 in yellow/orange color) in the perinuclear region at 24 h, while the onset of DNA release (red) and its trafficking to the nucleus (blue) was observed at 48 h and 72 h post transfection (absence of Cy5 signal).

Figure reprinted from Ho, Y.-P.; Chen, H. H.; Leong, K. W.; Wang, T.-H. Evaluating the intracellular stability and unpacking of DNA nanocomplexes by quantum dots-FRET, *J. Controlled Release* 2006, *116*, 83-89 with permission, Copyright Elsevier (2006).

Commonly used techniques to visualize RNA interference (RNAi) experiments are co-transfection of an siRNA with a fluorescent reporter gene (to monitor degree of reporter gene knockdown) and/or end-modification of a covalently attach a fluorophore to the sense strand on the siRNA. Although above mentioned strategies posses some utility, these techniques are limited in that they are best suited for highly silenced genes and ignore moderately-silenced

gene, which might be of interest in some cases. Further, current transfection methods are incapable of discriminating among multiple siRNA molecules delivered simultaneously.. Additionally, QDs do not photobleach and have longer fluorescene lifetime compared to organic dyes. As an example, Bhatia and coworkers[23,24] synthesized near-infrared (NIR) QDs (emission max 655 nm or 705 nm) functionalized with PEG and amino groups and attached with an siRNA (designed to knockdown expression of enhanced green fluorescent protein (EGFP)) and a cell-targeting moiety (tumor-homing F3 peptide; Figure 1.2) via reducible disulfide (sulfo-LC-SPDP) or non-reducible (sulfo-SMCC) linkers. The F3-peptide and siRNA were attached to the surface of the QD via reducible or non-reducible linkers and their effect on cell internalization and gene knockdown was compared. The resulting molecule was transfected into cultured cells with Lipofectamine™ 2000, a commercially-available transfection reagent, and the EGFP expression was monitored by measuring the fluorescence intensity using flow cytometry.The use of reducible versus non-reducible cross-linker for the F3 peptide did not affect the cell internalization. However, use of reducible disulfide linker (sulfo-LC-SPDP) for siRNA showed significantly higher gene knockdown, possibly due to change in interaction of siRNA with the RNA induced silencing complex through release of the siRNA from the particle surface.

(a) (b)

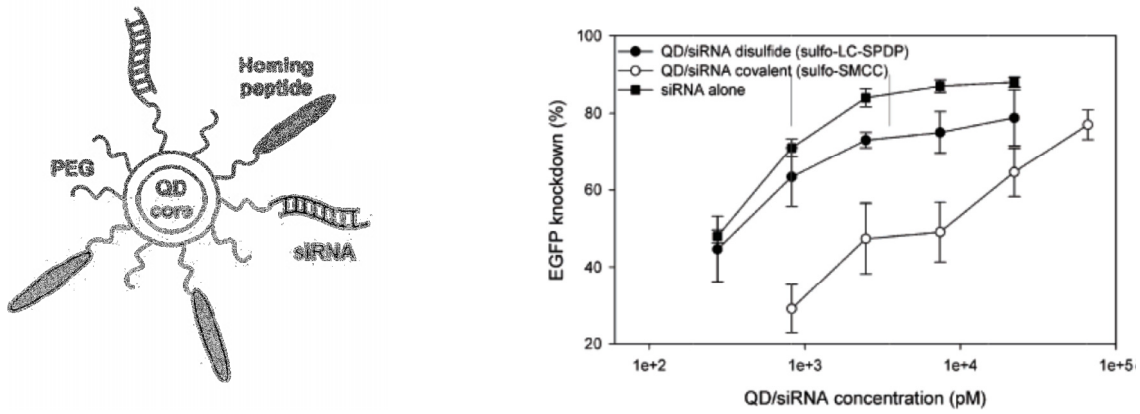

Figure 1-2: (a) Schematic representation of siRNA containing QD nanoparticles decorated with PEG and a targeting peptide. (b) Significantly greater EGFP knockdown was observed for the QD/siRNA complexes containing the reducible disulfide (sulfo-LC-SPDP) linker versus the non-reducible (sulfo-SMCC) linker.

Figure reprinted from Derfus, A. M.; Chen, A. A.; Min, D.-H.; Ruoslahti, E.; Bhatia, S. N., (2007*)* Targeted Quantum Dot Conjugates for siRNA Delivery. *Bioconjugate Chem. 18,* 1391-1396 with permission from the American Chemical Society (ACS).

In another example, Tan et al.[25] have developed a 'self-tracking' siRNA delivery vehicle based upon chitosan-coated quantum dots (green fluorescent CdSe/ZnS) as a core. The negatively charged QD was coated with positively charged chitosan via electrostatic attraction and the surface of chitosan was complexed with negatively charged siRNA against human epidermal growth factor receptor 2 (HER2) to promote delivery of the nanoparticles to breast cancer cells (SKBR3 cells) in which HER2 is upregulated; a variation of these nanoparticles was also coated with an anti-HER2 antibody (via standard EDC/NHS chemistry). Cellular uptake studies were performed and confocal microscopy on both SKBR3 and MCF-7 (HER2 under-expressed) cell lines to validate the targeting efficacy of the HER2-targeting moiety on the

nanoparticles in cellular uptake and target gene knockdown (Figure 1.3). The QD was encapsulated to probe the delivery of the siRNA-carrier system.

(a) (b)

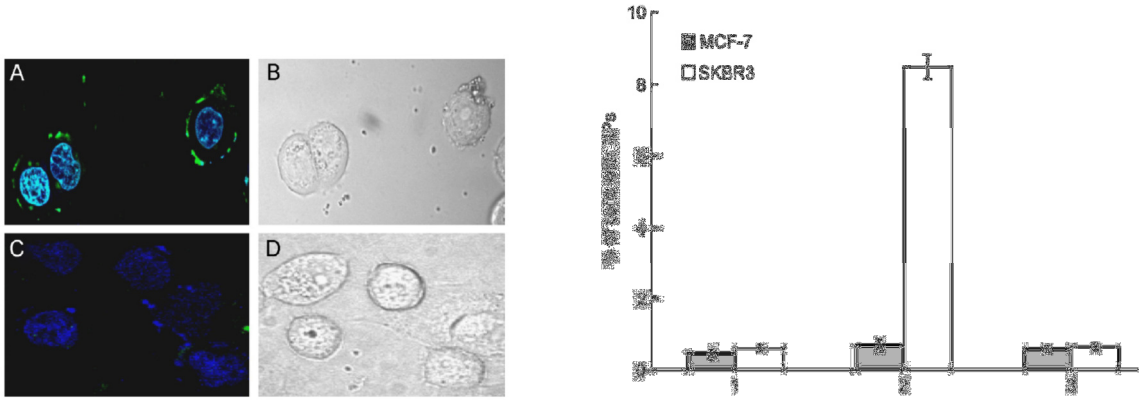

Figure 1-3: (a) Laser confocal microscopy images of SKBR3 cells showing HER2 siRNA-containing chitosan-QD nanoparticles (cyan) with (A) and without (C) anti-HER2 antibody labeling (green). Corresponding bright field microscopy images are shown in (B) and (D); (b) Cellular uptake of chitosan-QD-siRNA nanoparticles labeled with HER2-targeting antibody in SKBR3 and MCF-7 cell lines. "1" denotes control cell populations, "2" denotes cells exposed to HER2-targeted chitosan-QD-siRNA nanoparticles, and "3" denotes cells exposed to non-targeted chitosan-QD-siRNA nanoparticles. The role of HER2 targeting is revealed by the enhanced uptake of "2" by SKBR3 cells (vs. MCF-7).

Figure adapted from Tan, W. B.; Jiang, S.; Zhang, Y. Quantum-dot based nanoparticles for targeted silencing of HER2/neu gene via RNA interference, *Biomaterials* 2007, *28*, 1565-1571 with permission, Copyright Elsevier (2007).

Prigodich et al.[26] have developed nanoconjugates that can both detect and regulate intracellular mRNA levels via monitoring an increase in fluorescence of a 'flare' that is released upon successful binding of a therapeutic oligonucleotide to its target mRNA (Figure 1.4a).

Nanoconjugates containing gold nanoparticles were functionalized with a therapeutic antisense oligonucleotide (a chimera of DNA and a 'linked nucleic acid' (LNA)) which binds to a specific region of an mRNA suppressing expression of survivin, a well-known gene for cancer diagnosis and treatment. An additional complementary short oligonucleotide labeled with Cy5 was conjugated onto the nano-flare that is released upon binding to the target mRNA, thereby increasing the Cy5 fluorescence intensity. The mRNA detection technique is rapid (reaches completion in 10 min) and sensitive for single-base pair mismatch recognition. These nanoflares deplete mRNA levels in sequence- and dosage-dependent manners and, consequently, hold promise towards mRNA-directed theranostics (Figure 1.4b).

(a) (b)

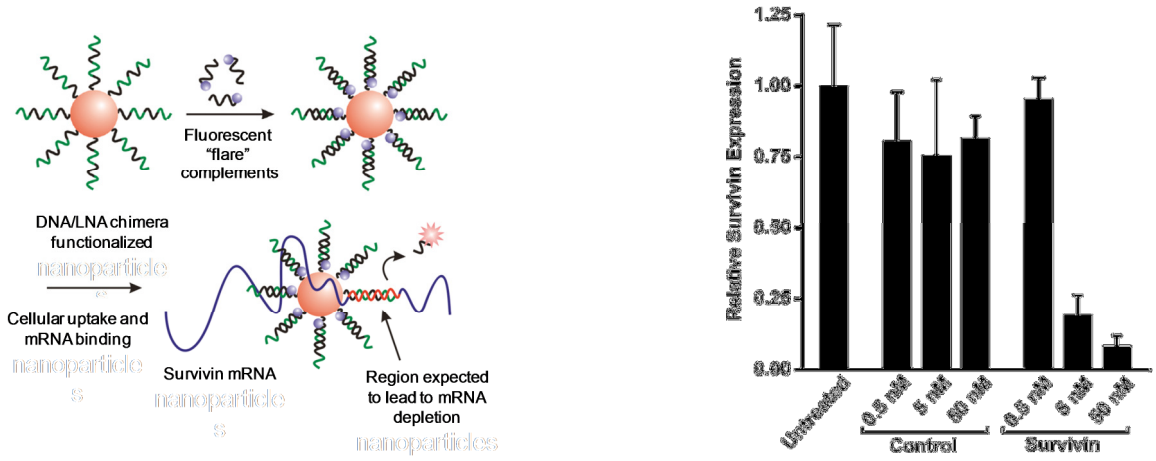

Figure 1-4: (a) Schematic of antisense oligonucleotide delivering gold-nanoconjugates. (b) RT-PCR mRNA knockdown results for control and therapeutic (survivin) oligonucleotide delivery into the HeLa cells normalized to untreated cells. Dosage dependent knockdown was observed for survivin and no significant knockdown for controls at high therapeutic dosage.

Figure adapted from Prigodich, A. E.; Seferos, D. S.; Massich, M. D.; Giljohann, D. A.; Lane, B. C.; Mirkin, C. A., (2009) Nano-flares for mRNA regulation and detection. *ACS Nano 3,* 2147-2152 with permission from ACS.

Our group has developed a new set of theranostic polymers for the combined delivery of nucleic acids and magnetic resonance imaging (MRI). [27] The macromolecule structures contain a lanthanide-binding domain (diethylenetriamine pentaacetic acid or DTPA) and an oligoethyleneamine (PEI-like) domain that contain secondary amines, which are protonated at physiological pH and promote binding and compaction of nucleic acids into polyplexes (Figure 1.5a). The flexibility in this platform is that the lanthanide-binding domain can be chelated to either gadolinium (Gd), an MRI contrast agent for sub-μm to mm scale imaging or luminescent europium (Eu) for visualization on the nm-μm scale, which can be imaged with fluorescence microscopy. These polymeric delivery vehicles integrate both therapeutic delivery and diagnostic imaging functionalities into one system. Plasmid DNA (pDNA) transfection studies performed on polyplexes formed with these delivery beacons reveal that the Gd^{3+}-containing analogues show high image contrast (compared to untransfected cells) and Eu^{3+} analogues can be imaged with fluorescent microscopy inside the cell (Figure 1.5b and 1.5c). These polyplexes formed with these polymer beacons showed high cell internalization efficiency and a low toxicity profile, and they hold promise to individually monitor both the nucleic acid and the polymer vehicle during the delivery process. The use of a lanthanide metal instead of other common fluorescent markers (i.e. fluorescent dyes) eliminates concerns related to photobleaching and non-uniform labeling. Also, the long luminescence lifetime (on the order of milliseconds) characteristic of the lanthanides enables easy removal of background fluorescence via time-delayed measurements. Moreover, these lanthanides are known to form FRET pairs with some fluorescent dyes, such as tetramethyl rhodamine (TMR), Cy5, and some APC (allophycocyanin) dyes, which may be beneficial to monitor kinetics of polyplex association-dissociation via FRET. Current efforts are directed towards studying the effects of an increase in amine stoichiometry on transfection

efficiency and toxicity and monitoring complex unpackaging via FRET with terbium- (Tb^{3+}-) containing analogues of these polymers.

(a)

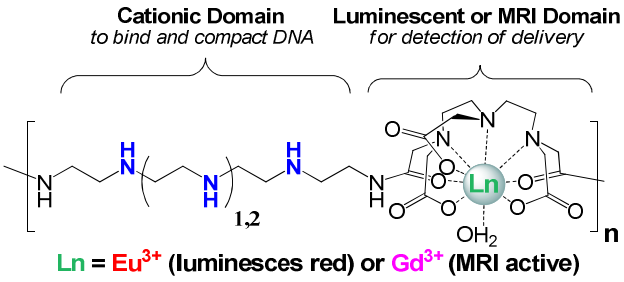

(b)

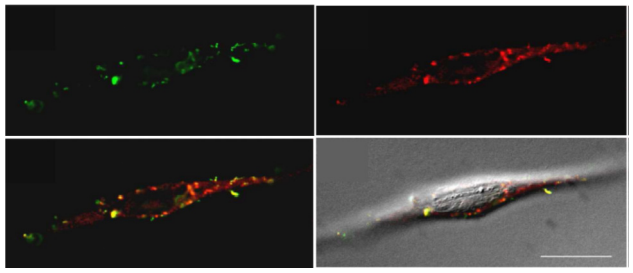

(c)

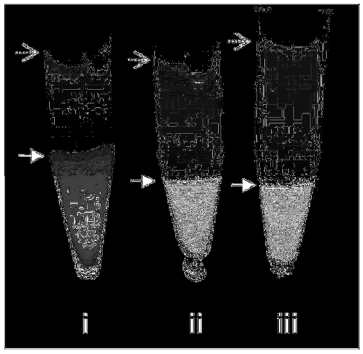

Figure 1-5: (a) The chemical structure of lanthanide- and oligoethyleneamine-containing theranostic polymers for nucleic acid delivery. (b) Deconvoluted confocal microscopy images of HeLa cells transfected with polyplexes containing Eu^{3+}-chelated polymer (red) and fluorescein isothiocyanate- (FITC-) labeled pDNA (green), and their overlay with DIC (differential interference contrast), shows accumulation of polyplexes in the perinuclear region and in cytoplasm. (c) Magnetic resonance (MR) images of cells transfected with two different Gd-containing polymers, (ii) and (iii), compared to untreated HeLa cells, (i).

Figure adapted from Bryson, J. M.; Fichter, K. M.; Chu, W.-J.; Lee, J.-H.; Li, J.; Madsen, L. A.; McLendon, P. M.; Reineke, T. M., (2009*)* Polymer beacons for luminescence and magnetic

resonance imaging of DNA delivery. *Proc. Natl. Acad. Sci. U. S. A. 106,* 16913-16918. Copyright (2009) National Academy of Sciences, U.S.A

Several interesting examples of *in vivo* administration of theranostics containing nucleic acid therapies have been reported previously; these materials are useful for the study of pharmacokinetic and biodistribution profiles of both the medicinal agent and the vehicle *in vivo*. Similar to the *in vitro* imaging discussed above, several labeling agents can be conjugated to the delivery vehicle and used for *in vivo* diagnostic imaging. Imaging agents such as NIR quantum dots (optical imaging), magnetic resonance contrast agents (MR imaging), and PET/SPECT (positron emission tomography/single photo emission computerized tomography) agents can be incorporated into the delivery system. Each of these imaging modalities has its advantages and disadvantages. For example, while MRI has good spatial resolution (10-100 μm), it is hampered by low sensitivity (micromolar quantities of paramagnetic agent must be used to see significant change in signal). Nuclear imaging techniques such as PET and SPECT imaging possess high sensitivity but are limited by low spatial resolution. Additionally, generating radionuclides in the cyclotron is expensive and exposure to ionizing radiation can be harmful in the long term.

In the case of MRI, to obtain high image contrast, significant accumulation of the contrast agents at the target site is necessary. This can be achieved by functionalizing contrast agents with suitable ligands that target various cell receptors, such as transferin receptor, folate receptor, and human/epidermal growth factor receptor 2, upregulated on the surface of various cancer cells. Both T_1 (positive) and T_2 (negative) contrast agents can be employed within theranostic materials. For *in vitro* imaging, iron oxide-based nanoparticles (T_2 contrast agents) have been used and are discussed herein. Additionally, these particles can be functionalized with targeting ligands like human holo-transferin that are covalently attached to the dextran-coated

monocrystalline iron oxide (Tf-MION) or cross-linked iron oxide (Tf-CFIO) and can easily be taken up by cells via receptor-mediated endocytosis.[28-30]

Park et al[31] developed magnetic iron oxide-based nanoarchitectures that allow assessment of polyplex dissociation via tracking of changes in T_2 relaxation rates. Poly(ethyleneimine) (Branched PEI, MW 10 kDa) that can bind to DNA via electrostatic interactions was covalently conjugated to ultrasmall superparamagnetic iron oxide to form higher-order structures (size ~ 100 nm). A 'T_2 relaxation switch' (Figure 1.6a) was proposed as a tool for monitoring packaging and unpackaging of the polyplexes. When complexed with DNA, the nanoparticle carriers show longer T_2 relaxation times; conversely, upon dissociation, they reduce back to original values (Figure 1.6b). Salt (sodium chloride)-induced polyplex dissociation was studied via three different methods: (i) YOYO dye exclusion, (ii) turbidity measurement, and (iii) decrease in T_2 relaxation time. Plasmid-containing ultrasmall superparamagnetic iron oxide- PEI nanoparticles were less toxic to HeLa cells than PEI only (for 10 kDa and 25 kDa molecular weights at the same net PEI concentration) and showed higher luciferase gene expression (at N/P 15) than PEI alone.

(a)

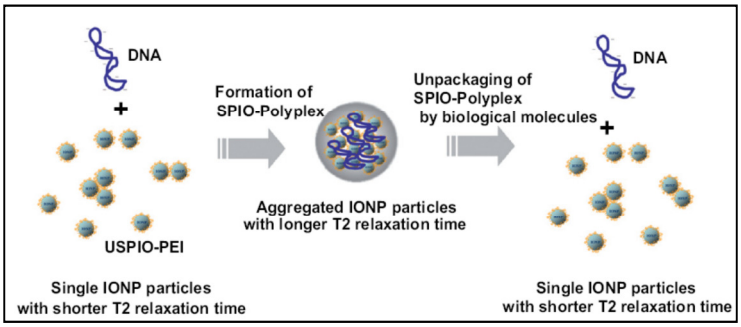

(b)

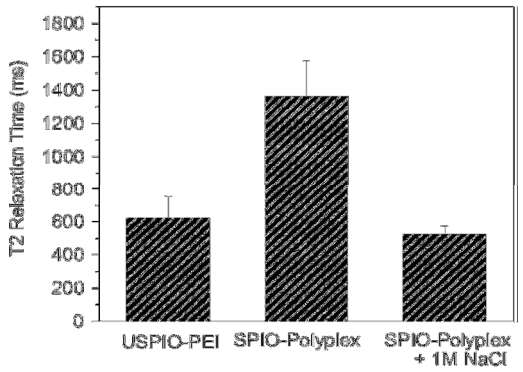

Figure 1-6: (a) The proposed mechanism of a 'T_2 relaxation switch'. (b) T_2 relaxation times upon formation of polyplexes and their subsequent dissociation upon addition of salt.

Figure adapted from Park, I.-K.; Ng, C.-P.; Wang, J.; Chu, B.; Yuan, C.; Zhang, S.; Pun, S. H. *Biomaterials* 2008, *29*, 724-732 with permission, Copyright Elsevier (2008).

Dubertret et al.[32] demonstrated that QDs encapsulated into phospholipid-block copolymer micelles (Figure 1.7) can be used as fluorescent probes for *in vitro* and *in vivo* imaging. ZnS-coated Cd-Se QDs encapsulated in the hydrophobic cavity of micelles formed with poly (ethylene glycol)-phosphatidylethanolamine (PEG-PE) and phosphatidylcholine (PC) were functionalized with primary amines to allow covalent binding to thiol-functionalized DNA. *In vivo* studies performed in *Xenopus* embryos revealed that these QD-micelles were able to label all types of embryonic cells without any aggregation, including somites, neurons, axonal tracks, ectoderm, neural crest, and endoderm. Additionally, QDs were found to be stable against photobleaching for as long as 80 min, a time at which rhodamine-green dextran dye was completely photobleached. Toxicity studies indicated no abnormalities in the embryo at typical concentration ($< 5x10^9$ QDs/cell)—they showed unaltered phenotype and normal health.

(i)

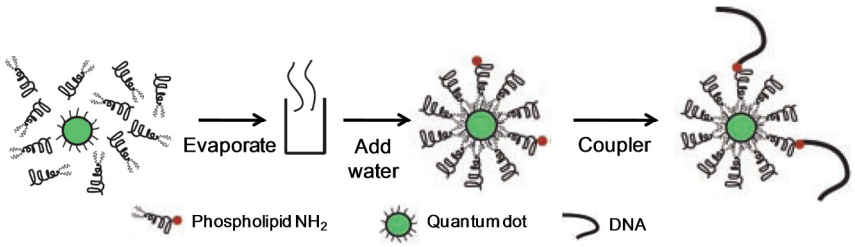

(ii)

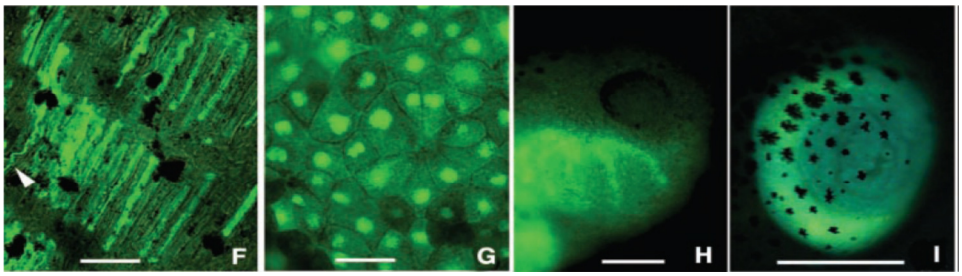

Figure 1-7: (i) Schematic of formation of a QD-micelle and its conjugation to single-stranded DNA (ssDNA). (ii) Fluorescence microscopy images of QD-micelles in different embryonic cells including: (F) axon (arrow) and somites at tadpole stage 40; (G) QDs localized in nucleus during mid-blastula stages; (H) neural crest cells; and (I) gut of an injected embryo. Scale bars: (F) and (G) 30 μm; (H) and (I) 0.5 mm.

Figure adapted from Dubertret, B.; Skourides, P.; Norris, D. J.; Noireaux, V.; Brivanlou, A. H.; Libchaber, A. In vivo imaging of quantum dots encapsulated in phospholipid micelles, *Science (Washington, D. C., 1883-)* 2002, *298*, 1759-1762 with permission from American Association for Advancement of Science.

Medarova et al.[33] synthesized dextran-coated superparamagnetic (MN) nanoparticles covalently attached to siRNA targeting green fluorescent protein (siGFP; five per particle), an NIR-emitting dye, Cy5.5 (NIRF; three per particle), and a membrane translocation peptide, myristolyated polyarginine peptide (MPAP; four per particle) to facilitate trafficking of

nanoparticles inside the cytoplasm of target cells (Figure 1.8a). Cellular uptake of MN-NIRF-siGFP in 9L-glioma cells (that stably expressed green fluorescent protein (GFP)) was monitored by fluorescence microscopy. These results were compared with red fluorescent protein (RFP)-expressing 9L-glioma cells to test the specificity of siRNA target towards GFP; target mRNA levels were compared via quantitative RT-PCR. *In vivo* studies in tumor-bearing mice bilaterally implanted with 9L-GFP- and 9L-RFP-expressing glioma cells showed significant mRNA knockdown in 9L-GFP tumors compared to saline only and mismatch controls (Figure 1.8b). After success of these proof-of-concept studies with GFP, MN-NIRF-MPAP-siSurvivin was developed to target survivin, a member of the inhibitor of apoptosis protein (IAP) family. MN-NIRF-MPAP-siSurvivin was injected into nude mice bearing subcutaneous human colorectal carcinoma tumors (LS174T) over a 2-week period and quantified by RT-PCR (Figure 1.8c)—strong reduction in survivin mRNA levels was observed. Additionally, *in vivo* studies with these particles indicated low cytotoxicity and a lack of immunostimulatory response (as monitored by aspartate aminotransferase (AST) and alanine aminotransferase (ALT) levels).

(a)

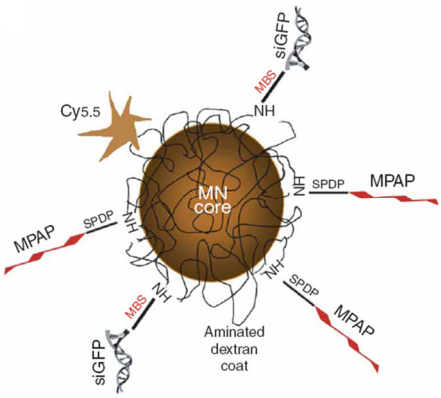

(b)

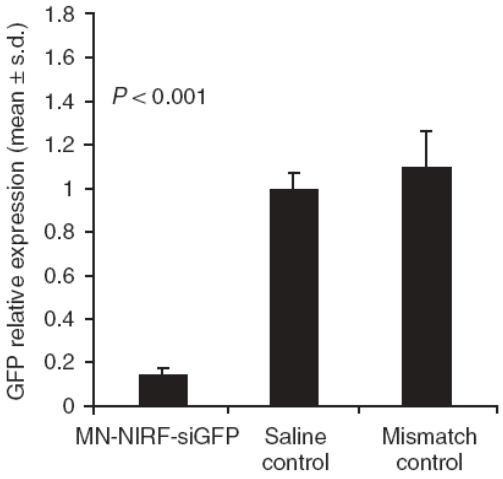

(c)

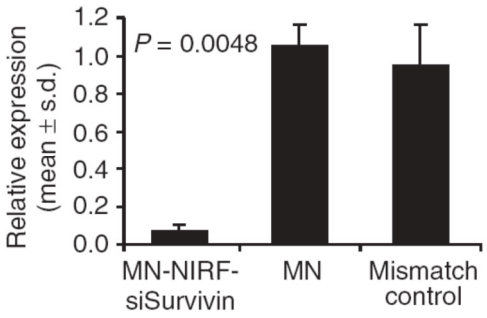

Figure 1-8: (a) Schematic of dextran-coated magnetic iron oxide nanoparticles containing siGFP, a NIR dye, Cy5, and a membrane translocation peptide, MPAP. Quantitative RT-PCR data of target mRNA levels in tumors of mice treated with MN-NIRF-siGFP (b) or MN-NIRF-siSurvivin (c) compared with controls.

Figure adapted from Medarova, Z.; Pham, W.; Farrar, C.; Petkova, V.; Moore, A., (2007*)* In vivo imaging of siRNA delivery and silencing in tumors. *Nat Med 13,* 372-377. with permission from Nature Publishing Group.

Davis and co-workers[34,35] have developed a series of linear cyclodextrin-containing polycations (CDPs) for *in vivo* delivery of nucleic acids. Their studies in mice have indicated,

upon systemic injection, significant uptake (of polyplexes containing cyclodextrin polycations and siRNA against EWS-FLI1 gene to treat Ewing sarcoma) in the tumor microenvironment can be achieved due to EPR effect; however, to maximize cellular internalization and specificity, the presence of a targeting ligand on the nanoparticles is crucial. Bartlett et al.[36] investigated the biodistribution and pharmacokinetics of polyplexes created by complexing CDP with siRNA via positron emission tomography (PET), computed tomography (CT) and bioluminescence imaging (BLI). The CDP delivery vehicles were conjugated to 1,4,7,10-tetraazacyclododecane-1,4,7,10-tetraacetic acid (DOTA), a chelator for [^{64}Cu], to introduce micro-PET/CT imaging functionality. *In vivo* biodistribution studies using micro-PET/CT in mice indicated that transferrin (Tf)-targeted and non-targeted nanoparticles have similar biodistribution and pharmacokinetic profiles (Figure 1.9). However, tissue analysis by bioluminescent imaging indicated that the targeted nanoparticles achieved greater target gene knockdown and thus had greater siRNA efficacy.

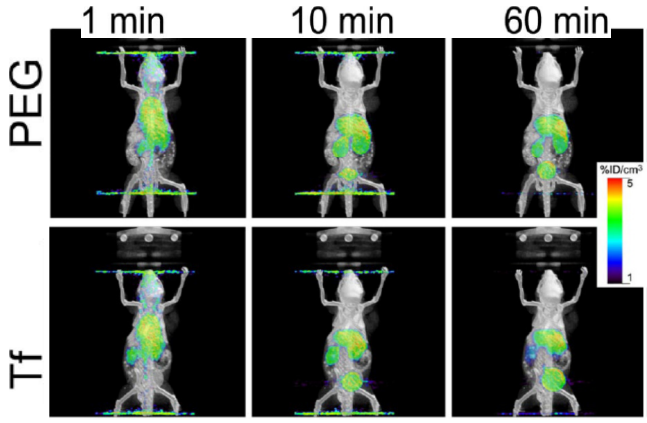

Figure 1-9: Fused micro-PET/CT images of transferrin-targeted ('Tf') and non-targeted ('PEG') nanoparticles injected into tumor-bearing mice and monitored at different time points (1 min, 10 min and 60 min) after injection.

Figure adapted from Bartlett, D. W.; Su, H.; Hildebrandt, I. J.; Weber, W. A.; Davis, M. E., (2007*)* Impact of tumor-specific targeting on the biodistribution and efficacy of siRNA nanoparticles measured by multimodality in vivo imaging. *Proc. Natl. Acad. Sci. U. S. A. 104,* 15549-15554. Copyright (2007) National Academy of Sciences, U.S.A

In a separate set of studies, Schneider et al.[37] studied intracellular trafficking of DNA/lipid complexes (lipoplexes) in rat smooth muscle cells (A10) via FRET. DNA and lipids were labeled with Cy3 and Cy5, respectively, and analyzed via flow cytometry, confocal microscopy and fluorimetric techniques to calculate the donor- (E_d) and acceptor-based (E_a) efficiencies of energy transfer (Figure 1.10). Different optical settings (donor excitation wavelengths) were used for flow cytometry (excitation = 488 nm) and microscopy (excitation = 523 nm) to study the kinetics of lipoplex dissociation. Analysis of the efficiency of donor- and acceptor-based energy transfer studied at different time points (3, 5, 9 and 24 h) indicated that most of the DNA was released from the lipoplexes by 24 h post-transfection. These findings and techniques are crucial to understand the intracellular trafficking and mechanism of vehicle unpackaging, and their studies have highlighted the value of FRET to facilitate information acquisition with high spatial resolution inside the cell.

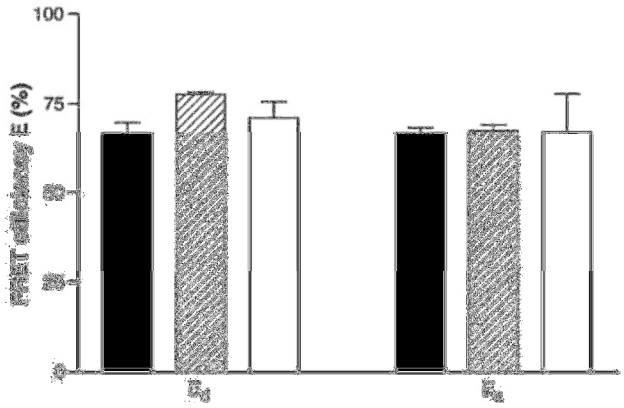

Figure 1-10: FRET efficiencies for donor (E_d) and acceptor (E_a) calculated based on three different measuring techniques: fluorimetry (solid bars), flow cytometry (hatched bars) and fluorescence microscopy (open bars) showed comparable results. The excitation wavelengths used for flow cytometry and fluorescence microscopy were 488 nm and 523 nm, respectively, and emission signals were monitored at 670 nm and above 650 nm, respectively.

Figure adapted from Schneider, S.; Lenz, D.; Holzer, M.; Palme, K.; Suess, R.Intracellular FRET analysis of lipid/DNA complexes using flow cytometry and fluorescence imaging techniques, *J. Controlled Release* 2010, *145*, 289-296 with permission, Copyright Elsevier (2010).

1.3. Theranostic Delivery Vehicles for Small Molecule Drugs

Several kinds of drug delivery vehicles have been developed over the years, such as polymeric micelles, block co-polymers, liposomes, inorganic iron oxide nanoparticles coated with a biocompatible polymer, and quantum dot conjugates. These vehicles have been used to deliver a variety of hydrophobic/hydrophilic anti-cancer drugs such as paclitaxel, doxorubicin, methotrexate, and camptothecin. In addition to inclusion of these drugs, the delivery vehicles can be decorated with various imaging agents to simultaneously monitor the therapeutic delivery.

With the increasing concerns of nephrogenic system fibrosis due to gadolinium-based blood pool agents in patients with renal disease or with recent liver transplant,[38] several approaches[39,40] have been recently taken to substitute gadolinium with manganese (Mn). For example, Pan et al.[39] developed a fibrin-targeting "nanobialys"-based contrast agent and drug delivery vehicle containing a porphyrin which chelates Mn. 'Nanobialys' are toroidal-shaped, nearly-monodisperse reverse micellar structures formed from amphiphilic branched polyethyleneimine (PEI) in anhydrous chloroform with a core containing a porphyrin-Mn(III) complex, which is a T_1 contrast agent for MRI (Figure 1.11a). Amphiphilic PEI was modified by reaction of amines with hydrophobic linoleic acid (55% of primary amines were reacted) via EDC coupling. The core of the micelles was loaded with a hydrophobic (camptothecin) or hydrophilic (doxorubicin) chemotherapeutic drug, and the drug release profile was studied *in vitro* for 3 days (Figure 1.11c). The MR imaging of fibrin (Figure 1.11b) was performed with fibrin-rich clots supported on silk sutures in phosphate-buffered saline (PBS) with the help of sealed polystyrene test tubes. The MR imaging results for targeted ligand-containing nanobialys (containing a fibrin-specific monoclonal antibody) were compared to nanobialys without any targeting ligand or without any metal inside as controls and demonstrated the role of the targeting agent in achieving contrast enhancement.

(a)

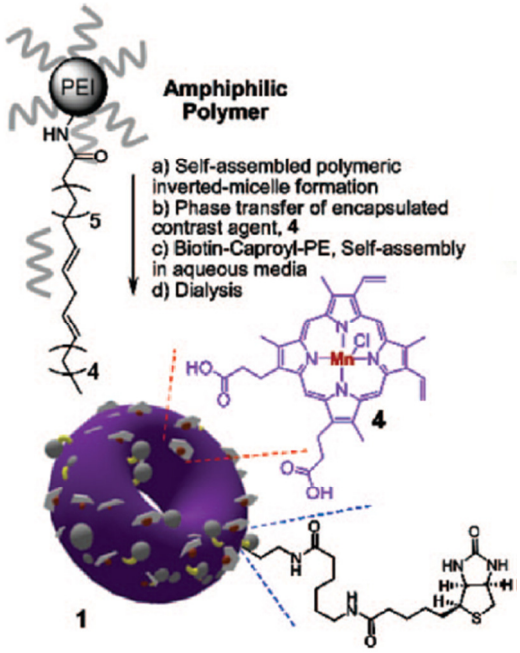

(b) (c)

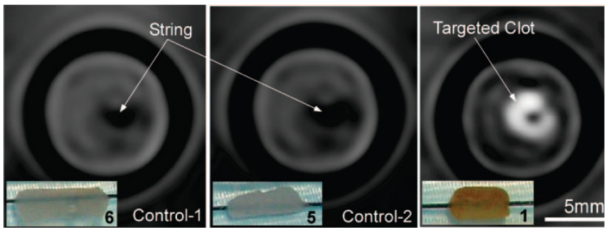

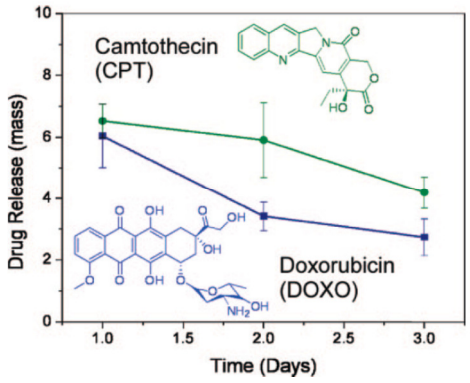

Figure 1-11: (a) Schematic of formation of nanobialys; (b) T_1-weighted MR images of Mn(III)-containing, fibrin-targeting nanobialys (right) compared with metal-free and non-targeted controls (left and center, respectively). (c) Drug (CPT or DOXO) release from the nanobialys was monitored for 3 days.

Figure adapted from Pan, D.; Caruthers, S. D.; Hu, G.; Senpan, A.; Scott, M. J.; Gaffney, P. J.; Wickline, S. A.; Lanza, G. M., (2008*)* Ligand-Directed Nanobialys as Theranostic Agent for

Drug Delivery and Manganese-Based Magnetic Resonance Imaging of Vascular Targets. *J. Am. Chem. Soc. 130,* 9186-9187. with permission from ACS.

Shin et al.[40] developed manganese oxide-based hollow nanoparticles (HMONs) as dual (T_1 and T_2) MRI contrast and drug delivery agents. HMONs were synthesized by stabilization of manganese oxide nanoparticles with oleate, encapsulation with poly (ethylene glycol)-phospholipid, and selective removal of the manganese oxide core in acidic phthalate buffer solution (pH = 4.6) to dope it with doxorubicin (DOX). Cell culture studies indicated that these HMONs were efficiently taken up by cultured cancer cells and induced cell death. High T_1 and T_2 image contrast was obtained upon MR imaging of transfected cells as well as the brain of a mouse injected with HMONs (Figure 1.12).

(a) (b)

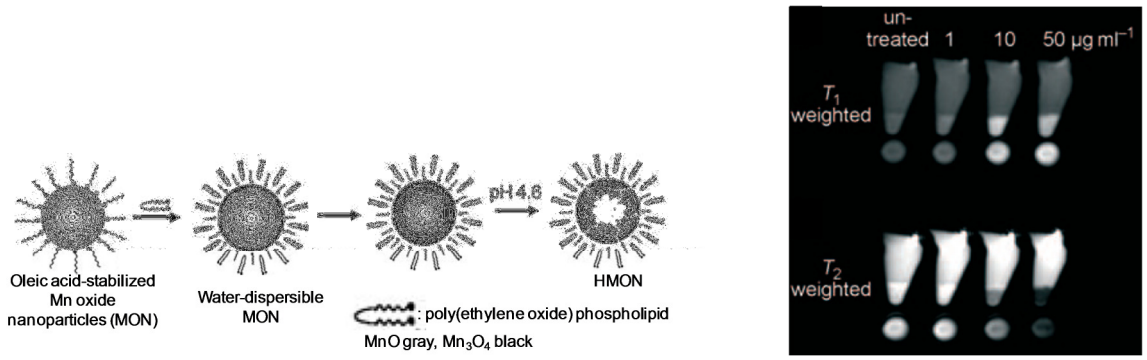

Figure 1-12: (a) Schematic of formation of HMON; (b) T_1- and T_2-weighted magnetic resonance images of DOX-loaded HMONs incubated with MCF-7 (human breast adenocarcinoma) cells at different concentrations and compared to untreated cells. A concentration-dependent increase in image contrast was observed.

Figure adapted from Shin, J.; Anisur, R. M.; Ko, M. K.; Im, G. H.; Lee, J. H.; Lee, I. S. Hollow manganese oxide nanoparticles as multifunctional agents for magnetic resonance imaging and

drug delivery, *Angew. Chem., Int. Ed.* 2009, *48*, 321-324. Copyright Wiley-VCH Verlag GmbH & Co. KGaA. Reproduced with permission.

1.3.1 Iron Oxide-Containing Theranostics for Delivery of Small Molecules

It has been shown that, at very low concentrations, circulating iron can impart T_1 contrast to MR imaging; however, at concentrations that are commonly used for T_2-weighted imaging, T_2 contrast is the predominant effect.[41] Encapsulation of iron oxide within a hydrophobic matrix can abate the T_2 effect and, thereby, improve T_1 contrast; hence, this can enable one to develop positive contrast agents that are devoid of the gadolinium cation. Senpan et al.[41] developed vascular-targeted colloidal iron oxide nanocolloids for the detection of atherosclerotic ruptured plaques and antiangiogenic plaque therapy. These nanoparticles can be loaded with an antiangiogenic mycotoxin drug, fumagillin (Figure 1.13a). Colloidal iron oxide nanocolloids with phospholipids containing a partially cross-linked hydrophobic core and a low concentration of pure magnetite iron oxide particles (0.5% w/v) show high T_1 relaxivity (7 [Fe] $mM^{-1}s^{-1}$) compared to those with a mixed core (Fe_2O_3-Fe_3O_4 mixture, 1.3 [Fe] $mM^{-1}s^{-1}$) and show potential as an alternative to gadolinium-containing agents (Figure 1.13b).

(a) (b)

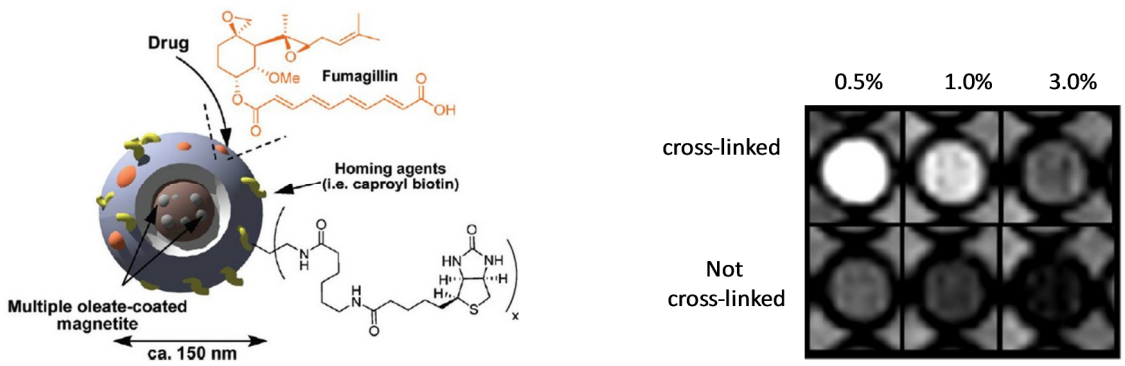

Figure 1-13: (a) Schematic of formation of fumagillin-loaded CION with a targeting ligand on the surface. (b) T_1-weighted MR imaging for colloidal iron oxide nanocolloids with (top row) and without (bottom row) surfactant cross-linking and with different extents of magnetite loading (0.5%, 1.0%, or 3.0% w/v). CIONs with the lowest magnetite loading evaluated showed the greatest image contrast.

Figure reprinted from Senpan, A.; Caruthers, S. D.; Rhee, I.; Mauro, N. A.; Pan, D.; Hu, G.; Scott, M. J.; Fuhrhop, R. W.; Gaffney, P. J.; Wickline, S. A.; Lanza, G. M., (2009*)* Conquering the Dark Side: Colloidal Iron Oxide Nanoparticles. *ACS Nano 3,* 3917-3926. with permission from ACS.

Calcium phosphate-based delivery vehicles can be effective for the delivery of hydrophobic, insoluble drugs such as ceramide and camptothecin. Calcium phosphate nanoparticles are relatively insoluble at physiological pH (pH=7.4) but have improved solubility in acidic pH environments (pH=6.5). Upon endocytosis, calcium phosphate will release the drug only in acidic compartments of the cell (endosomes and lysosomes), thus reducing the off-target toxicity in systemic administration. Researchers[42,43] have used this pH-tunable solubility to develop calcium phosphate-based vehicles for controlled, pH-triggered drug delivery. Kester et al. have developed colloidally-stable, amine carboxylate- and polyethylene glycol-functionalized

calcium phosphate nanoparticles (CPNPs) for delivery of ceramide (Cer6 and Cer10) and a fluorescent dye, rhodamine-water tracer (Rh-WT), to melanoma and breast adenocarcinoma cells.[43] Upon encapsulation into CPNPs, the lifetime and quantum properties of fluorescent dyes are believed to be improved.[44,45] Nanoparticles lacking any drug within were non-toxic (Figure 1.14) at low concentrations, and drug encapsulation induced apoptosis in neural, melanoma and breast adenocarcinoma cells measured by MTS assay.

Barth et al. further modified CPNP with PEG groups and one of two different antibodies targeting the gastrin (gastrin-10-PEG-CPNP) and transferrin receptor (antiCD71-Avidin-CPNP), respectively.[42] These materials were created to study the *in vivo* biodistribution of CPNPs in murine models containing pancreatic (orthotopic) and breast (subcutaneous) cancer tumors. *In vivo* imaging using NIR microscopy (indocyanine green, ICG) on athymic female mice bearing tumor xenografts indicated greater tumor accumulation of targeted nanoparticles than non-targeted ones and penetration through the blood-brain barrier (Figure 1.15).

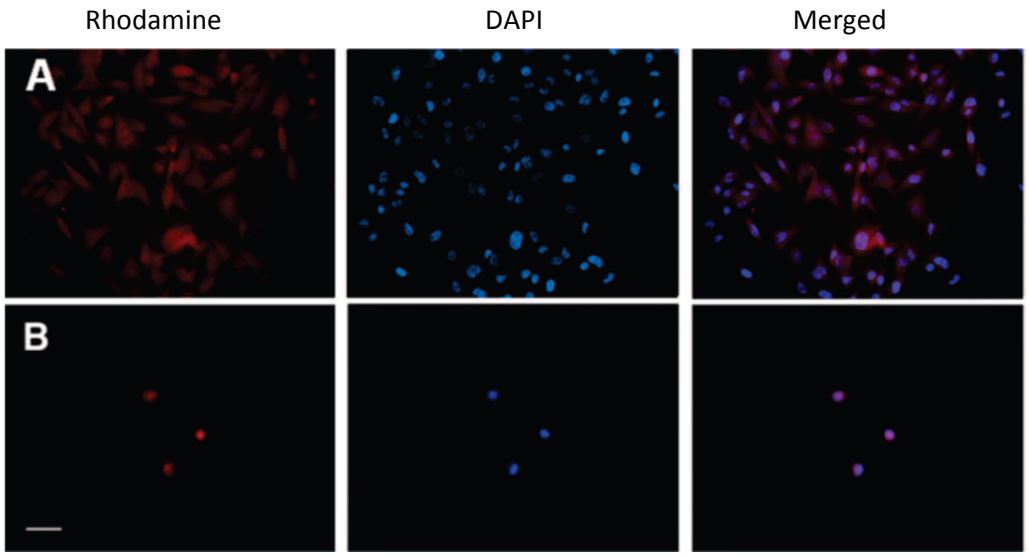

Figure 1-14: Cell images of cultured melanoma cells (UACC 903) exposed to Rh-WT-CPNPs with (B) or without (A) anticancer drug (Cer10). Cell nuclei stained with DAPI (blue). Cer10-containig CPNPs, unlike control CPNPs, induced melanoma cell death.

Figure adapted from Kester et al., *Nano Lett.* 2008, *8*, 4116-4121 with permission from ACS.

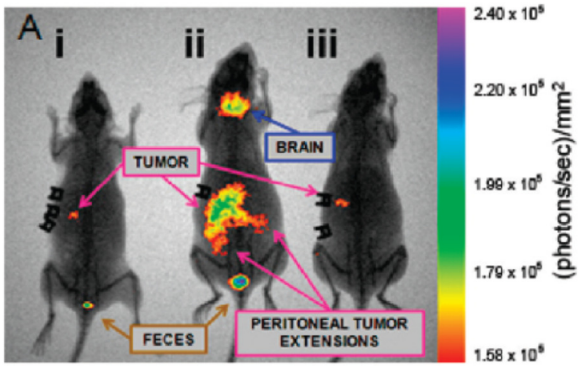

Figure 1-15: Human BxPC-3 pancreatic cancer cells were xenografted orthotopically in athymic nude mice. Biodistribution of indocyanine green (ICG) loaded PEG-CPNPs decorated with one of two different gastrin targeting groups (gastrin-10 (ii) and pentagastrin (iii)) was assessed *in vivo* using NIR imaging and compared to untargeted ICG loaded-PEG-CPNPs. Both non-

targeted (i) and pentagastrin-targeted CPNPs showed some tumor accumulation; however, significantly higher accumulation was observed with gastrin-10-targeted PEG-CPNPs.

Figure adapted from Barth, B. M.; Sharma, R.; Altinoglu, E. I.; Morgan, T. T.; Shanmugavelandy, S. S.; Kaiser, J. M.; McGovern, C.; Matters, G. L.; Smith, J. P.; Kester, M.; Adair, J. H., (2010*)* Bioconjugation of Calcium Phosphosilicate Composite Nanoparticles for Selective Targeting of Human Breast and Pancreatic Cancers In Vivo. *ACS Nano 4,* 1279-1287. with permission from ACS.

Langer and co workers[46,47] developed poly(ethylene oxide) (PEO)-modified poly(β-amino ester) (PbAE)-based materials as novel, pH-responsive, non-toxic and biodegradable nanoparticle drug carriers. Solid unprotonated PbAEs (Figure 1.16a) are insoluble at physiological pH; however, the solubility increases upon protonation of the amines along the backbone. Below pH 6.5, PbAEs release their payload of chemotherapeutic drug, such as paclitaxel. *In vivo* biodistribution of encapsulated polymeric nanoparticles was studied in nude mice via radiolabeling using ^{111}Indium oxine (Figure 1.16b). When tumor-bearing (human ovarian adenocarcinoma) mice were evaluated 5 h after intravenous administration, 23-fold and 8.7-fold increases in tumor accumulation (compared to an aqueous solution of paclitaxel) were observed for paclitaxel-loaded PEO-PbAE nanoparticles and PEO-poly(caprolactam) (PCL) nanoparticles, respectively.

(a)

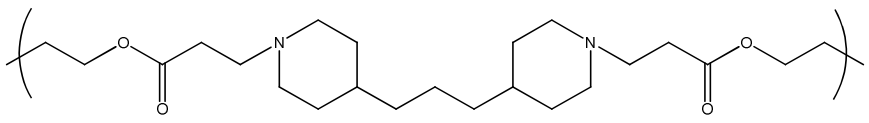

(b)

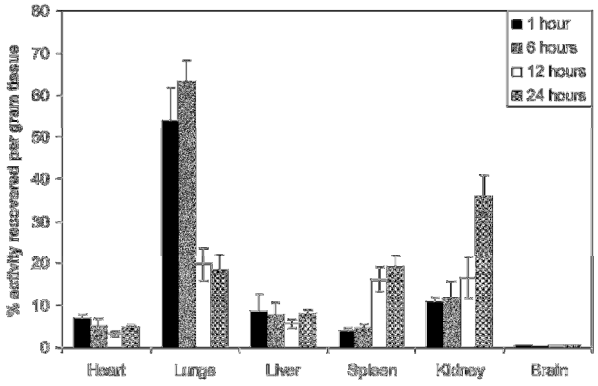

Figure 1-16: (a) Chemical structure of poly(β-amino ester) (PbAE). (b) Biodistribution of PEO-modified PbAE based nanoparticles loaded with gamma-emitter indium [^{111}In] oxine was examined in non-tumor-bearing mice at indicated time points (1, 6, 12, and 24 h post-administration) by comparing the percentage of recovered radioactivity within indicated organs. Figures reprinted from Shenoy, D.; Little, S.; Langer, R.; Amiji, M., (2005*)* Poly(ethylene oxide)-Modified Poly(beta -amino ester) Nanoparticles as a pH-Sensitive System for Tumor-Targeted Delivery of Hydrophobic Drugs. 1. In Vitro Evaluations. *Molecular Pharmaceutics 2,* 357-366. and Shenoy, D.; Little, S.; Langer, R.; Amiji, M., (2005*)* Poly(Ethylene Oxide)-Modified Poly(beta -Amino Ester) Nanoparticles as a pH-Sensitive System for Tumor-Targeted Delivery of Hydrophobic Drugs: Part 2. In Vivo Distribution and Tumor Localization Studies. *Pharmaceutical Research 22,* 2107-2114. with permission from ACS and Springer.

In another approach to theranostics, magnetoplasmonic nanoparticle assemblies (MPAs) combine both the magnetic and optical properties of metal nanoparticles and can be imaged with both magnetic resonance imaging and photoacoustic imaging. The general method for synthesizing these nanoparticles is by gradual reduction of gold nanoparticles in the presence of magnetic metal particles. The field of MPAs has been primarily restricted to hyperthermia or

photothermal ablation treatment in cancer therapy thus far, and there have been few examples of incorporation of anticancer drugs within these nanoparticles. Chen et al.[48] synthesized magnetoplasmonic particles with a magnetic iron oxide (Fe_3O_4) core by co-precipitation—the core was coated with a porous, water-dispersible silica layer and then functionalized with gold nanoparticles, forming corona-like structures via surface amine functionality. This corona-like morphology was studied in MPAs containing curcumin, an anticancer drug (Figure 1.17a), using transmission electron microscopy (TEM) (Figure 1.17c); the particle size was determined to be ~400 nm and ~600 nm for MPA-curcumin and MPA-PEG-curcumin, respectively. The T_2 relaxation time of human leukemia cells (HL-60) transfected with MPA particles loaded with curcumin was lower than that of untransfected cells, as expected. Further, results of an MTT assay to examine therapeutic efficiency revealed that, while MPA-PEG-curcumin outperforms MPA-curcumin, both are potent inducers of apoptosis in HL-60 cells (Figure 1.17b).

(a)

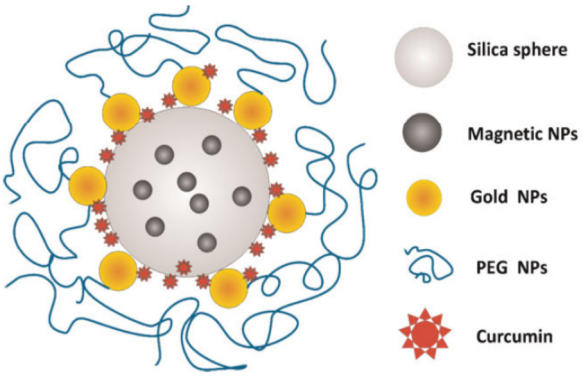

(b) (c)

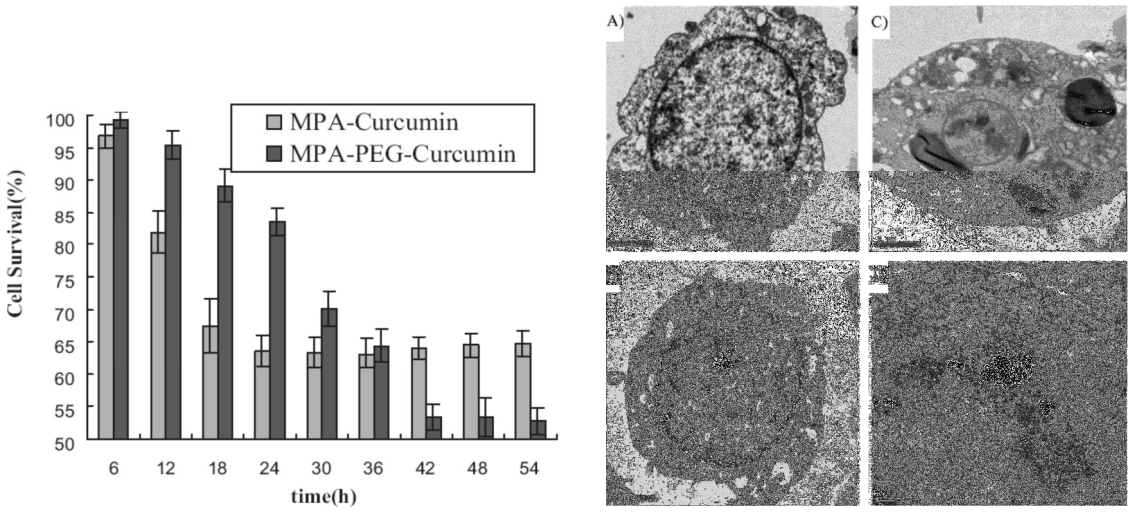

Figure 1-17: (a) Schematic of magnetoplasmonic nanoparticles containing magnetic iron oxide for anticancer drug delivery. (b) An MTT assay performed on human leukemia (HL-60) cells at various time points after treatment with curcumin-loaded MPA and MPA-PEG revealed significant, time-dependent induction of apoptosis for both preparations. (c) Transmission electron micrographs (TEMs) of HL-60 cells that were untreated (A), transfected with pure curcumin (B), or transfected with curcumin-loaded MPA-PEG (C). (D) This image is a magnified image of the circled portion of image (C). A change in cell morphology was observed upon treatment with curcumin-loaded MPA-PEG particles.

Figure adapted from Chen, W.; Xu, N.; Xu, L.; Wang, L.; Li, Z.; Ma, W.; Zhu, Y.; Xu, C.; Kotov, N. A. Multifunctional Magnetoplasmonic Nanoparticle Assemblies for Cancer Therapy and Diagnostics (Theranostics), Macromol. Rapid Commun. 31, 228-236. Copyright Wiley-VCH Verlag GmbH & Co. KGaA. Reproduced with permission.

Several research groups have introduced multimodal imaging functionalities into drug delivery vehicles. For example, Xie et al.[49] adapted a novel approach of treating iron oxide nanoparticles (IONPs) with dopamine to make them moderately hydrophilic, thereby allowing

them to be doped into human serum albumin (HSA) matrices in a way very similar to that used for drug loading. Using this technique, IONPs were surface functionalized with Cy5.5 (fluorescence imaging) and [^{64}Cu] (PET imaging) via NHS ester-NH_2 coupling (Figure 1.18a). For *in vivo* and *ex vivo* imaging, animal models were prepared by subcutaneously injecting glioblastoma cells (U87MG) into the front flank of each mouse. Images were obtained at 1 h, 4 h and 18 h post-injection for PET and NIRF imaging (Figure 1.18b) and at 18 h post-injection for MR imaging. MR imaging studies with HSA-IONPs indicated higher relaxivity (r_2) values and longer blood circulation half-life than a frequently-used contrast agent, Feridex®.

(a) (b)

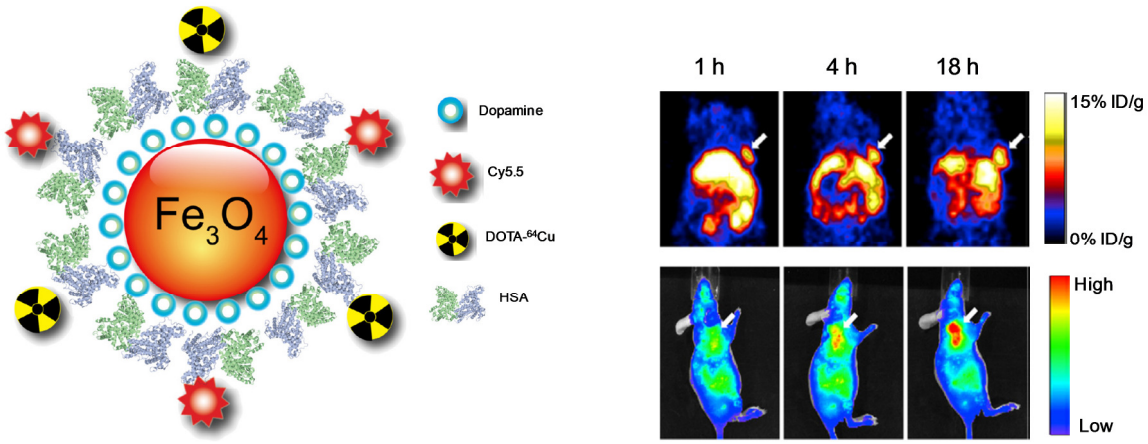

Figure 1-18: (a) Schematic of HSA-IONPs. (b) NIRF (bottom) and PET (top) images of a mouse containing a subcutaneous glioblastoma tumor taken 1 h, 4 h and 18 h post-injection of HSA-IONPs. Significant tumor accumulation was observed via both imaging techniques, as indicated by an arrow.

Figure adapted from Xie, J.; Chen, K.; Huang, J.; Lee, S.; Wang, J.; Gao, J.; Li, X.; Chen, X. PET/NIRF/MRI triple functional iron oxide nanoparticles, *Biomaterials* 2010, *31*, 3016-3022 with permission, Copyright Elsevier (2010).

Liong et al.[50] synthesized mesoporous silica nanoparticles doped with superparamagnetic iron oxide nanocrystals and hydrophobic anticancer drugs, such as camptothecin (CPT) or paclitaxel (TXL), and functionalized with hydrophilic groups, like phosphonates, onto the surface to achieve high stability in aqueous solutions (Figure 1.19a). Incorporation of silica into theranostic nanoparticles like these can impart numerous desirable properties—silica nanoparticles are known to be endocytosed by cells, provide a mesoporous matrix capable of being doped with other inorganic metal particles (such as gold and iron oxide), and can be easily functionalized owing to silane linkers present on their surface. Additionally, a fluorescent dye, fluorescein isothiocyanate (FITC), and α-folate receptor-targeting folic acid groups were conjugated on the surface to promote uptake by tumor cells. Cellular uptake studies carried out in two types of pancreatic cancer cells, PANC-1 and BxPC3, indicated nanoparticles were internalized within 30 min of transfection. By comparison with drug-free nanoparticle controls, which were non-toxic, the toxicity of these nanoparticles was attributed to its drug payload (Figure 1.19b).

(a) (b)

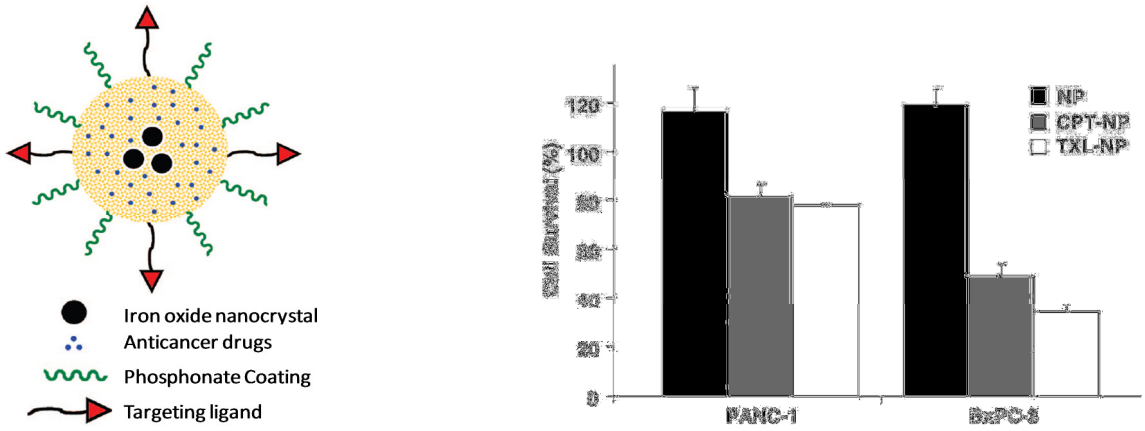

Figure 1-19: (a) Schematic of multifunctional iron oxide nanoparticles. (b) Cell growth inhibition assay results indicating relative therapeutic efficiency of CPT- or TXL-loaded nanoparticles in two different pancreatic cancer cell lines (PANC-1 and BxPC-3). Drug-free control nanoparticles were found to be non-toxic.

Figure reprinted Liong, M.; Lu, J.; Kovochich, M.; Xia, T.; Ruehm, S. G.; Nel, A. E.; Tamanoi, F.; Zink, J. I., (2008*)* Multifunctional Inorganic Nanoparticles for Imaging, Targeting, and Drug Delivery. *ACS Nano 2,* 889-896.with permission from ACS.

In order to achieve a high therapeutic concentration at the site of interest and to reduce off-target effects, several researchers have developed targeted theranostic agents to address specific receptors or proteins that are over expressed in cancer targets, as has been mentioned above. In another example of this, Gao and coworkers[51,52] have developed targeted polymeric micellar architectures for drug delivery and magnetic resonance imaging. The core-shell morphology helps to introduce different hydrophobic functionalities (therapeutic and imaging) into the core, and the hydrophilic shell improves the stability in aqueous system and prevents aggregation. Polymeric micellar structures based on amphiphilic block copolymers—maleimide-terminated poly(ethylene glycol)-block-poly(D,L-lactide) copolymer (MAL-PEG-PLA) and

methoxy-terminated poly(ethylene glycol)-block-poly(D,L-lactide) copolymer (MPEG-PLA)—were developed and loaded with doxorubicin (DOX) and superparamagnetic iron oxide (SPIO). Functionalization of these polymeric micelles was performed with $\alpha_v\beta_3$ integrin receptor-targeting cRGD peptide via thiol-maleimide reaction, and different extents of cRGD loading (0% vs. 16%) were achieved through control of the amount of MPEG-PLA introduced into the system. Incorporation of the targeting group on polymeric micelles showed a concomitant change in cell uptake, MR image contrast (Figure 1.20a) and DOX-induced cytotoxicity (Figure 1.20b). Cellular uptake studies performed using flow cytometry and confocal laser scanning microscopy indicated that uptake of targeted particles was about 2.5 times higher than that of non-targeted analogues.

(a) (b)

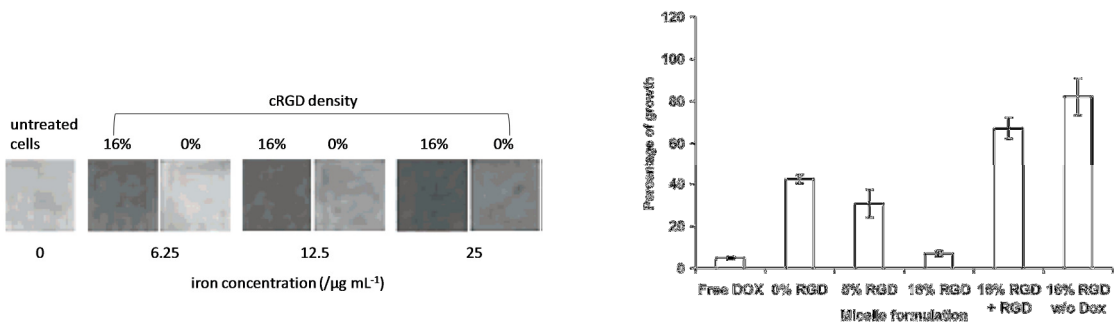

Figure 1-20: (a) Significant T_2-weighted image contrast was achieved for SLK endothelial tumor cells transfected with cRGD-containing micelles (16% cRGD density) compared to non-targeted (0% cRGD density) micellar analogues. (b) An increase in DOX induced-cytotoxicity in SLK cells was achieved upon incorporation of cRGD within the micellar nanoparticles.

Figure adapted from Nasongkla, N.; Bey, E.; Ren, J.; Ai, H.; Khemtong, C.; Guthi Jagadeesh, S.; Chin, S.-F.; Sherry, A. D.; Boothman David, A.; Gao, J., (2006*)* Multifunctional polymeric micelles as cancer-targeted, MRI-ultrasensitive drug delivery systems. *Nano Lett. 6,* 2427-2430. with permission from ACS.

In a separate study, these polymeric micelles were modified with a lung cancer-targeting peptide (LCP) that binds specifically to $\alpha_v\beta_6$ receptors overexpressed on lung cancer cells. The specificity of LCP for $\alpha_v\beta_6$-expressing H2009 cells (lung cancer cells) was evaluated by comparative exposure to $\alpha_v\beta_6$-negative H460 cells and by using micelles containing a scrambled peptide (SP, a peptide with same amino acid composition as LCP but scrambled sequence) in H2009 cells using [^{3}H] radioactivity measurement, confocal microscopy (Figure 1.21), and MRI.

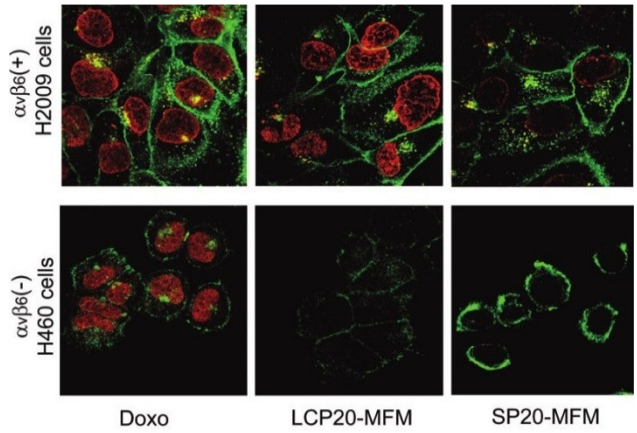

Figure 1-21: Evaluation of the cellular uptake of LCP-functionalized, doxorubicin (Doxo)-loaded multifunctional micelles (LCP20-MFM) in $\alpha_v\beta_6$-positive H2009 cells (top panels) and $\alpha_v\beta_6$-negative H460 cells (bottom panels) by fluorescence microscopy. Free Doxo (left panels) and MFM functionalized with a scrambled peptide (SP20-MFM, right panels) were used for comparison with LCP20-MFM (center panels). The cell membrane was stained with Alexa Fluor® 350 and pseudocolored with green; Doxo fluorescence is indicated in red.

Figure adapted from Guthi, J. S.; Yang, S.-G.; Huang, G.; Li, S.; Khemtong, C.; Kessinger, C. W.; Peyton, M.; Minna, J. D.; Brown, K. C.; Gao, J., (2010*)* MRI-Visible Micellar Nanomedicine for Targeted Drug Delivery to Lung Cancer Cells. *Mol. Pharmaceutics 7,* 32-40. with permission from ACS.

The folate receptor is another surface molecule overexpressed on many cancer cells (such as lung, breast, and cervical cancer cells); consequently, numerous groups have imparted folate-receptor targeting in their theranostic nanoparticles. Santra et al.[53] developed a novel synthetic method to prepare biodegradable and biocompatible poly(acrylic acid)-iron oxide nanoparticles (PAA-IONPs). PAA-IONPs were functionalized with NIR dyes, DiR and DiL, and an anticancer drug, Taxol®, by a solvent-diffusion method, then "click" chemistry was used to introduce a folate-receptor targeting ligand. Cytotoxicity and target specificity of folate-functionalized IONP were examined in lung carcinoma cells (A549, overexpress folate receptor) and cardiomyocytes (H9c2, do not overexpress folate receptor) via a MTT assay. The results from the MTT assay indicated almost 100% survival, for both A549 and H9c2 cells, when exposed to control Taxol®-free PAA-IONPs. However, upon Taxol® encapsulation in these PPA-IONPs, cell survival for A549 reduced to 20% after 3 h incubation, whereas cell viability for H9c2 cells remained unchanged. These results indicate specificity of PAA-IONPs towards tumor cells that overexpress folate receptor. Drug/dye release was only observed in acidic pH or in presence of esterase, a degradative enzyme.

In another example of targeting of the folate receptor, Kohler et al.[54] covalently functionalized superparamagnetic iron oxide (SPIO) nanoparticles with an anticancer drug, methotrexate (MTX). MTX was incorporated via a peptide linkage that is reducible under acidic pH, thereby releasing the drug into the cell upon reaching the acidic environment of the endosome/lysosome. MTX is a reduced form of folic acid that inhibits dihydrofolate reductase, thereby stopping the folic acid cycle and inducing cellular toxicity. The delivery efficacy and cytotoxicity of MTX-loaded SPIO nanoparticles vs. free MTX was tested in human cervical cancer cells (HeLa) and breast cancer cells (MCF-7). The endocytosis of these particles was

confirmed to be folate-receptor-mediated, as determined by use of an acidic condition (to mimic lysosomes) and TEM.

Das et al.[55] synthesized N-phosphonomethyl iminodiacetic acid (PMIDA)-functionalized ultrasmall iron oxide nanoparticles (USPIO) equipped with (i) rhodamine B isothiocyanate (RITC) for optical imaging, (ii) a chemotherapeutic drug, methotrexate (MTX), and (iii) folic acid (FA) for targeting the folic acid receptor. They initially synthesized amine-functionalized iron oxide nanoparticles via a two-step process. First the USPIOs were synthesized by an alkali-mediated chemical co-precipitation process in the presence of PMIDA containing one phosphonic and two carboxylic groups. This process creates stable nanoparticles with high interparticle repulsion due to negatively-charged carboxylic and phosphonate groups on the surface. An amine-functionalized surface was then generated by reacting the terminal carboxylic acids with diamine (EDBE) in the presence of EDC and NHS. This amine functionality was further utilized to introduce MTX, RITC and FA onto the particle to make USPIO-PMIDA-EDBE-RITC-FA. These authors were the first to functionalize an iron oxide surface with phosphonate groups (as opposed to solely using carboxylate groups, which is more common). The benefit of using phosphonate groups—instead of or in addition to carboxylate group—is that the phosphonate bond increases thermal stability and reduces susceptibility to enzymatic degradation. These targeted USPIO-PMIDA-EDBE-RITC-FA particles showed significantly higher cell uptake and MTX-induced cytotoxicity for folate receptor-expressing cancer (HeLa) cells than in non-folate receptor-expressing (MG-63) cells.

In a final example of iron oxide-containing theranostic nanoparticles, Kim et al.[56] have developed a facile synthetic route (Figure 1.22a) with good control over size to synthesize monodisperse, discrete mesoporous silica materials (smaller than 100 nm) containing a single

Fe_3O_4 nanocrystal as a core (Fe_3O_4@$mSiO_2$,). Fluorescent dyes, rhodamine (R) or fluorescein (F) isothiocyanate, were covalently attached to the silica surface and doxorubicin (DOX) was encapsulated within the silica matrix. Next, the surface of the rhodamine-containing nanoparticles was functionalized with PEG groups (Fe_3O_4@$mSiO_2$(R)-PEG) to minimize non-specific interactions and lengthen the blood circulation half-life. DOX-induced cytotoxicity was studied by transfecting SK-BR-3 cells with DOX-loaded Fe_3O_4@$mSiO_2$(R)-PEG nanoparticles. *In vivo* studies were performed by subcutaneously injecting MCF-7 cells pre-treated with Fe_3O_4@$mSiO_2$(R)-PEG particles into the dorsal shoulder of nude mice. The MCF-7 cells containing Fe_3O_4@$mSiO_2$(R)-PEG particles were easily detectable as dark spots on T_2-weighted MR images and elicited significant rhodamine fluorescence when examined by fluorescence imaging (Figure 1.22b).

(a)

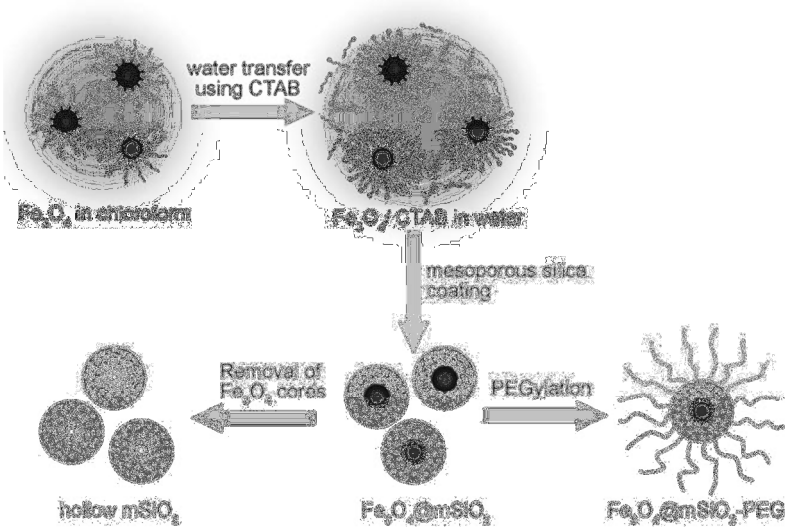

(b)

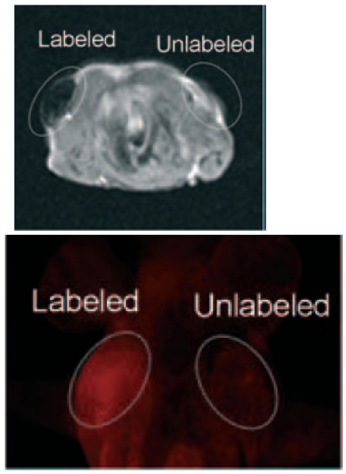

Figure 1-22: (a) Schematic for synthesis of Fe_3O_4@mSiO_2–PEG. (b) *In vivo* T_2-weighted MR imaging (top) and fluorescence microscopy imaging (bottom) of MCF-7 cells transfected with Fe_3O_4@mSiO_2–PEG, either unlabeled or labeled with rhodamine.

Figure adapted from Kim, J.; Kim, H. S.; Lee, N.; Kim, T.; Kim, H.; Yu, T.; Song, I. C.; Moon, W. K.; Hyeon, T. Multifunctional uniform nanoparticles composed of a magnetite nanocrystal core and a mesoporous silica shell for magnetic resonance and fluorescence imaging and for drug delivery, *Angew. Chem., Int. Ed.* 2008, *47*, 8438-8441. Copyright Wiley-VCH Verlag GmbH & Co. KGaA. Reproduced with permission.

1.3.2 Quantum Dot-Containing Theranostics for Delivery of Small Molecules

Quantum dots (QDs) are semiconductor materials with cadmium-selenium (Cd-Se) or cadmium-tellurium (Cd-Te) cores. As mentioned earlier, some of the major advantages of using QDs over fluorescent dyes are high extinction coefficients, control over optical properties, and reduced susceptibility to photobleaching. In addition, many QDs are known to form FRET pairs with fluorescent dyes, which allows them to be effectively used to understand intracellular trafficking and unpackaging of particles that contain them.[13,57-59]

Bagalkot et al.[60] have developed multifunctional nanoparticles for drug delivery based upon QDs that are capable of detecting and treating cancer. They have created a novel, QD-targeting aptamer-doxorubicin conjugate (QD-Apt(Dox)) (Figure 1.23) that effectively targets prostate cancer cells via incorporation of an RNA aptamer (A10) which binds prostate-specific membrane antigen (PSMA). QD-Apt (Dox) systems were synthesized by first conjugating amine-terminated A10 aptamer with carboxylic group-functionalized QDs via EDC coupling and NHS activation chemistry. Once the aptamer is immobilized on the QD surface, Dox was introduced and conjugated by CG-sequence intercalation within the PSMA-targeting aptamer. The release of Dox from the delivery vehicle was detected from the conjugate via bimolecular FRET (Bi-FRET, Figure 1.23a and 1.23b). When the QD-Apt (Dox) conjugate is intact, both the QD and Dox fluorescence are in the 'OFF' state—QD fluorescence is quenched by Dox, and Dox fluorescence is simultaneously quenched due to intercalation within the A10 aptamer. However, upon the dissociation of the conjugate/complex to release drug, the fluorescence is turned 'ON'; hence, this system can be used to monitor intracellular vehicle unpackaging to release its cargo. The specificity of the A10 aptamer for PSMA was tested via MTT assay and confocal microscopy by transfecting QD-aptamer (Dox) conjugates into LNCaP (PSMA+) and PC3 (PSMA-) prostate adenocarcinoma cells. Minimal cytotoxicity resulting from QD-Apt(D)X) was observed for PC3 cells compared to LNCaP cells, whereas comparable toxicity was achieved in these two cells for free Dox. These results together indicate successful targeting of these QD-containing theranostics to PSMA via inclusion of the A10 aptamer.

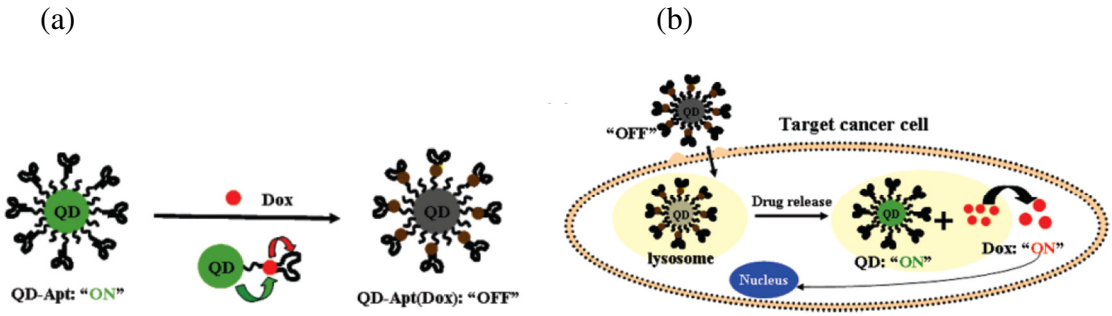

Figure 1-23: (a) Schematic of QD-Apt(Dox) conjugate in fluorescence 'ON' state before conjugation to Dox, which leads to conversation to the 'OFF' state due to Bi-FRET between two donor-acceptor (quencher) pairs. (b) Schematic of the proposed mechanism to monitor intracellular trafficking using Bi-FRET in QD-Apt (DOX) conjugates.

Figure adapted from Bagalkot, V.; Zhang, L.; Levy-Nissenbaum, E.; Jon, S.; Kantoff, P. W.; Langer, R.; Farokhzad, O. C., (2007*)* Quantum Dot-Aptamer Conjugates for Synchronous Cancer Imaging, Therapy, and Sensing of Drug Delivery Based on Bi-Fluorescence Resonance Energy Transfer. *Nano Lett. 7,* 3065-3070.with permission from ACS.

1.4. Theranostics in Photodynamic Therapy

In photodynamic therapy (PDT), a photosensitizer-containing drug is delivered to the tumor cell that, upon light activation, generates 'killer' singlet oxygen and free radicals (reactive oxygen species (ROS)) that induce apoptosis. PDT is currently being explored as a novel cancer treatment strategy. Three important things for the success of PDT are: (i) minimized systemic toxicity, (ii) adequate oxygen permeability and drug (or O_2) diffusion in the diseased region, and (iii) sufficient concentration of photosensitizer in the region of interest (must have a high singlet oxygen quantum yield). These requirements are necessary to minimize the thermal damage due to photoirradiation and to avoid unwanted toxicity to neighboring healthy cells.

Porphyrin derivatives are the most commonly-used photosensitizers in PDT. When irradiated with the required wavelength, the porphyrin produces cytotoxic singlet oxygen species via reaction of excited-state porphyrin with nearby molecular oxygen. In PDT, off-target toxicity can be prevented because generating of the cytotoxic species only occurs at the site of illumination, which allows the therapy to be localized. This localized accumulation of the drug can further be enhanced by conjugation with targeting moieties and/or encapsulation in nanoparticles to increase concentration at the target site. Attachment of targeting groups can help to reduce one of the major limitations associated with PDT–-increased patient photosensitivity due to prolonged accumulation of the drug within the skin.

McCarthy et al.[61] developed macrophage-targeted theranostic nanoparticles (TNPs) for PDT application to cardiovascular diseases such as atherosclerosis and in-stent restenosis. Dextran-coated superparamagnetic iron oxide nanoparticles targeting the dextran receptor, SIGNR1, on macrophages were synthesized[62-66] and functionalized with a photosensitizer, 5-(4-carboxyphenyl)-10,15,20-triphenyl-2,3-dihydroxychlorin (TPC), and a fluorescent dye, Alexa Fluor® 750, through covalent bonding with amine groups present on the surface of iron oxide particles. Cell uptake and light-induced phototoxicity studies carried out in a murine macrophage (RAW 264.7) cell line transfected with TNPs (0.1 mg Fe per mL) indicated only 35% cell survival after 1 h irradiation with a 646-nm laser. No toxicity was observed for TNPs without any photosensitizer loaded. TNPs (0.2 mg Fe per mL) caused as high as 100% cell death (Figure 1.24) after irradiation with a 646-nm laser for 1 h in human macrophage (U937) cells.

(a) (b)

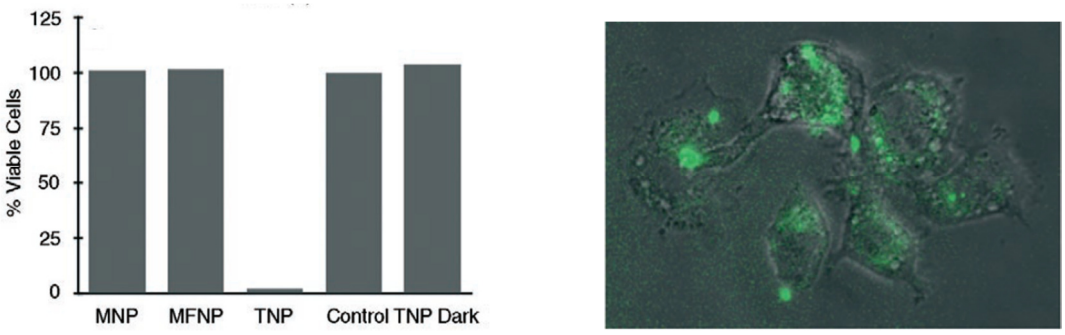

Figure 1-24: (a) Results from MTS assay of the viability of human macrophage (U937) cells upon transfection with indicated species and irradiation with a 646-nm laser for 1 h. "MNP" = magnetic nanoparticles (lack TPC and Alexa Fluor® 750). "MFNP" = magnetofluorescent nanoparticles (lack TPC, contain Alexa Fluor® 750). "TNP" = theranostic nanoparticles (contain TPC and Alex Fluor® 750). "Control" = untransfected. "TNP Dark" = exposed to TNP but not irradiated. Unlike all other treatments, TNPs induced near complete cytotoxicity upon irradiation. (b) Fluorescence microscopy images of murine macrophage (RAW 264.7) cells incubated with TNPs (green) for 3 h reveal intracellular accumulation of TNPs.

Figure adapted from McCarthy, J. R.; Jaffer, F. A.; Weissleder, R. A macrophage-targeted theranostic nanoparticle for biomedical applications, *Small* 2006, *2*, 983-987. Copyright Wiley-VCH Verlag GmbH & Co. KGaA. Reproduced with permission.

Kopelman et al.[67] have developed an extracellular PDT drug for imaging and treatment of brain tumors. This agent incorporates a photosensitizer, PHOTOFRIN® (a complex mixture of porphyrin oligomers), into a polyacrylamide (PAA) core along with MRI contrast agents; it is further functionalized with PEG groups and the RGD targeting peptide on the surface of these nanoparticles (Figure 1.25a). Some of the major advantages of encapsulating PHOTOFRIN® within a nanoparticle are that it: (i) reduces the direct exposure of the drug to the physiological

milieu, (ii) reduces cutaneous photosensitivity post-treatment, and (iii) significantly reduces the wait time (from 24 h to 1 h) between intravenous injection of the drug and subsequent laser irradiation. The value of including a targeting ligand was demonstrated when RGD peptide-bearing nanoparticles showed higher accumulation in $\alpha_v\beta_3$-expressing cancer cells (MDA-435) than $\alpha_v\beta_3$-negative MCF-7 cells. *In vivo* pharmacokinetic behavior, studied in rats bearing 9L gliosarcoma by diffusional MRI, indicated a 50-fold increase in circulation half-life of nanoparticles after PEGylation and a significant increase in the diffusion coefficient of the water surrounding tumor cells, indicating a decrease in rate of tumor growth and shrinkage of tumor mass (Figure 1.25b). The efficiency of PHOTOFRIN® to generate killer singlet oxygen species and cause tumor cell death was also measured using a chemical test employing anthracene-9,10-dipropionic acid, disodium salt (ADPA)—in the presence of singlet oxygen species, the fluorescence of ADPA decays with time. Induction of cell death was also assessed by fluorescence microscopy on 9L gliomas transfected with PAA nanoparticles containing PHOTOFRIN® in varying amounts (1.25c). Overall, the nanoparticles were able to effectively kill brain tumors engrafted inside rats within 5 min of light exposure.

(a)

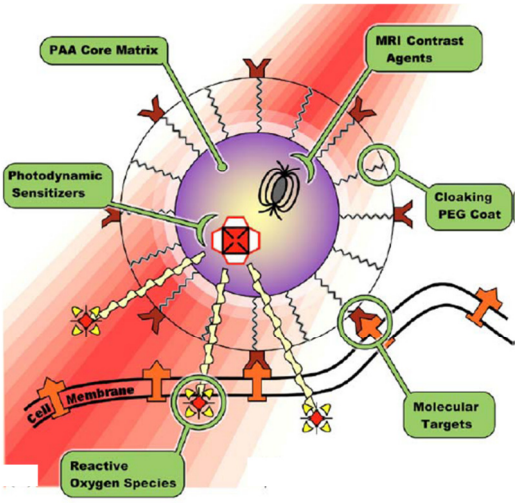

(b)

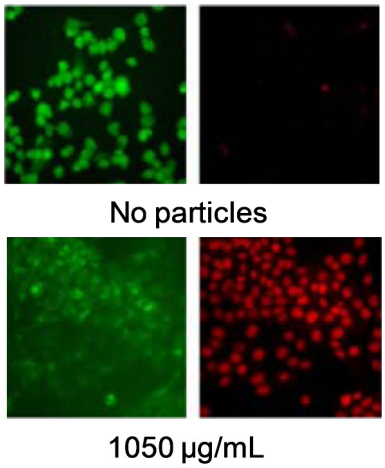

(c)

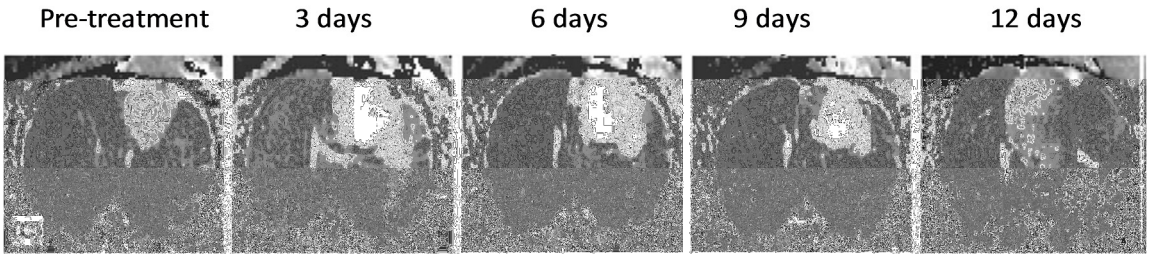

Figure 1-25: (a) Schematic of PAA-based multi-functional nanoparticles for photodynamic therapy; (b) *In vitro* cell kill test on 9L glioma cells that were untreated (top) or transfected with 1050 µg/mL of PAA particles containing PHOTOFRIN® (bottom). Live cells are stained with calcein acetoxymethylester (green) and dead cells with propidium iodide (red). (c) Diffusional MR imaging of rat 9L gliosarcoma model treated with PAA nanoparticles containing PHOTOFRIN® and irradiated with a laser for PDT. Treatment produced massive regional necrosis, demonstrated by large "bright" regions in the images, which resulted in shrinkage of the tumor mass. Re-growth occurred at 12 days post-treatment.

Figure adapted from Kopelman, R.; Koo, Y.-E. L.; Philbert, M.; Moffat, B. A.; Ramachandra Reddy, G.; McConville, P.; Hall, D. E.; Chenevert, T. L.; Bhojani, M. S.; Buck, S. M.;

Rehemtulla, A.; Ross, B. D. Multifunctional nanoparticle platforms for in vivo MRI enhancement and photodynamic therapy of a rat brain cancer, *J. Magn. Magn. Mater.* 2005, *293*, 404-410 with permission, Copyright Elsevier (2005).

Studies have shown that PDT can be promising for treatment of malignant brain tumors, for which more than 80% of the tumor growth recurs after therapy. Being a localized therapy, PDT has the potential to be very beneficial in this scenario.[68-72] A dose-dependent increase in survival rate of glioblastoma patients has also been shown, further suggesting that the future of this therapy is bright.

Reddy et al.[73] have synthesized PHOTOFRIN®- and superparamagnetic iron oxide-encapsulated uniform poly(acrylamide) (PAA) nanoparticles (~40 nm) decorated with PEG groups and a vascular homing and cell-penetrating F3 peptide on the surface which targets brain cancer cells (Figure 1.26a). Laser irradiation (630 nm) for 5 min induced up to 90% cell death 4 h after transfection (Figure 1.26b). *In vivo* administration to 9L glioma-bearing rats revealed that inclusion of PEG and targeting groups onto the surface increased the tumor half-life (from 39 min to 123 min) and T_2-weighted image contrast compared to non-targeted analogues.

(a) (b)

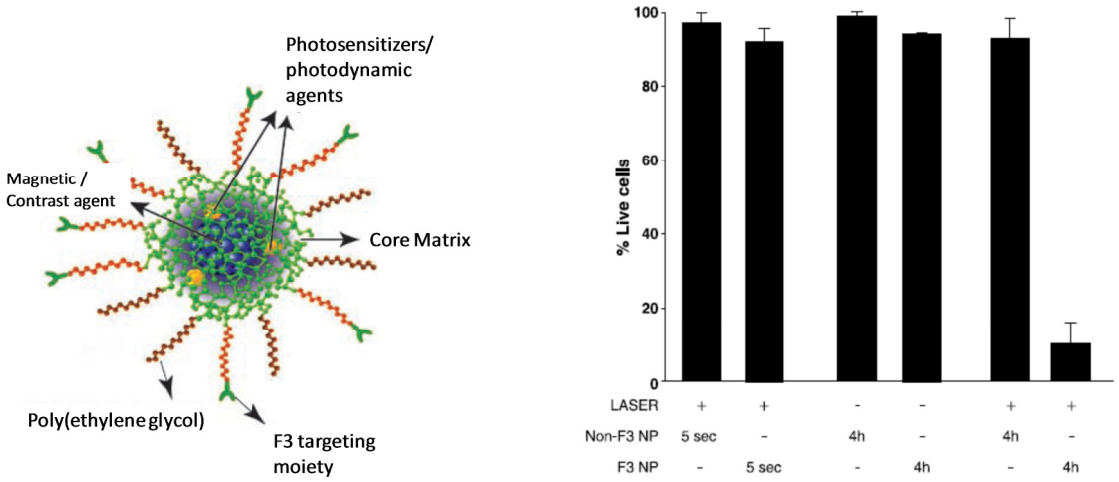

Figure 1-26: (a) Schematic of targeted PAA nanoparticles for PDT and diffusional MR imaging. (b) Cell viability studies performed on MDA-43 cells with PHOTOFRIN®- and iron oxide-encapsulated nanoparticles lacking ("Non-F3 NP") or containing ("F3 NP") the F3 targeting ligand. Only the combination of F3-containing nanoparticles incubated for 4 h and laser irradiation significant reduced the percentage of live cells.

Figure adapted and reprinted with permission from American Association for Cancer Research:Reddy, G. R.; Bhojani, M. S.; McConville, P.; Moody, J.; Moffat, B. A.; Hall, D. E.; Kim, G.; Koo, Y.-E. L.; Woolliscroft, M. J.; Sugai, J. V.; Johnson, T. D.; Philbert, M. A.; Kopelman, R.; Rehemtulla, A.; Ross, B. D., Vascular Targeted Nanoparticles for Imaging and Treatment of Brain Tumors, *Clin. Cancer Res.,* 2006, *12,* 6677-6686.

Another approach to introduce theranostic functionalities into a nanosystem is to covalently attach a palladium (Pd)-porphyrin chelate to mesoporous silica nanoparticles (MSNs) which are readily taken up by cells. Some of the important properties of MSNs are large surface area (~1000 m^2/g), uniform pore size (~3 nm), particle size (in the range of ~70-100 nm), ease of functionalization, large payload capacity, high cellular uptake, and low cytotoxicity. Because of

these properties, MSNs have several advantages over normal silica nanoparticles and, thus, are used in wide array of applications, including chemical catalysis, drug delivery, controlled release of therapeutics, and cell labeling. Pd-porphyrin has a long phosphorescence lifetime and has been used for *in vivo* oxygen sensing and imaging.[74,75] Cheng et al.[76] synthesized (Figure 1.27a and 1.27b) phosphorescent Pd-meso-tetra (4-carboxyphenyl) porphyrin (PdTPP) covalently embedded in MSNs (MSN-PdTPP) as theranostic agents for the imaging and treatment of breast cancer. The energy required for phosphorescence imaging is only 10^{-4}-10^{-5} times that required for conventional PDT. Also, the concentration of singlet oxygen species generated during oxygen sensing/imaging is much lower compared to that during conventional PDT and, thus, by changing the energy of photoirradiation, the functionalities of MSN-PdTPP can be 'switched' between a phosphorescence probe for oxygen sensing/imaging (diagnostics) and a photosensitizer for PDT (therapy). Breast cancer cells (MDA-MB-231) transfected with 25 µg MSN-PdTPP for 2 h at 37 °C, followed by photoirradiation (532 nm wavelength with energy 1.2 J/cm^2), showed a significant change in cell morphology and large extent of cell death indicated by high propidium iodide fluorescence (Figure 1.27c).

(a) (b)

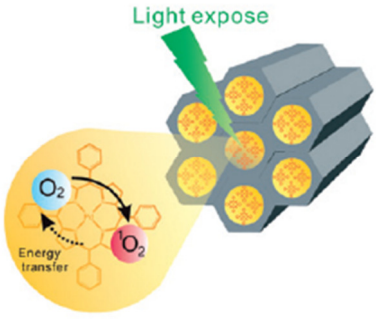

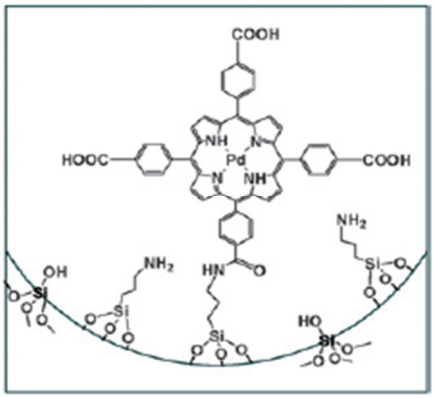

(c)

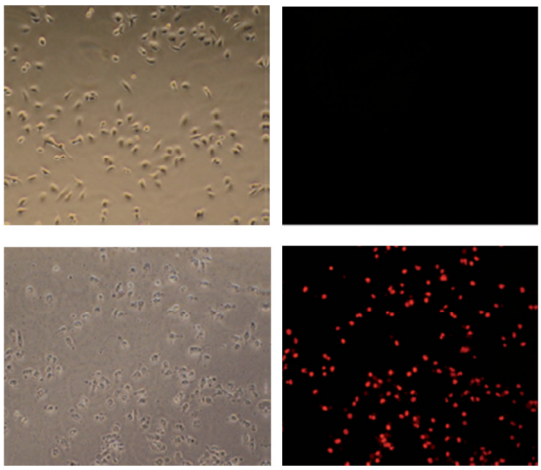

Figure 1-27: (a) Schematic of the mechanism of PDT with MSN-PdTPP. (b) The chemical structure of PdTPP covalently attached to MSN. (c) Propidium iodide (PI) staining of MDA-MB-231 cells treated with 25 μg of MSN-PdTPP at 37 °C for 2 h and then irradiated with a 532-nm laser. The left panels show the change in morphology of the cells before (top) and after (bottom) treatment, respectively. The right panels show red propidium iodide fluorescence (indicating dead cells) before (top) and after (bottom) treatment, respectively.

Figure adapted from Cheng, S.-H.; Lee, C.-H.; Yang, C.-S.; Tseng, F.-G.; Mou, C.-Y.; Lo, L.-W., (2009*)* Mesoporous silica nanoparticles functionalized with an oxygen-sensing probe for cell photodynamic therapy: potential cancer theranostics. *J. Mater. Chem. 19,* 1252-1257. Reproduced by permission of The Royal Society of Chemistry.

PDT is an FDA-approved first-line treatment for age-related macular degeneration and is routinely used for obstructive esophageal cancer and some forms of lung cancer.[77-79] One of the approaches for cancer treatment includes therapies that block or interrupt a specific cellular pathway or proteins involved in cell proliferation. One of these proteins is the Ki-67 protein (pKi-67), which is upregulated in highly proliferating cells during all active cell cycles (G1, S and G2, as well as mitosis). Rahmanzadeh et al.[80] used a non-cationic liposome-based vehicle

for delivering fluorescently-labeled (fluorescein isothiocyanate, FITC) antibodies, namely TuBB-9 and MIB-1, that recognize Ki-67 protein in two different states. Twenty four hours after transfection in ovarian cancer cells (OVCAR-5), TuBB-9-FITC- and MIB-1-FITC-containing liposome particles (particle size ~ 180 nm) were found to be localized in the nucleolar regions (Figure 1.28a). Irradiation with a 488-nm laser (5 J/cm^2 laser power) resulted in a significant decrease in cell viability for cells incubated with TuBB-9-FITC-labeled liposomes, but not MIB-1-FITC-labeled liposomes (Figure 1.28c). As expected, no significant toxicity was observed for various controls, including liposome-treated cells that were not irradiated as well as irradiated cells treated with TuBB-9-FITC alone (without the liposomal carrier).

(a)

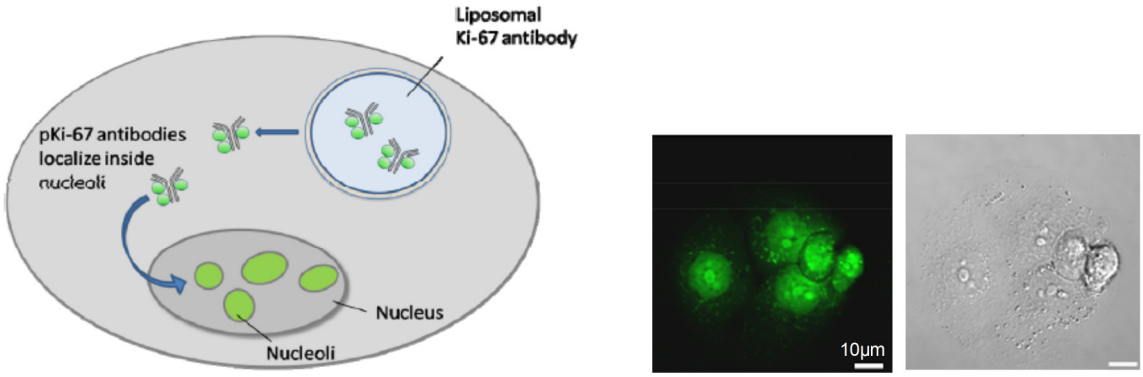

(b)

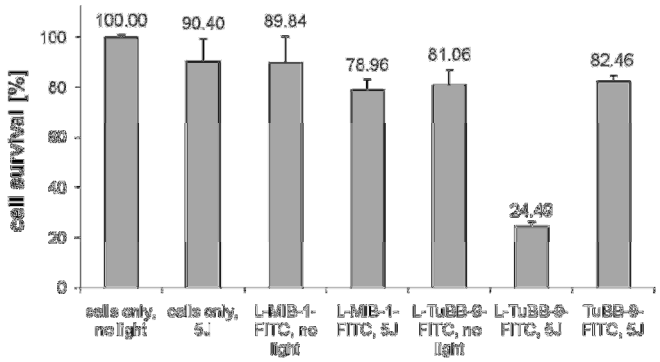

Figure 1-28: (a) Schematic and fluorescence micrograph of intracellular (nucleolar) localization of pKi-67-targeting liposomes. (b) An MTT cell toxicity assay performed on ovarian cancer (OVCAR-5) cells incubated with TuBB-9-FITC-labeled liposomes ('L-TuBB-9-FITC') indicated that more than 75% cells experienced death upon light irradiation (denoted '5J'); minimal cell death was observed to upon treatment with various controls.

Figure adapted from Rahmanzadeh, R.; Rai, P.; Gerdes, J.; Hasan, T., (2010*)* Targeted light-inactivation of the Ki-67 protein using theranostic liposomes leads to death of proliferating cells. *Proc. SPIE 7576,* 757602/757601-757602/757605 with permission from SPIE.

1.5. Combining Theranostic Use with Hyperthermia (Photothermal Ablation)

Hyperthermia, also called photothermal ablation, is a physical treatment for cancer involving the killing of cancer cells in the presence of heat. Hyperthermia leads to apoptotic cell death caused by heating of surrounding tissues or cells to a temperature of 42-46 °C; above 46 °C, photothermal ablation causes undesirable necrosis of surrounding cells.[81,82] With no chemical payload to deliver, hyperthermia is less prone to toxic side effects that often accompany chemotherapeutic agents.

Gold nanoparticles are more commonly used for hyperthermia than other heavy metals (such as silver or cobalt) due to the unique interaction of gold with light, which results in surface plasmon resonance (SPR). In the presence of oscillating electromagnetic radiations at a particular resonance frequency, free electrons in gold undergo collective coherent oscillations ('SPR oscillations') which can decay via heat emission.[83,84] Changing the size, shape, and refractive index (RI) of the material changes its SPR frequency. Ideally, this frequency is tuned in the near infrared (NIR) region. At NIR wavelengths, the absorption of innate biological fluorochromes and water is low[85] and, thus, the light can penetrate deeper into tissues without causing damage to surrounding healthy cells.

To combine imaging and therapy in the case of gold-containing nanoparticles, architectures with iron oxide cores and gold shells have been explored widely. Gold nanoparticles with iron oxide cores, such as magnetite (Fe_2O_4) or maghemite (γ-Fe_2O_4), can be imaged using MRI. The layer of gold surrounding the magnetic iron oxide particles helps to stabilize them from *in vivo* aggregation and reduces their toxicity. The desired NIR absorption frequency for gold nanoparticles can be achieved by coating them with silica, which has a high dielectric constant and, thus, helps to lower the absorption frequency towards NIR wavelengths.[83] Iron oxide particles impart a high T_2 relaxivity (good negative contrast for MRI) and, in the presence of a magnetic field, can be localized to the site of interest. This therapeutic targeting strategy is known as magnetic field-directed hyperthermia.[86]

As an example of magnetic field-directed hyperthermia, researchers have developed human epidermal growth receptor 2 (HER2)-targeted gold nanoparticles for breast cancer treatment. Kim et al.[87] designed magnetic gold nanoshells (Mag-GNS) consisting of a magnetic iron oxide (Fe_2O_4) and silica core surrounded by a 15-nm gold shell. For breast cancer targeting,

Mag-GNS functionalized with an antibody targeting HER-2/neu receptor ($Ab_{HER2/neu}$), a cell surface molecule that is overexpressed on breast cancer cells. SKBR3 breast cancer cells and lung cancer cells (H520 cells, which do not overexpress HER2/neu) were treated with $Ab_{HER2/neu}$–containing Mag-GNS for 2 h at 37 °C. Upon subsequent exposure to a femtosecond-long laser (800 nm) pulse, Mag-GNS-transfected SKBR3 cells exhibited significant cell death. T_2-weighted MR images of transfected SKBR3 cells and H520 cells showed higher image contrast for targeted particles than untransfected cells (Figure 1.29), with SKBR3 cells exhibiting enhanced contrast relative to H520 cells, as expected.

(a)

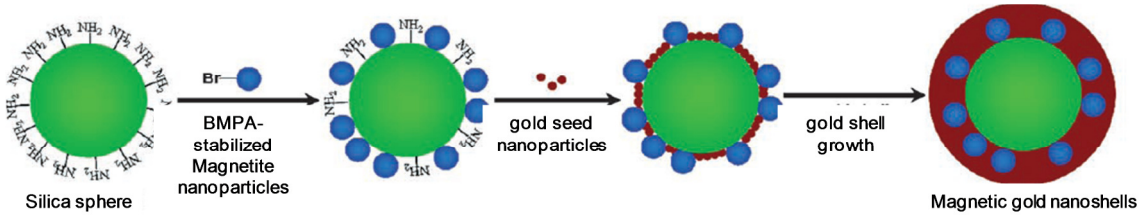

(b)

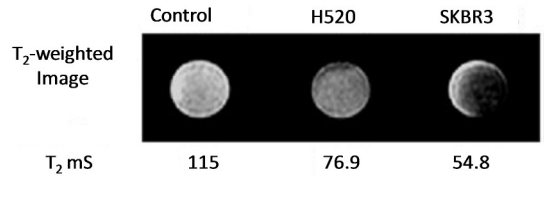

(c)

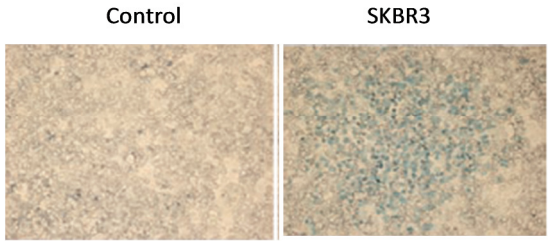

Figure 1-29: (a) Schematic of synthesis of magnetic gold-nanoshells (Mag-GNS); (b) T_2-weighted MR imaging of Mag-GNS-$Ab_{HER2/neu}$-transfected SKBR3 and H520 cells, compared to untransfected SKBR3 cells ("Control"). (b) A change in morphology of SKBR3 cells upon transfection with Mag-GNS- $Ab_{HER2/neu}$ and subsequent irradiation with a femtosecond-pulse laser (800 nm for 10 s); dead cells were stained with trypan blue.

Figure adapted from Kim, J.; Park, S.; Lee, J. E.; Jin, S. M.; Lee, J. H.; Lee, I. S.; Yang, I.; Kim, J.-S.; Kim, S. K.; Cho, M.-H.; Hyeon, T. Designed fabrication of multifunctional magnetic gold nanoshells and their application to magnetic resonance imaging and photothermal therapy, *Angew. Chem., Int. Ed.* 2006, *45*, 7754-7758. Copyright Wiley-VCH Verlag GmbH & Co. KGaA. Reproduced with permission.

In a related study, Lim et al.[88] synthesized core-shell type structures in which 9-11 nm magnetic iron oxide cores were covered with 2-3-nm hollow gold nanoshells (HGNS); the resulting materials (Fe_3O_4@Au) were surface-functionalized with anti-HER2 monoclonal antibodies (Figure 1.30a). The specificity of the antibody attached on the surface of HGNS (Fe_2O_3@Au) was tested in SKBR3 (HER2-positive) and MCF-7 (HER2-negative) cancer cells by further labeling these particles with tetramethyl rhodamine iso-thiocyanate (TRITC); TRITC fluorescence was only seen in SKBR3 cells, implicating HER2 engagement in the uptake of these nanoparticles. Photothermal therapy performed on treated SKBR3 cells with an 808-nm laser resulted in cell death within 3 min of exposure without causing any damage to unexposed cells (Figure 1.30b).

(a)

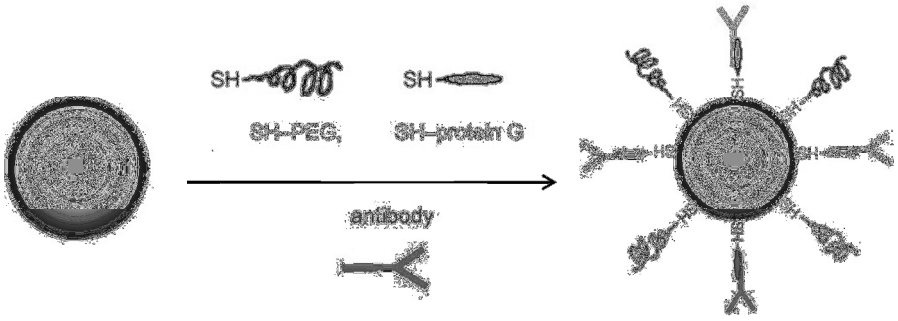

(b)

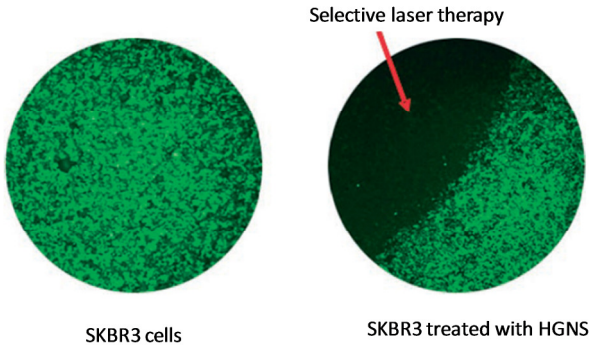

Figure 1-30: (a) Schematic of the synthesis of hollow gold nanoshells (HGNS) functionalized with iron oxide, a HER2-targeting antibody, and poly(ethylene glycol) (PEG). (b) SKBR3 cells incubated with the targeted HGNS (Fe_2O_3@Au) and stained with calcein-AM (green). Irradiation with an 808-nm laser resulted in a significant decrease in survival of treated cells.

Figure adapted from Lim, Y. T.; Cho, M. Y.; Kim, J. K.; Hwangbo, S.; Chung, B. H. Plasmonic magnetic nanostructure for bimodal imaging and photonic-based therapy of cancer cells, *ChemBioChem* 2007, *8*, 2204-2209. Copyright Wiley-VCH Verlag GmbH & Co. KGaA. Reproduced with permission.

Hybridization of $MnFe_2O_4$ with gold nanoparticles can help to combine MR imaging and hyperthermia treatment for cancer therapy. Recently, it has been shown that clustering of magnetic nanoparticles increases their MR properties.[89-91] Magnetic contrast agents consisting of magnetic kernels of manganese and iron oxide clusters were used to improve image contrast. Lee et al.[92] developed quadruple-layered theranostic agents (Figure 1.31a) for hyperthermia treatment by embedding a number of magnetic kernels in a silica layer, followed by coating with a layer of gold nanoparticles, and then finally incorporating a PEG layer and a targeting antibody, Erbitux (ERB), which binds to epidermal growth factor receptor (EGFR) that is overexpressed on certain cancer cells. T_2-weighted MR imaging of these multifunctional magnetic gold nanocomposites

(MGNCs), performed on a 1.5-T magnetic scanner, indicated a dose-dependent increase in relaxivity upon increase in MGNC concentration. The specificity of the ERB antibody for EGFR- expressing tumor cells was tested via MTT assay by adding ERB- vs. irrelevant antibody (IRR)-functionalized MGNCs to A431 (overexpress EGFR) and MCF7 (low EGFR expression) cells, followed by irradiation with a NIR laser (Figure 1.31b).

(a) (b)

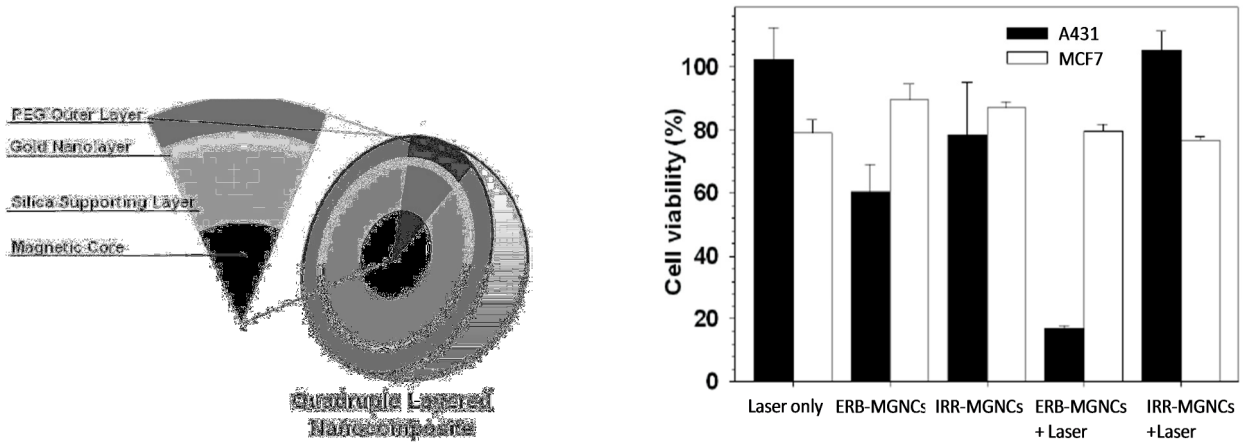

Figure 1-31: (a) Schematic of the quadruple-layered structure of magnetic-gold nanocomposites (MGNCs) targeting EGFR. (b) MTT assay shows the relative cell viability of A431 and MCF7 cells treated with ERB-MGNCs and IRR-MGNCs and irradiated with a NIR laser for 5 min. The combination of ERB-MGNCs in A431 cells resulted in the greatest observed reduction in cell viability.

Figure adapted from Lee, J.; Yang, J.; Ko, H.; Oh, S. J.; Kang, J.; Son, J.-H.; Lee, K.; Lee, S.-W.; Yoon, H.-G.; Suh, J.-S.; Huh, Y.-M.; Haam, S. Multifunctional magnetic gold nanocomposites: human epithelial cancer detection via magnetic resonance imaging and localized synchronous therapy, *Adv. Funct. Mater.* 2008, *18*, 258-264. Copyright Wiley-VCH Verlag GmbH & Co. KGaA. Reproduced with permission.

In 1957, Gilchrist and co workers[86] first introduced the concept of magnetic fluid hyperthermia (MFH), whereby magnetic particles, in the presence of a magnetic field, produce heat by hysteresis loss and, thus, can be used for hyperthermia treatment. Comes Franchini et al.[93] employed this technique to develop (Figure 1.32) bovine serum albumin (BSA)- and poly(lactic-co-glycolic acid) (PLGA)-coated magnetic nanocarriers containing a cobalt-iron oxide (PLGA-BSA-$CoFe_2O_4$) core. In the presence of a high-frequency magnetic field (168 kHz, 21 kA/m), these particles can heat the surrounding cells up to 48 °C. At these conditions, an impressive 82% cell death is induced within 1 h of treatment. It is proposed that introducing structural anisotropy (such as via cobalt) into the iron oxide magnetic nanoparticles increases their hyperthermia efficiency and possibly also their magnetic contrast property. *In vivo* studies on the brain and liver of rats indicated that these PLGA-BSA-$CoFe_2O_4$ particles show higher image contrast compared to a commercial contrast agent, Endorem®.

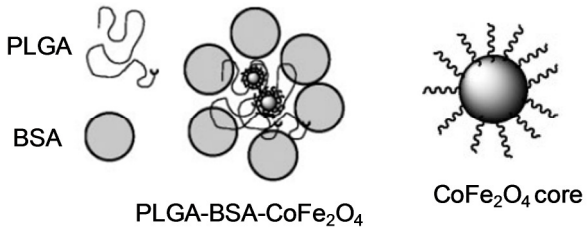

Figure 1-32: Schematic representation morphology of PLGA-BSA-$CoFe_2O_4$ nanoparticles for hyperthermia therapy.

Figure adapted from Comes Franchini, M.; Baldi, G.; Bonacchi, D.; Gentili, D.; Giudetti, G.; Lascialfari, A.; Corti, M.; Marmorato, P.; Ponti, J.; Micotti, E.; Guerrini, U.; Sironi, L.; Gelosa, P.; Ravagli, C.; Ricci, A., Bovine Serum Albumin-Based Magnetic Nanocarrier for MRI Diagnosis and Hyperthermic Therapy: A Potential Theranostic Approach Against Cancer, *Small* 2010, *6*, 366-370. Copyright Wiley-VCH Verlag GmbH & Co. KGaA. Reproduced with permission.

1.6. Radiation Therapy and Theranostics

Radiation therapy uses high-energy radiations, such as X-rays, gamma rays and charged particles, to kill target cancer cells.[94] Radiation can be received externally or internally, the latter occurring via a dosage of radioactive materials which emit radiation upon their decay. These high-energy ionizing radiations cause irreversible damage to DNA, thereby inducing cell death. Another mechanism involved may be generation of free radicals, which can also cause apoptosis of the cells. If employed without any cell surface targeting groups, radiation therapy does not have any specificity towards cancer cells over normal cells. Radiation therapy can be administered as a stand-alone therapy or in combination with other types of cancer treatment, such as chemotherapy or surgical intervention.

Due to increasing concerns associated with albumin-based radiopharmaceuticals (HIV, hepatitis C), Saatchi et al.[95] developed an alternative approach based on biodegradable poly(L-lactide) (PLL) microspheres. PLL microspheres (size 0.5-2 μm) were functionalized with a microSPECT/ CT contrast agent, [^{99m}Tc], and decorated with PEG via a double-emulsion solvent evaporation technique. These PEGylated PLL microspheres showed significant accumulation in the liver and the reticuloendothelial system (RES), likely due to macrophage clearance of these large microspheres. When chelated to β-emitting radionuclides such as [^{90}Y], these microspheres can be utilized for radioembolization therapy of liver tumors, uterine fibroids, meningiomas and arteriovenous malformations, as well as local treatments of leftover and recurring disease.

Radiation therapy can also be performed by delivering radionuclide-functionalized radiopeptides to the tumor cells. Radiopeptides are attractive options in the field of cancer therapeutics because they have rapid clearance, rapid tissue penetration, target accessibility, low antigenicity and ease of synthesis. For patients with inoperable or metastasized tumors, selective

receptor-targeting radiopeptides can be a useful therapy. Radiopeptides labeled with γ- or positron-emitting radionuclides can easily be visualized with diagnostic imaging techniques, like positron emission tomography (PET), or single-photon emission computed tomography (SPECT). These radiopeptides can be labeled with γ-emitters like indium-111 [^{111}In] or [^{99m}Tc] for SPECT imaging and/or positron emitters such as gallium-68 [^{68}Ga] or fluorine-18 [^{18}F] for PET imaging. In addition, when labeled with β-emitting species (such as yttrium-90 [^{90}Y] and lutetium-177 [^{177}Lu]), they can effectively eradicate the targeted tumor cells.[96]

Lastly, radiopeptides that target the somatostatin receptor (which is overexpressed on the surface of a majority of neuroendocrine tumors) show promise for both imaging and therapy of tumors in which other therapies are ineffective. Somatostatin analogues containing FDA-approved DTPA-octreotide (DTPA = diethylene triamine pentaacetic acid), DOTA-octreotide (DOTA = 1,4,7,10-tetraazacyclododecane-1,4,7,10-tetraacetic acid), DTPA-Tyr^3-octreotide/octreotate, and DOTA-Tyr^3-octreotide/octreotate have high binding affinity for the subtype 2 (sst_2) of somatostatin receptors (Figure 1.33).[97,98]

Octreotide	D-Phe-Cys-Phe-D-Trp-Lys-Thr-Cys-Thr (ol)
[Tyr^3]octreotide	D-Phe-Cys-Tyr-D-Trp-Lys-Thr-Cys-Thr (ol)
[Tyr^3]octreotate	D-Phe-Cys-Tyr-D-Trp-Lys-Thr-Cys-Thr

Figure 1-33: Structures of somatostatin analogues: octreotide, Tyr^3-octreotide and Tyr^3-octreotate.

Figure adapted from de Jong, M.; Breeman, W. A. P.; Kwekkeboom, D. J.; Valkema, R.; Krenning, E. P., (2009*)* Tumor Imaging and Therapy Using Radiolabeled Somatostatin Analogues. *Acc. Chem. Res. 42,* 873-880. with permission from ACS.

1.7. Conclusions:

The field of theranostics remains relatively young but is developing at an incredibly fast rate. Researchers have developed numerous nanoparticle-based systems that can be used for therapy, as in the cases of hyperthermia or radiation therapy, and/or for delivery of chemotherapeutic drugs and diagnostic imaging agents. Several approaches include multi-imaging modalities that can facilitate tracking of nanoparticles both *in vitro* and *in vivo*. To monitor the therapy and response to therapy at a cellular level, the use of fluorescent labeling agents, such as organic fluorescent dyes or quantum dots, can permit achievement of high-resolution images delineating different organelles inside the cell. However, for *in vivo* purposes, modalities such as PET or SPECT agents and MRI contrast agents are preferred to overcome problems of background fluorescence and photobleaching.

Theranostic agents can play major roles both in early-stage drug development and as clinical-stage therapeutic-containing drug candidates. *In vitro* imaging agents are important during early development, such as for modification of chemical structure and architecture to fine-tune drug properties. However, *in vivo* agents are important for advanced studies that may be promising for clinical trials. Until now, theranostics have not reached clinical trials, this field is, however, relatively young and issues related to ambiguity and/or difference between the optimum concentrations for the therapeutic and imaging agents are in the process of being resolved. For example, for systems with nuclear imaging agents, such as 2-[^{18}F]-2-deoxyglucose (FDG), and anticancer chemotherapeutics, such as doxorubicin, the dosages required for success of the individual modalities are vastly (several orders-of-magnitude) different. Systems with MRI agents based on gadolinium and therapeutic drugs can face similar problems because of the inherent low sensitivity of MRI. The minimum dosage required for Gd-based imaging agents,

such as Magnevist®, is 100 mg/kg, which is typically considerably higher than the appropriate therapeutic dose. These mismatches can be overcome by exploring different combinations of diagnostic and therapeutic agents, developing new drugs that are potent at lower concentrations, and creating more advanced and sensitive imaging techniques that match the dose required for therapy and imaging. Research into theranostics that can overcome these obstacles and be suitable for important applications remains rich, and the time before theranostics begin clinical evaluation is likely to be short.

1.8. References

(1) Funkhouser, J. *Current Drug Discovery* **2002**, Reintroducing Pharma: theranostic revolution, *2*, 17-19.

(2) McCarthy Jason, R. *Nanomedicine (Lond)* **2009**, The future of theranostic nanoagents, *4*, 693-5.

(3) McCarthy, J. R. *Adv. Drug Delivery Rev.* **2010**, Multifunctional agents for concurrent imaging and therapy in cardiovascular disease, *62*, 1023-1030.

(4) Sumer, B.; Gao, J. *Nanomedicine (London, England)* **2008**, Theranostic nanomedicine for cancer, *3*, 137-40.

(5) Warenius, H. M. *Expert Opinion on Medical Diagnostics* **2009**, Technological challenges of theranostics in oncology, *3*, 381-393.

(6) Matsumura, Y.; Oda, T.; Maeda, H. *Gan to kagaku ryoho. Cancer & chemotherapy* **1987**, General mechanism of intratumor accumulation of macromolecules: advantage of macromolecular therapeutics, *14*, 821-9.

(7) Iyer, A. K.; Khaled, G.; Fang, J.; Maeda, H. *Drug Discovery Today* **2006**, Exploiting the enhanced permeability and retention effect for tumor targeting, *11*, 812-818.

(8) Niidome, T.; Huang, L. *Gene Therapy* **2002**, Gene Therapy Progress and Prospects: Nonviral Vectors, *9*, 1647-1652.

(9) Heilbronn, R.; Weger, S. *Handb. Exp. Pharmacol.* **2010**, Viral vectors for gene transfer: current status of gene therapeutics, *197*, 143-170.

(10) Scollay, R. *Ann. N.Y. Acad. Sci.* **2001**, Gene therapy: A brief overview of the past, present, and future, *953*, 26-30.

(11) Thomas, C. E.; Ehrhardt, A.; Kay, M. A. *Nature Reviews Genetics* **2003**, Progress and problems with the use of viral vectors for gene therapy, *4*, 346-358.

(12) Akhtar, S. *Gene Therapy* **2006**, Non-viral cancer gene therapy: Beyond delivery, *13*, 739-740.

(13) Medintz, I. L.; Uyeda, H. T.; Goldman, E. R.; Mattoussi, H. *Nature Materials* **2005**, Quantum dot bioconjugates for imaging, labelling and sensing, *4*, 435-446.

(14) Godbey, W. T.; Wu, K. K.; Mikos, A. G. *Proc. Natl. Acad. Sci. U. S. A.* **1999**, Tracking the intracellular path of poly(ethylenimine)/DNA complexes for gene delivery, *96*, 5177-5181.

(15) Ho, Y.-P.; Chen, H. H.; Leong, K. W.; Wang, T.-H. *J. Controlled Release* **2006**, Evaluating the intracellular stability and unpacking of DNA nanocomplexes by quantum dots-FRET, *116*, 83-89.

(16) Lucas, B.; Remaut, K.; Sanders, N. N.; Braeckmans, K.; De Smedt, S. C.; Demeester, J. *Biochemistry* **2005**, Studying the intracellular dissociation of polymer-oligonucleotide complexes by dual color fluorescence fluctuation spectroscopy and confocal imaging, *44*, 9905-9912.

(17) Matsumoto, Y.; Itaka, K.; Yamasoba, T.; Kataoka, K. *Journal of Gene Medicine* **2009**, Intranuclear fluorescence resonance energy transfer analysis of plasmid DNA decondensation from nonviral gene carriers, *11*, 615-623.

(18) Stryer, L. *Annu. Rev. Biochem.* **1978**, Fluorescence energy transfer as a spectroscopic ruler, *47*, 819-46.

(19) Schwille, P. *Cell Biochem. Biophys.* **2001**, Fluorescence correlation spectroscopy and its potential for intracellular applications, *34*, 383-408.

(20) Resch-Genger, U.; Grabolle, M.; Cavaliere-Jaricot, S.; Nitschke, R.; Nann, T. *Nature Methods* **2008**, Quantum dots versus organic dyes as fluorescent labels, *5*, 763-775.

(21) Remaut, K.; Lucas, B.; Raemdonck, K.; Braeckmans, K.; Demeester, J.; De Smedt, S. C. *J. Controlled Release* **2007**, Can we better understand the intracellular behavior of DNA nanoparticles by fluorescence correlation spectroscopy?, *121*, 49-63.

(22) Correa-Duarte, M. A.; Giersig, M.; Liz-Marzan, L. M. *Chem. Phys. Lett.* **1998**, Stabilization of CdS semiconductor nanoparticles against photodegradation by a silica coating procedure, *286*, 497-501.

(23) Chen, A. A.; Derfus, A. M.; Khetani, S. R.; Bhatia, S. N. *Nucleic Acids Res.* **2005**, Quantum dots to monitor RNAi delivery and improve gene silencing, *33*, e190/1-e190/8.

(24) Derfus, A. M.; Chen, A. A.; Min, D.-H.; Ruoslahti, E.; Bhatia, S. N. *Bioconjugate Chem.* **2007**, Targeted Quantum Dot Conjugates for siRNA Delivery, *18*, 1391-1396.

(25) Tan, W. B.; Jiang, S.; Zhang, Y. *Biomaterials* **2007**, Quantum-dot based nanoparticles for targeted silencing of HER2/neu gene via RNA interference, *28*, 1565-1571.

(26) Prigodich, A. E.; Seferos, D. S.; Massich, M. D.; Giljohann, D. A.; Lane, B. C.; Mirkin, C. A. *ACS nano* **2009**, Nano-flares for mRNA regulation and detection, *3*, 2147-2152.

(27) Bryson, J. M.; Fichter, K. M.; Chu, W.-J.; Lee, J.-H.; Li, J.; Madsen, L. A.; McLendon, P. M.; Reineke, T. M. *Proc. Natl. Acad. Sci. U. S. A.* **2009**, Polymer beacons for luminescence and magnetic resonance imaging of DNA delivery, *106*, 16913-16918.

(28) Ichikawa, T.; Hoegemann, D.; Saeki, Y.; Tyminski, E.; Terada, K.; Weissleder, R.; Chiocca, E. A.; Basilion, J. P. *Neoplasia (New York, NY, United States)* **2002**, MRI of transgene expression: correlation to therapeutic gene expression, *4*, 523-530.

(29) Moore, A.; Josephson, L.; Bhorade, R. M.; Basilion, J. P.; Weissleder, R. *Radiology (Oak Brook, IL, United States)* **2001**, Human transferrin receptor gene as a marker gene for MR imaging, *221*, 244-250.

(30) Weissleder, R.; Moore, A.; Mahmood, U.; Bhorade, R.; Benveniste, H.; Chiocca, E. A.; Basilion, J. P. *Nature Medicine (New York)* **2000**, In vivo magnetic resonance imaging of transgene expression, *6*, 351-354.

(31) Park, I.-K.; Ng, C.-P.; Wang, J.; Chu, B.; Yuan, C.; Zhang, S.; Pun, S. H. *Biomaterials* **2008**, Determination of nanoparticle vehicle unpackaging by MR imaging of a T2 magnetic relaxation switch, *29*, 724-732.

(32) Dubertret, B.; Skourides, P.; Norris, D. J.; Noireaux, V.; Brivanlou, A. H.; Libchaber, A. *Science (Washington, DC, United States)* **2002**, In vivo imaging of quantum dots encapsulated in phospholipid micelles, *298*, 1759-1762.

(33) Medarova, Z.; Pham, W.; Farrar, C.; Petkova, V.; Moore, A. *Nature medicine* **2007**, In vivo imaging of siRNA delivery and silencing in tumors, *13*, 372-7.

(34) Hu-Lieskovan, S.; Heidel, J. D.; Bartlett, D. W.; Davis, M. E.; Triche, T. J. *Cancer Research* **2005**, Sequence-Specific Knockdown of EWS-FLI1 by Targeted, Nonviral Delivery of Small Interfering RNA Inhibits Tumor Growth in a Murine Model of Metastatic Ewing's Sarcoma, *65*, 8984-8992.

(35) Pun, S. H.; Tack, F.; Bellocq, N. C.; Cheng, J.; Grubbs, B. H.; Jensen, G. S.; Davis, M. E.; Brewster, M.; Janicot, M.; Janssens, B.; Floren, W.; Bakker, A. *Cancer Biol. Ther.* **2004**, Targeted delivery of RNA-cleaving DNA enzyme (DNAzyme) to tumor tissue by transferrin-modified, cyclodextrin-based particles, *3*, 641-650.

(36) Bartlett, D. W.; Su, H.; Hildebrandt, I. J.; Weber, W. A.; Davis, M. E. *Proc. Natl. Acad. Sci. U. S. A.* **2007**, Impact of tumor-specific targeting on the biodistribution and efficacy of siRNA nanoparticles measured by multimodality in vivo imaging, *104*, 15549-15554.

(37) Schneider, S.; Lenz, D.; Holzer, M.; Palme, K.; Suess, R. *J. Controlled Release* **2010**, Intracellular FRET analysis of lipid/DNA complexes using flow cytometry and fluorescence imaging techniques, *145*, 289-296.

(38) Kuo Phillip, H. *J Am Coll Radiol* **2008**, Gadolinium-containing MRI contrast agents: important variations on a theme for NSF, *5*, 29-35.

(39) Pan, D.; Caruthers, S. D.; Hu, G.; Senpan, A.; Scott, M. J.; Gaffney, P. J.; Wickline, S. A.; Lanza, G. M. *J. Am. Chem. Soc.* **2008**, Ligand-Directed Nanobialys as Theranostic Agent for Drug Delivery and Manganese-Based Magnetic Resonance Imaging of Vascular Targets, *130*, 9186-9187.

(40) Shin, J.; Anisur, R. M.; Ko, M. K.; Im, G. H.; Lee, J. H.; Lee, I. S. *Angew. Chem. Int. Ed.* **2009**, Hollow manganese oxide nanoparticles as multifunctional agents for magnetic resonance imaging and drug delivery, *48*, 321-324.

(41) Senpan, A.; Caruthers, S. D.; Rhee, I.; Mauro, N. A.; Pan, D.; Hu, G.; Scott, M. J.; Fuhrhop, R. W.; Gaffney, P. J.; Wickline, S. A.; Lanza, G. M. *ACS nano* **2009**, Conquering the Dark Side: Colloidal Iron Oxide Nanoparticles, *3*, 3917-3926.

(42) Barth, B. M.; Sharma, R.; Altinoglu, E. I.; Morgan, T. T.; Shanmugavelandy, S. S.; Kaiser, J. M.; McGovern, C.; Matters, G. L.; Smith, J. P.; Kester, M.; Adair, J. H. *ACS nano* **2010**, Bioconjugation of Calcium Phosphosilicate Composite Nanoparticles for Selective Targeting of Human Breast and Pancreatic Cancers In Vivo, *4*, 1279-1287.

(43) Kester, M.; Heakal, Y.; Fox, T.; Sharma, A.; Robertson, G. P.; Morgan, T. T.; Altinoglu, E. I.; Tabakovic, A.; Parette, M. R.; Rouse, S.; Ruiz-Velasco, V.; Adair, J. H. *Nano Lett.* **2008**, Calcium Phosphate Nanocomposite Particles for In Vitro Imaging and Encapsulated Chemotherapeutic Drug Delivery to Cancer Cells, *8*, 4116-4121.

(44) Morgan, T. T.; Muddana, H. S.; Altinoglu, E. I.; Rouse, S. M.; Tabakovic, A.; Tabouillot, T.; Russin, T. J.; Shanmugavelandy, S. S.; Butler, P. J.; Eklund, P. C.; Yun, J. K.; Kester, M.; Adair, J. H. *Nano Lett.* **2008**, Encapsulation of Organic Molecules in Calcium Phosphate Nanocomposite Particles for Intracellular Imaging and Drug Delivery, *8*, 4108-4115.

(45) Muddana, H. S.; Morgan, T. T.; Adair, J. H.; Butler, P. J. *Nano Lett.* **2009**, Photophysics of Cy3-Encapsulated Calcium Phosphate Nanoparticles, *9*, 1559-1566.

(46) Shenoy, D.; Little, S.; Langer, R.; Amiji, M. *Pharm. Res.* **2005**, Poly(Ethylene Oxide)-Modified Poly(beta -Amino Ester) Nanoparticles as a pH-Sensitive System for Tumor-Targeted Delivery of Hydrophobic Drugs: Part 2. In Vivo Distribution and Tumor Localization Studies, *22*, 2107-2114.

(47) Shenoy, D.; Little, S.; Langer, R.; Amiji, M. *Molecular Pharmaceutics* **2005**, Poly(ethylene oxide)-Modified Poly(beta -amino ester) Nanoparticles as a pH-Sensitive System for Tumor-Targeted Delivery of Hydrophobic Drugs. 1. In Vitro Evaluations, *2*, 357-366.

(48) Chen, W.; Xu, N.; Xu, L.; Wang, L.; Li, Z.; Ma, W.; Zhu, Y.; Xu, C.; Kotov, N. A. *Macromol. Rapid Commun.* **2010,** Multifunctional Magnetoplasmonic Nanoparticle Assemblies for Cancer Therapy and Diagnostics (Theranostics), *31*, 228-236.

(49) Xie, J.; Chen, K.; Huang, J.; Lee, S.; Wang, J.; Gao, J.; Li, X.; Chen, X. *Biomaterials* **2010**, PET/NIRF/MRI triple functional iron oxide nanoparticles, *31*, 3016-3022.

(50) Liong, M.; Lu, J.; Kovochich, M.; Xia, T.; Ruehm, S. G.; Nel, A. E.; Tamanoi, F.; Zink, J. I. *ACS nano* **2008**, Multifunctional Inorganic Nanoparticles for Imaging, Targeting, and Drug Delivery, *2*, 889-896.

(51) Guthi, J. S.; Yang, S.-G.; Huang, G.; Li, S.; Khemtong, C.; Kessinger, C. W.; Peyton, M.; Minna, J. D.; Brown, K. C.; Gao, J. *Molecular Pharmaceutics* **2010**, MRI-Visible Micellar Nanomedicine for Targeted Drug Delivery to Lung Cancer Cells, *7*, 32-40.

(52) Nasongkla, N.; Bey, E.; Ren, J.; Ai, H.; Khemtong, C.; Guthi Jagadeesh, S.; Chin, S.-F.; Sherry, A. D.; Boothman David, A.; Gao, J. *Nano Lett.* **2006**, Multifunctional polymeric micelles as cancer-targeted, MRI-ultrasensitive drug delivery systems, *6*, 2427-30.

(53) Santra, S.; Kaittanis, C.; Grimm, J.; Perez, J. M. *Small (Weinheim an der Bergstrasse, Germany)* **2009**, Drug/Dye-Loaded, Multifunctional Iron Oxide Nanoparticles for Combined Targeted Cancer Therapy and Dual Optical/Magnetic Resonance Imaging, *5*, 1862-1868.

(54) Kohler, N.; Sun, C.; Wang, J.; Zhang, M. *Langmuir* **2005**, Methotrexate-Modified Superparamagnetic Nanoparticles and Their Intracellular Uptake into Human Cancer Cells, *21*, 8858-8864.

(55) Das, M.; Mishra, D.; Dhak, P.; Gupta, S.; Maiti, T. K.; Basak, A.; Pramanik, P. *Small (Weinheim an der Bergstrasse, Germany)* **2009**, Biofunctionalized, Phosphonate-Grafted, Ultrasmall Iron Oxide Nanoparticles for Combined Targeted Cancer Therapy and Multimodal Imaging, *5*, 2883-2893.

(56) Kim, J.; Kim, H. S.; Lee, N.; Kim, T.; Kim, H.; Yu, T.; Song, I. C.; Moon, W. K.; Hyeon, T. *Angew. Chem. Int. Ed.* **2008**, Multifunctional uniform nanoparticles composed of a magnetite nanocrystal core and a mesoporous silica shell for magnetic resonance and fluorescence imaging and for drug delivery, *47*, 8438-8441.

(57) Gopalakrishnan, G.; Danelon, C.; Izewska, P.; Prummer, M.; Bolinger, P.-Y.; Geissbuhler, I.; Demurtas, D.; Dubochet, J.; Vogel, H. *Angew. Chem. Int. Ed.* **2006**, Multifunctional lipid/quantum dot hybrid nanocontainers for controlled targeting of live cells, *45*, 5478-5483.

(58) Michalet, X.; Pinaud, F. F.; Bentolila, L. A.; Tsay, J. M.; Doose, S.; Li, J. J.; Sundaresan, G.; Wu, A. M.; Gambhir, S. S.; Weiss, S. *Science (Washington, DC, U. S.)* **2005**, Quantum Dots for Live Cells, in Vivo Imaging, and Diagnostics, *307*, 538-544.

(59) Yao, J.; Larson, D. R.; Vishwasrao, H. D.; Zipfel, W. R.; Webb, W. W. *Proc. Natl. Acad. Sci. U. S. A.* **2005**, Blinking and nonradiant dark fraction of water-soluble quantum dots in aqueous solution, *102*, 14284-14289.

(60) Bagalkot, V.; Zhang, L.; Levy-Nissenbaum, E.; Jon, S.; Kantoff, P. W.; Langer, R.; Farokhzad, O. C. *Nano Lett.* **2007**, Quantum Dot-Aptamer Conjugates for Synchronous Cancer Imaging, Therapy, and Sensing of Drug Delivery Based on Bi-Fluorescence Resonance Energy Transfer, *7*, 3065-3070.

(61) McCarthy, J. R.; Jaffer, F. A.; Weissleder, R. *Small (Weinheim an der Bergstrasse, Germany)* **2006**, A macrophage-targeted theranostic nanoparticle for biomedical applications, *2*, 983-987.

(62) Denis, M. C.; Mahmood, U.; Benoist, C.; Mathis, D.; Weissleder, R. *Proc. Natl. Acad. Sci. U. S. A.* **2004**, Imaging inflammation of the pancreatic islets in type 1 diabetes, *101*, 12634-12639.

(63) Jaffer Farouc, A.; Nahrendorf, M.; Sosnovik, D.; Kelly Kimberly, A.; Aikawa, E.; Weissleder, R. *Molecular imaging official journal of the Society for Molecular Imaging* **2006**, Cellular imaging of inflammation in atherosclerosis using magnetofluorescent nanomaterials, *5*, 85-92.

(64) Kircher, M. F.; Mahmood, U.; King, R. S.; Weissleder, R.; Josephson, L. *Cancer Research* **2003**, A Multimodal Nanoparticle for Preoperative Magnetic Resonance Imaging and Intraoperative Optical Brain Tumor Delineation, *63*, 8122-8125.

(65) Pande, A. N.; Kohler, R. H.; Aikawa, E.; Weissleder, R.; Jaffer, F. A. *Journal of biomedical optics* **2006**, Detection of macrophage activity in atherosclerosis in vivo using multichannel, high-resolution laser scanning flourescence microscopy, *11*, 021009/1-021009/7.

(66) Weissleder, R.; Kelly, K.; Sun, E. Y.; Shtatland, T.; Josephson, L. *Nat. Biotechnol.* **2005**, Cell-specific targeting of nanoparticles by multivalent attachment of small molecules, *23*, 1418-1423.

(67) Kopelman, R.; Koo, Y.-E. L.; Philbert, M.; Moffat, B. A.; Ramachandra Reddy, G.; McConville, P.; Hall, D. E.; Chenevert, T. L.; Bhojani, M. S.; Buck, S. M.; Rehemtulla, A.; Ross, B. D. *J. Magn. Magn. Mater.* **2005**, Multifunctional nanoparticle platforms for in vivo MRI enhancement and photodynamic therapy of a rat brain cancer, *293*, 404-410.

(68) Kaye, A. H.; Morstyn, G.; Brownbill, D. *Journal of neurosurgery* **1987**, Adjuvant high-dose photoradiation therapy in the treatment of cerebral glioma: a phase 1-2 study, *67*, 500-5.

(69) Kostron, H.; Weiser, G.; Fritsch, E.; Grunert, V. *Photochem. Photobiol.* **1987**, Photodynamic therapy of malignant brain tumors: clinical and neuropathological results, *46*, 937-43.

(70) Muller Paul, J.; Wilson Brian, C. *Lasers Surg Med* **2006**, Photodynamic therapy of brain tumors--a work in progress, *38*, 384-9.

(71) Perria, C.; Capuzzo, T.; Cavagnaro, G.; Datti, R.; Francaviglia, N.; Rivano, C.; Tercero, V. E. *Journal of neurosurgical sciences* **1980**, Fast attempts at the photodynamic treatment of human gliomas, *24*, 119-29.

(72) Popovic, E. A.; Kaye, A. H.; Hill, J. S. *Seminars in surgical oncology* **1995**, Photodynamic therapy of brain tumors, *11*, 335-45.

(73) Reddy, G. R.; Bhojani, M. S.; McConville, P.; Moody, J.; Moffat, B. A.; Hall, D. E.; Kim, G.; Koo, Y.-E. L.; Woolliscroft, M. J.; Sugai, J. V.; Johnson, T. D.; Philbert, M. A.; Kopelman, R.; Rehemtulla, A.; Ross, B. D. *Clinical Cancer Research* **2006**, Vascular Targeted Nanoparticles for Imaging and Treatment of Brain Tumors, *12*, 6677-6686.

(74) Lo, L.-W.; Koch, C. J.; Wilson, D. F. *Anal. Biochem.* **1996**, Calibration of oxygen-dependent quenching of the phosphorescence of Pd-meso-tetra (4-carboxyphenyl) porphine: a phosphor with general application for measuring oxygen concentration in biological systems, *236*, 153-60.

(75) Vinogradov, S. A.; Wilson, D. F. *Biophys. J.* **1994**, Phosphorescence lifetime analysis with a quadratic programming algorithm for determining quencher distributions in heterogeneous systems, *67*, 2048-59.

(76) Cheng, S.-H.; Lee, C.-H.; Yang, C.-S.; Tseng, F.-G.; Mou, C.-Y.; Lo, L.-W. *J. Mater. Chem.* **2009**, Mesoporous silica nanoparticles functionalized with an oxygen-sensing probe for cell photodynamic therapy: potential cancer theranostics, *19*, 1252-1257.

(77) Dougherty, T. J.; Gomer, C. J.; Henderson, B. W.; Jori, G.; Kessel, D.; Korbelik, M.; Moan, J.; Peng, Q. *Journal of the National Cancer Institute* **1998**, Photodynamic therapy, *90*, 889-905.

(78) Price, M.; Terlecky, S. R.; Kessel, D. *Photochem. Photobiol.* **2009**, A role for hydrogen peroxide in the pro-apoptotic effects of photodynamic therapy, *85*, 1491-1496.

(79) Hasan, T.; Ortel, B.; Solban, N.; Pogue, B. W. *Cancer Med. 7* **2006**, Photodynamic therapy of cancer, 537-548.

(80) Rahmanzadeh, R.; Rai, P.; Gerdes, J.; Hasan, T. *Proceedings of SPIE* **2010**, Targeted light-inactivation of the Ki-67 protein using theranostic liposomes leads to death of proliferating cells, *7576*, 757602/1-757602/5.

(81) Hilger, I.; Andra, W.; Hergt, R.; Hiergeist, R.; Schubert, H.; Kaiser, W. A. *Radiology* **2001**, Electromagnetic heating of breast tumors in interventional radiology: in vitro and in vivo studies in human cadavers and mice, *218*, 570-5.

(82) Hilger, I.; Fruhauf, K.; Andra, W.; Hiergeist, R.; Hergt, R.; Kaiser Werner, A. *Acad Radiol* **2002**, Heating potential of iron oxides for therapeutic purposes in interventional radiology, *9*, 198-202.

(83) Jain, P. K.; Huang, X.; El-Sayed, I. H.; El-Sayed, M. A. *Acc. Chem. Res.* **2008**, Noble Metals on the Nanoscale: Optical and Photothermal Properties and Some Applications in Imaging, Sensing, Biology, and Medicine, *41*, 1578-1586.

(84) Melancon, M. P.; Lu, W.; Li, C. *MRS Bull.* **2009**, Gold-based magneto-optical nanostructures: challenges for in vivo applications in cancer diagnostics and therapy, *34*, 415-421.

(85) Mahmood, U.; Weissleder, R. *Mol. Cancer Ther.* **2003**, Near-infrared optical imaging of proteases in cancer, *2*, 489-496.

(86) Gilchrist, R. K.; Medal, R.; Shorey, W. D.; Hanselman, R. C.; Parrott, J. C.; Taylor, C. B. *Annals of surgery* **1957**, Selective inductive heating of lymph nodes, *146*, 596-606.

(87) Kim, J.; Park, S.; Lee, J. E.; Jin, S. M.; Lee, J. H.; Lee, I. S.; Yang, I.; Kim, J.-S.; Kim, S. K.; Cho, M.-H.; Hyeon, T. *Angew. Chem. Int. Ed.* **2006**, Designed fabrication of multifunctional magnetic gold nanoshells and their application to magnetic resonance imaging and photothermal therapy, *45*, 7754-7758, S7754/1.

(88) Lim, Y. T.; Cho, M. Y.; Kim, J. K.; Hwangbo, S.; Chung, B. H. *ChemBioChem* **2007**, Plasmonic magnetic nanostructure for bimodal imaging and photonic-based therapy of cancer cells, *8*, 2204-2209.

(89) Berret, J.-F.; Schonbeck, N.; Gazeau, F.; El Kharrat, D.; Sandre, O.; Vacher, A.; Airiau, M. *J Am Chem Soc* **2006**, Controlled clustering of superparamagnetic nanoparticles using block copolymers: design of new contrast agents for magnetic resonance imaging, *128*, 1755-61.

(90) Lee, J.-H.; Jun, Y.-W.; Yeon, S.-I.; Shin, J.-S.; Cheon, J. *Angew Chem Int Ed Engl* **2006**, Dual-mode nanoparticle probes for high-performance magnetic resonance and fluorescence imaging of neuroblastoma, *45*, 8160-2.

(91) Perez, J. M.; Josephson, L.; O'Loughlin, T.; Hoegemann, D.; Weissleder, R. *Nat. Biotechnol.* **2002**, Magnetic relaxation switches capable of sensing molecular interactions, *20*, 816-820.

(92) Lee, J.; Yang, J.; Ko, H.; Oh, S. J.; Kang, J.; Son, J.-H.; Lee, K.; Lee, S.-W.; Yoon, H.-G.; Suh, J.-S.; Huh, Y.-M.; Haam, S. *Adv. Funct. Mater.* **2008**, Multifunctional magnetic gold nanocomposites: human epithelial cancer detection via magnetic resonance imaging and localized synchronous therapy, *18*, 258-264.

(93) Comes Franchini, M.; Baldi, G.; Bonacchi, D.; Gentili, D.; Giudetti, G.; Lascialfari, A.; Corti, M.; Marmorato, P.; Ponti, J.; Micotti, E.; Guerrini, U.; Sironi, L.; Gelosa, P.; Ravagli, C.; Ricci, A. *Small (Weinheim an der Bergstrasse, Germany)* **2010**, Bovine Serum Albumin-Based Magnetic Nanocarrier for MRI Diagnosis and Hyperthermic Therapy: A Potential Theranostic Approach Against Cancer, *6*, 366-370.

(94) Kaplan, H. S. *Cancer* **1977**, Basic principles in radiation oncology, *39*, 689-93.

(95) Saatchi, K.; Hafeli, U. O. *Bioconjugate Chem.* **2009**, Radiolabeling of Biodegradable Polymeric Microspheres with [99mTc(CO)3]+ and in Vivo Biodistribution Evaluation using MicroSPECT/CT Imaging, *20*, 1209-1217.

(96) de Jong, M.; Breeman, W. A. P.; Kwekkeboom, D. J.; Valkema, R.; Krenning, E. P. *Acc. Chem. Res.* **2009**, Tumor Imaging and Therapy Using Radiolabeled Somatostatin Analogues, *42*, 873-880.

(97) Krenning, E. P.; Kwekkeboom, D. J.; Bakker, W. H.; Breeman, W. A.; Kooij, P. P.; Oei, H. Y.; van Hagen, M.; Postema, P. T.; de Jong, M.; Reubi, J. C.; et al. *European journal of nuclear medicine* **1993**, Somatostatin receptor scintigraphy with [111In-DTPA-D-Phe1]- and [123I-Tyr3]-octreotide: the Rotterdam experience with more than 1000 patients, *20*, 716-31.

(98) Reubi, J. C.; Schar, J.-C.; Waser, B.; Wenger, S.; Heppeler, A.; Schmitt, J. S.; Macke, H. R. *European journal of nuclear medicine* **2000**, Affinity profiles for human somatostatin receptor subtypes SST1-SST5 of somatostatin radiotracers selected for scintigraphic and radiotherapeutic use, *27*, 273-282.

Chapter 2 : Lanthanide Containing Multi-functional Polymers for pDNA Delivery*

*This work is collaborative effort between dissertation author, and Lian Xue (University of Minnesota). Lian performed biological work (transfection and toxicity experiments) for this chapter.

Abstract:

'Theranostic nanomaterials' emerged in last decade combine therapeutic delivery and diagnostic imaging into one package and offer opportunity to minimize the time and therapeutic dosage during treatment. We have developed nucleic acid delivery polymers comprising of oligoethylene amines that are able to be protonated at physiological pH (for binding to DNA) and lanthanide-chelating domain, which can impart diagnostic functionality. Our materials can compact large, polyanionic DNA into nanoparticles that can be monitored both *in vivo* (Gd chelation, MRI imaging,) and *in cellulo* (Tb chelation, fluorescence microscopy).

The materials were synthesized by step-growth polymerization of oligoethylene diamines with a varying number of secondary amines and diethylenetriamine pentaacetic acid (DTPA-BA). Monomers were prepared in high purity via a multistep procedure comprising of selective protection and deprotection of primary and secondary amines based on a procedure previously developed in the Reineke lab. Gadolinium and terbium analogues of series of polymers with varying number of amines (three-to- six) were synthesized with high purity (no free lanthanide present) and degree of polymerization between 18-24. Chelation of polymer backbone with gadolinium and terbium was performed to functionalize polymer structure with MRI contrast agent and luminescent agent properties. All of the polymers had one water coordination site

calculated by the Horrock's equation and possess longitudinal relaxivities (r_1) at least twice (per Gd basis) that of Magnevist®, a clinical contrast agent.

All the polymers formed (zeta potential +25 to 50mV at N/P 40) polyplexes (50-80nm hydrodynamic diameter) with pDNA. In this study, the effect of amine number along the polymer backbone on transfection efficiency and cytotoxicity was investigated. A trend was observed whereas the secondary amine number in the polymer backbone increases from three to six, we observed an increase in the transfection efficiency in Human Glioblastoma Cells (U-87) with an anomaly of polymer with four amines. The change in amine number did not affect the cytotoxicity and all the polyplexes showed high cell survival (~90%) at N/P 40.

1. Introduction:

Recently published[1] statistics on cancer have highlighted that one out of four deaths in United States occur due to cancer. This imposes an urgent need for development of anticancer drugs to avoid falling into the "valley of death" of drug development as Adams[2] points out. Nucleic acid based therapeutics holds promise in treating aggressive and deadly diseases such as cancer, diabetes, Alzheimer's disease or other genetic disorders; however, lack of efficacious delivery of these polynucleotides has presented impediments for the field to advance for clinical approval.[3,4] For a nucleic acid carrier to be effective, it has to be endocytosed, undergo intracellular trafficking, and get released in the nucleus (pDNA) or the cytoplasm (siRNA).[5]

When injected systemically, nanomedicine delivery vehicles are strategically designed to accumulate in tumor/cancer site via 'passive targeting' through 'enhanced permeability and retention (EPR) effect'.[6,7] To monitor this delivery in real-time, nanoparticles can be loaded with

imaging agents such as fluorescent markers, MRI contrast agents, and radionuclides which allow non-invasive imaging.[8]

In last decade, interdisciplinary research in the field of chemistry, biology, nanotechnology, materials science and medicine has led to development of novel materials that are capable of combining therapy and imaging into one modality.[8-10] These 'theranostic' materials can potentially eliminate the need for multi-step drug administration process for diagnosis and treatment and enable real-time monitoring of drug delivery and drug efficacy.[11]

Magnetic resonance imaging is a non-invasive imaging technique, with higher spatio-temporal resolution and anatomical background contrast compared to PET, SPECT, CT and ultrasound with the advantage of having an absence of ionizing radiation.[12-14]

Optical imaging provides unique advantages over any other techniques by offering the capability to image/track NPs in real time and, as Bünzli and Piguet[15] point out light-detecting (or signaling) methods are sensitive modes of detection. However, there is an inherent tissue absorption in of light in living systems, which leads to background fluorescence and decreases accuracy/sensitivity of this technique during *in vivo* imaging. [16] For *in vivo* applications, the near-IR window where light is able to penetrate into the tissue is 650-900 nm and this narrow optical window essentially limits the choice of organic fluorophores. Some of these problems can be overcome by using inorganic nanoparticles which do not photobleach, have small Stokes shifts and can have relatively longer lifetimes.[17]

Luminescent lanthanides such as europium (Eu) or terbium (Tb) are an alternative choices over traditional fluorescent dyes because they do not photobleach, have large Stokes shifts, narrow emission lines and long luminescence lifetimes, this helps to eliminate background autofluorescence by performing experiments in a time-delayed manner and are also useful

donors for fluorescence resonance energy transfer.[18] While there is toxicity affiliated with lanthanides (which is why they need to be chelated) lanthanides are not considered as Class A or B toxic elements unlike cadmium or selenium based semiconductor quantum dots.[16]

To this end, our group has developed novel lanthanide containing theranostic agents for nucleic acid delivery.[19] Current studies are focused on understanding structure-property relationships of a class of polymer vehicles that was originally developed by Bryson et al.[19] In the previous study, gadolinium or europium chelated polymers with three or four number of secondary amines along the backbone were synthesized and studied. Gd analogues of these polymers showed good MRI contrast agent properties in bulk cells and luminescent Eu containing polymers were imaged intracellularly with confocal imaging. In addition, very low cytotoxicity and high cellular uptake associated with these systems was encouraging to pursue further studies. In this current study, we sought to extend this design motif -by with varying the ethyleneamine number along the polymer backbone from three to six and observing the effect of these chemical changes on transfection efficiency and cytotoxicity. The diagnostic functionality of these structures can be varied by switching out the metal functionality (gadolinium or terbium) within the chelate structure of the polymer backbone. This enables millimeter or micrometer imaging resolution in vivo using MRI (with the Gd polymer vehicle analogues) or up to a nanometer resolution with optical or fluorescence imaging techniques (Tb analogues).

2. **Experimental**

2.1. *Materials*

All reagents obtained were purchased from Aldrich Chemical Co. (Milwaukee, WI) and used without any further purification unless specified otherwise. Diethylene triamine pentaacetic

acid was purchased from Alfa Aesar Chemical Co. (Ward Hill, MA). Pentaethylene hexamine obtained from Sigma Aldrich (95% pure) was further purified by double distillation. MeOH and dichloromethane were purified with MBRAUN MB SPS solvent purification system. Dry dimethyl sulfoxide (DMSO) was purchased from Alfa Aesar.

The Liquid Chromatography-Mass Spectra (LC-MS) were obtained on Agilent (Wilmington, DE,USA) HPLC 1100 series equipped with diode array detector, column heater, and Thermo Survey (San Jose, CA, USA) auto-sampler. The columns used for HPLC separations were Agilent extended C18 HPLC columns (50 x 2.1 mm) and the mobile phase was water (1% formic acid), methanol (1% formic acid) or acetonitrile (1% formic acid). For mass spectral analysis, the HPLC column effluent was directly pumped into the spray chamber of a Thermo Instrument TSQ triple quadrupole mass spectrometer (Thermo Finnigan, San Jose, CA, USA) equipped with ESI source. NMR spectra were obtained on Inova 400MHz or AVANCE 500 MHz instrument. Thin Layer Chromatography (TLC) was performed on TLC aluminum sheets (silica gel 60 F_{254}) obtained from Whatman (GE healthcare). The dialysis membranes (1000 and 3500 Da MWCO) were manufactured by Spectrum Laboratories, Inc. (Rancho Dominguez, CA) and dialysis was performed with ultrapure water. T_1 relaxivity measurements were performed on Bruker Minispec (Bruker Optics, Billerica, MA, USA) mq 20 NMR and mq 60 NMR series at magnetic field strengths, 0.47T and 1.41 T respectively. Dynamic light scattering was performed on Zetasizer Nanoseries, Malvern Instruments (Malvern, UK) equipped with 633nm wavelength laser. Luminescence lifetime measurements on 6a-6d Tb polymers were performed on Cary Eclipse fluorescence spectrometer by Agilent Technologies.

The synthesis of monomers 1a, 1b, 3a and 3b and polymers 4a and 4b was performed using procedures previously developed in our lab b Bryson et al. with some modifications[19-21] and is described in brief below.

2.2. Synthesis of monomers

*2.2.1. N^2,N^3,N^4-tris(tert-butoxycarbonyl)-tetraethylenepentamine (**1a**):*

Tetraethylene pentamine hydrochloride (11.7 g, 31.4 mmol) and triethylamine (TEA 17.5 g, 172.9 mmol) were dissolved in 3:1 mixture (~ 250 mL) of dry dichloromethane (DCM) and dry methanol and cooled down to 0°C. To this solution, ethyl trifluoroacetate (9.6 g, 67.5 mmol) was added dropwise to selectively protect the primary amines. The reaction mixture was stirred at 0ºC for 30min and then warmed up to room temperature and stirred overnight. After protection of the terminal amines, the reaction mixture was cooled again to 0°C and secondary amines were reacted with di-*tert* butyl bicarbonate (Boc) (22.0 g, 100.9 mmol) dissolved in DCM. The reaction mixture was stirred for 24 h at room temperature. After reaction was complete (monitored via TLC), the solvent was evaporated using a rotary evaporator and redissolved in DCM. Next, the product was extracted with sat. $NaHCO_3$ and brine to remove TEA-salt. The organic layers were collected, dried over Na_2SO_4 and reduced down to a crude product *in vacuo*. The crude product obtained after extraction was precipitated in ethyl acetate and recrystallized using ethanol to yield pure white solid.

Deprotection of the primary amines was performed by dissolving the above mentioned product (10.0 g, 14.7 mmol) and refluxing the mixture in (80°C) methanol (100 mL) in the presence of K_2CO_3 (9.1 g, 65.8 mmol) dissolved in H_2O (~15 mL). Deprotection was carried out for 6h. Next, the solvent was evaporated to dryness *in vacuo* and product was redissolved in chloroform. Chloroform mixture was filtered through a bed of Celite™, dried over Na_2SO_4 and

reduced down to obtain a crude product as yellowish oil. The crude product was purified using automated flash chromatography using DCM: Ethanol: NH_4OH (80:20:0.1) as eluant system. The product obtained was a clear viscous oil.

Yield: 3.1 g (43.0%)

^{1}H-NMR ($CDCl_3$): δ (ppm) = 1.46 (s, 27H), 2.83 (s, 4H), 3.33 (bm, 12H).

LC-ESI-MS positive mode- Calculated [C_{23} H_{47} N_5 O_6] m/z = 489.35 (M) Found: m/z = 490.30 ($M+H^+$)

*2.2.2. N^2,N^3,N^4,N^5-tetra(tert-butoxycarbonyl)-pentaethylenehexamine (**1b**):*

Pentaethylene hexamine (10.8 g, 46.7 mmol) was dissolved in anhydrous DCM (~150mL) and cooled down to 0ºC. To this solution, ethyl trifluoroacetate (14.1 g, 99.2 mmol) was added dropwise to protect the primary amines selectively. The reaction mixture was stirred at 0°C for 30min and then warmed up to room temperature and stirred overnight. After protection of the terminal amines, the reaction mixture was cooled down again to 0°C and the secondary amines were protected by addition of di-*tert* butyl bicarbonate (43.8 g, 200.7 mmol) and dissolved in DCM. The reaction mixture was stirred for 24 h at room temperature. After the reaction was complete (monitored via TLC), the solvent was evaporated using a rotary evaporator and orange oil formed was precipitated using ethyl acetate and recrystallized with ethanol to yield a pure white solid.

The primary amines within the structures of fully protected oligoamines were deprotected by dissolving the solid product (6.3g, 7.6 mmol) in refluxing methanol (~120 mL) in the presence of K_2CO_3 (6.3 g, 45.6 mmol) dissolved in H_2O (~15 mL). The deprotection was carried out for 6 h. Next, the solvent was evaporated to dryness *in vacuo* and the product was redissolved in chloroform. The mixture was filtered through a bed of Celite™ and reduced down

to obtain a crude product. The crude product was purified *via* recrystallization from 9:1 mixture of methyl *tert*-butyl ether (MTBE) and ethanol to yield a pure white amorphous solid. M.P. 112-113°C .

Yield: 3.2 g (66.7%)

^{1}H-NMR ($CDCl_3$): δ (ppm) = 1.48 (s, 36H), 2.81 (s, 4H), 3.32 (bm, 16H). (Appendix A)

^{13}C-NMR ($CDCl_3$): δ (ppm) = 28.78, 40.95, 45.62, 79.86 and 155.90. (Appendix B)

LC-ESI-MS positive mode- Calculated [C_{30} H_{60} N_6 O_8] m/z = 632.45 (M) Found: m/z = 633.45 ($M+H^+$) (Appendix C)

*2.2.3. N^1,N^5-bis(2-ethylphthalimido)-N^1,N^2,N^3,N^4,N^5-penta(tert-butoxycarbonyl)-tetraethylenepentamine (**2a**):*

A solution of phthalimidoacetaldehyde (3.82 g, 20.1 mmol) in anhydrous DCM (25 ml) was added slowly *via* syringe to *N^2,N^3,N^4-tri(tert-butoxycarbonyl)-tetraethylenepentamine* (**1a**) (3.94 g, 8.1 mmol) dissolved in anhydrous DCM (~75 ml), at 0°C (ice bath) under an $N_{2\ (g)}$ purge. The resulting solution was yellowish in color and was stirred for an additional 30 min. Sodium triacetoxyborohydride (4.03 g, 18.9 mmol) was added to the reaction mixture and the resulting heterogeneous mixture was stirred for 1 h at 0°C, and then at room temperature overnight. After completion of the reaction (monitored via TLC), the mixture was first washed with a sat. $NaHCO_3$ solution (2 × 100 ml) to neutralize the residual sodium triacetoxyborohydride, and then with brine (2 × 100 ml). The organic layer was isolated, dried over Na_2SO_4 and reduced to a crude oil on a rotary evaporator. The crude product was redissolved in DCM and the secondary amines were reacted with di-*tert* butyl bicarbonate (4.10 g, 18.78 mmol). The reaction was stirred for 18 h at room temperature, reduced down to a crude product on a rotary evaporator and purified using automated flash chromatography with ethyl

acetate : hexane (1:1) as the eluant. Product fractions were collected from the TLC monitoring the separation and concentrated to yield a pure white solid.

Yield: 3.0g (36.7%)

^{1}H-NMR ($CDCl_3$): δ (ppm) = 1.23 (t, J = 1.22 Hz, 18H), 1.43 (s, 27H), 3.29 (bm, 16H), 3.50 (bm, 4H), 3.81 (bm, 4H), and 7.72-7.83 (bm, 8H).

LC-ESI-MS positive mode- Calculated [C_{53} H_{77} N_7 O_{14}] m/z = 1035.55 (M) Found: m/z = 1036.56 ($M+H^+$)

*2.2.4. N^2,N^3,N^4,N^5,N^6-penta(tert-butoxycarbonyl)-hexaethyleneheptamine (**3a**):*

Hydrazine monohydrate (1.74 g, 34.8 mmol) was added to the solution of **2a** (1.65 g, 1.59 mmol) in methanol (25 ml) and was refluxed for 6 h. After completion of the reaction, the mixture was cooled down and a white precipitate from the side product- 2,3-dihydro-1,4-phthalazinedione was filtered off. The reaction mixture was concentrated under reduced pressure to yield a white amorphous solid. The solid obtained was then redissolved in DCM (~30 ml), and washed with 4 M NH_4OH solution (2 × 20 ml) and then with water (2 × 20 ml). All the organic layers were collected, dried on Na_2SO_4, and concentrated under reduced pressure to yield a white solid. The resulting solid was purified by recrystallization from methyl tert-butyl ether.

Yield: 0.7g (53.8%)

^{1}H-NMR ($CDCl_3$): δ (ppm) = 1.44 (s, 45H), 2.81 (bm, 4H), 3.31 (bm, 20H) (Appendix A)

^{13}C-NMR ($CDCl_3$): δ (ppm) = 28.57, 41.04, 46.00, 79.88 and 155.82 (Appendix B)

LC-ESI-MS positive mode- Calculated [C_{37} H_{73} N_7 O_{10}] m/z = 775.54(M) Found: m/z = 776.55 ($M+H^+$) (Appendix C)

*2.2.5. N^1,N^6-bis(2-ethylphthalimido)-N^1,N^2,N^3,N^4,N^5,N^6-hexa(tert-butoxycarbonyl)-pentaethylenehexamine (**2b**):*

2b was synthesized using a similar procedure to that of **2a**, except, instead of **1a**, **1b** (4.5 g, 7.2 mmol) was added to the reaction mixture and other reagents were added in similar molar ratios.

Yield: 2.8 g (33%)

^{1}H-NMR ($CDCl_3$): δ (ppm) = 1.23 (t, J = 1.22 Hz, 18H), 1.42 (s, 36H), 3.30 (bm, 20H), 3.50 (bm, 4H), 3.80 (bm, 4H), 7.71-7.82 (bm, 8H).

LC-ESI-MS positive mode, calculated [$C_{60}H_{90}N_8O_{16}$] m/z = 1178.65 (M), Found m/z= 1179.71 ($M+H^+$)

*2.2.6. N^2,N^3,N^4,N^5,N^6,N^7-hexa(tert-butoxycarbonyl)-heptaethyleneoctamine (**3b**):*

3b was synthesized using procedure described for **3a**, where, **2b** (1.7 g, 1.4 mmol) was used in place of **2a** and other reagents were used in similar molar ratios.

Yield: 0.50 g (38%) M.P. 142-143 °C.

^{1}H-NMR ($CDCl_3$): δ (ppm) = 1.45 (s, 54H), 2.83 (t, 4H), 3.31 (bm, 24H) (Appendix A)

^{13}C-NMR ($CDCl_3$): δ (ppm) = 28.86, 40.85, 45.43, 79.90 and 155.49 (Appendix B)

ESI-MS positive mode, Calculated [$C_{44}H_{86}N_8O_{12}$] m/z = 918.64 (M), Found m/z = 919.49 ($M+H^+$) (Appendix C)

*2.2.7. 2-(bis(2-(2,6-dioxomorpholino)ethyl)amino)acetic acid (**4a**):*

The synthesis of diethylenetriamine pentaacetic acid bis-anhydride (DTPA-BA, 4a) monomer from diethylenetriamine pentaacetic acid (DTPA) was performed using a reported procedure.[22] A slurry of 1.60 g (4.1 mmol) of DTPA, dry pyridine (2 mL) and acetic anhydride (2.24 g, 21.9 mmol) was prepared. The reaction mixture was stirred at 65°C for 24 h. After 24 h, the reaction mixture was filtered and a solid product was washed with acetic anhydride and then with diethyl ether to yield an off-white solid product. The resultant product when analyzed with

NMR. The NMR integration indicated formation of anhydride ring close to ~100% and did not require any further purification.

Yield: 1.32g (91%). M.P. 180-182 °C.

^{1}H-NMR (d^{6}-DMSO): δ (ppm) = 2.57 (t, J = 2.59 Hz, 4H), 2.72 (t, J = 2.75 Hz, 4H), 3.28 (s, 2H), 3.69 (s, 8H). (Appendix A)

^{13}C-NMR (d^{6}-DMSO): δ (ppm) = 50.70, 51.73, 52.61, 54.44, 54.99, 165.84, 170.73, 171.95, 172.50. (Appendix B)

2.3. Polymer Synthesis

*2.3.1. Poly ([N^{2}, N^{3}, N^{4}–tris(tert -butoxycarbonyl) tetraethylenepentamine] amidodiethylenetriaminetriaacetic acid) (**5a**):*

Monomer **1a** (1.074 g, 2.2 mmol) was added to a 25 mL dry flask containing 7.0 mL of dry dimethyl sulfoxide (DMSO) and dissolved at 80°C and cooled down to room temperature after dissolution. Monomer **4a** (0.78 g, 2.2 mmol) dissolved in 3.5 mL of dry DMSO was added *via* canula to the solution of **1a** and polymerization was carried out at room temperature for 18 hours. After the polymerization, the reaction mixture was deposited into a dialysis bag (MWCO 1000 Da) and dialyzed against methanol for 24 h to remove unreacted monomers and low molecular weight oligomers. The dialysis with MeOH allows solvent exchange from DMSO to low boiling MeOH, which is, then evaporated using a rotary evaporator. The product obtained was dried under vacuum overnight to yield a yellowish-white solid polymer.

Yield: 1.25 g (69%)

^{1}H NMR (d^{6}-DMSO): δ (ppm) = 1.39 (s, 27H), 2.83 (bm, 4H), 2.94 (bm, 4H), 3.25 (bm, 16H), 3.27 (s, 6H), 3.40-3.50 (bm, 4H), 8.0 (s, 1H) (Appendix A)

*2.3.2. Poly ([N^2, N^3, N^4, N^5–tetra(tert -butoxycarbonyl) pentaethylenehexamine] amidodiethylenetriaminetriaacetic acid) (**5b**):*

5b polymer was synthesized using the procedure described for the **5a**, where, **1b** (0.46 g, 0.72 mmol) was used instead of **1a** and the rest of the reagents were added in similar molar proportions. The final polymer was obtained in the form of a yellowish-white solid.

Yield: 0.45 g (63.9%)

^{1}H NMR (d^6-DMSO): δ (ppm) = 1.37 (s, 36H), 2.43 (bm, 4H), 2.96 (bm, 4H), 3.23 (bm, 20H), 3.36 (s, 6H), 3.41-4.50 (bm, 4H), 8.09 (bm, 1H). (Appendix A)

*2.3.3. Poly ([N^2, N^3, N^4, N^5, N^6 –penta (tert -butoxycarbonyl) hexaethylneheptamine] amidodiethylenetriaminetriaacetic acid) (**5c**):*

5b polymer was synthesized using the procedure described for the **5a**, where, **3a** (0.18 g, 0.23 mmol) was used instead of **1a** and rest of the reagents were added in similar molar proportions. The polymer was obtained in the form of a yellowish-white solid.

Yield: 0.18 g (68%)

^{1}H NMR (d^6-DMSO): δ (ppm) = 1.36 (s, 45H), 2.82 (bm, 4H), 2.92 (bm, 4H), 3.20 (bm, 24H), 3.35 (s, 6H), 3.41 (s, 4H), 8.07 (bm, 1H). (Appendix A)

*2.3.4. Poly ([N^2, N^3, N^4, N^5, N^6, N^7-hexa (tert -butoxycarbonyl) heptaethyleneoctamine] amidodiethylenetriaminetriaacetic acid) (**5d**):*

5d polymer was synthesized using the procedure described for the **5a**, where, **3b** (0.34 g, 0.37 mmol) was used instead of **1a** and rest of the reagents were added in similar molar proportions. The polymer was obtained in the form of a yellowish-white solid.

Yield: 0.34 g (72%)

^{1}H NMR (d^6-DMSO): δ (ppm) = 1.36 (s, 54H), 2.79 (bm, 4H), 2.90 (bm, 4H), 3.19 (bm, 28H),

3.31 (s, 6H), 3.37 (s, 4H), 8.09 (bm, 1H). (Appendix A)

2.3.3. General procedure for deprotection of Boc groups:

The deprotection of the Boc groups on the polymer backbone was performed using a standard trifluoroacetate (TFA) deprotection method.[23] 0.4 mmol of polymer (**5a-5d**) was dissolved 4.0 mL of DCM and cooled to 0°C. To this solution, 4.0 mL of TFA was added and the reaction mixture was warmed up to the room temperature. The reaction mixture was stirred for overnight at room temperature to allow deprotection of all the Boc groups and confirmed with NMR for completion of reaction. The solvents were evaporated *in vacuo* using a rotary evaporator and the resultant polymer was redissolved in ultrapure water and neutralized using saturated $NaHCO_3$. Next, the polymer solution was deposited into a dialysis bag (MWCO 3500 Da) and dialyzed against ultrapure water for 24 h. After dialysis, the solution was lyophilized to yield a white, fluffy, solid polymer.

*Characterization of **6a***

Yield: 0.41g (52%)

^{1}H NMR (D_2O): δ (ppm) = 3.02 (t, 4H), 3.12 (t, 4H), 3.20-3.30 (bm, 12H), 3.36 (t, 4H), 3.43 (s, 4H), 3.61 (bm, 4H), 3.86 (s, 2H)

*Characterization of **6b***

Yield: 0.21g (89%)

^{1}H NMR (D_2O): δ (ppm) = 3.02-3.10 (bm, 20H), 3.23 (s, 6H), 3.32 (t, 4H), 3.40 (s, 4H), 3.51 (t, 4H), 3.84 (s, 2H)

*Characterization of **6c***

Yield: 81 mg (83%)

^{1}H NMR (D_2O): δ (ppm) = 2.98-3.04 (bm, 24H), 3.20 (s, 4H), 3.26 (t, 4H), 3.37 (bm, 6H), 3.46 (bm, 4H), 3.77 (s, 2H)

*Characterization of **6d***

Yield: 0.106 mg (60%)

^{1}H NMR (D_2O): δ (ppm) = 2.89-3.10 (bm, 28H), 3.21 (s, 4H), 3.29 (t, 4H), 3.38 (bm, 6H), 3.55 (bm, 4H), 3.80 (s, 2H).

2.3.4. General Procedure for chelation of polymers with Gd or Tb:

Chelation of the polymers were carried out in 1:1 molar ratio between the lanthanide (Ln = Gd or Tb) and each polymer. Each polymer (0.082 mmol **6a-6d**) was dissolved in 1.7 mL of ultrapure water. Next, 0.082 mmol of $LnCl_3$ ($GdCl_3$ or $TbCl_3$) was dissolved in 0.8 mL of water and was then added to the polymer solution in three separate aliquots. The pH was adjusted to 6-7 using saturated $NaHCO_3$ after each aliquot addition. The reaction mixture was stirred at room temperature for 3 h. Next, the solution was deposited into a dialysis bag (MWCO 3500 Da) and dialyzed against ultrapure water for 24 h to remove the excess of $LnCl_3$. After dialysis, the solution was lyophilized to yield white, fluffy, chelated polymer.

Yields: **6aGd**-87mg (70%), **6aTb-**137.5mg (67%), **6bGd**- 19.4mg (73%), **6bTb**- 25.0mg (75%) **6cGd**- 37.1mg (72%), **6cTb**- 26.0 mg (62%), **6dGd**- 52.0 mg (77%) and **6dTb**- 43.7 mg (74%)

Synthetic Scheme:

Synthesis of the oligoethylene diamine monomers

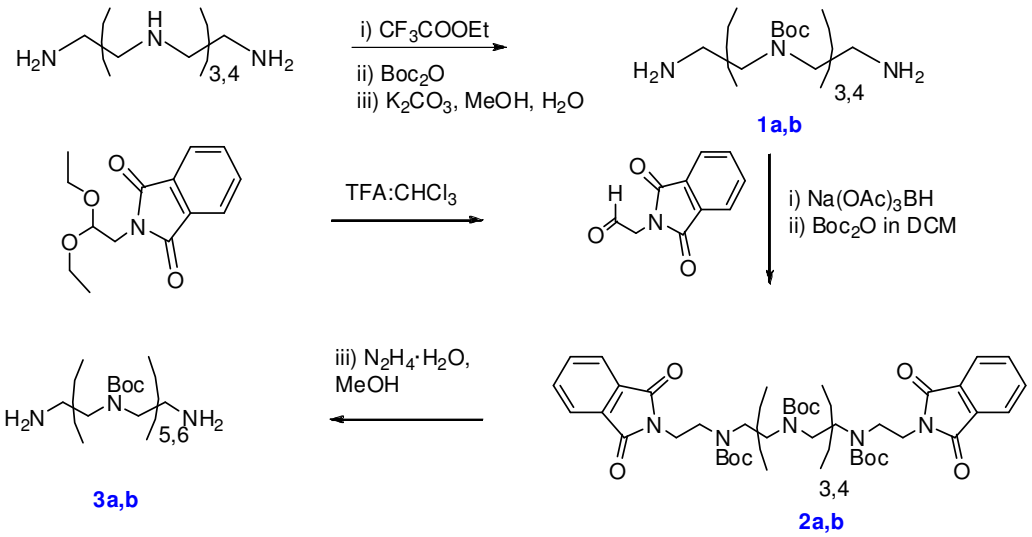

Synthesis of DTPA-BA monomer

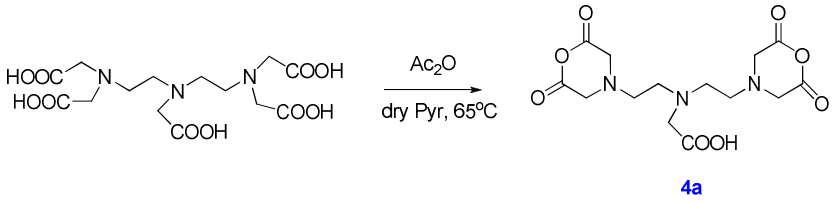

Polymerization:

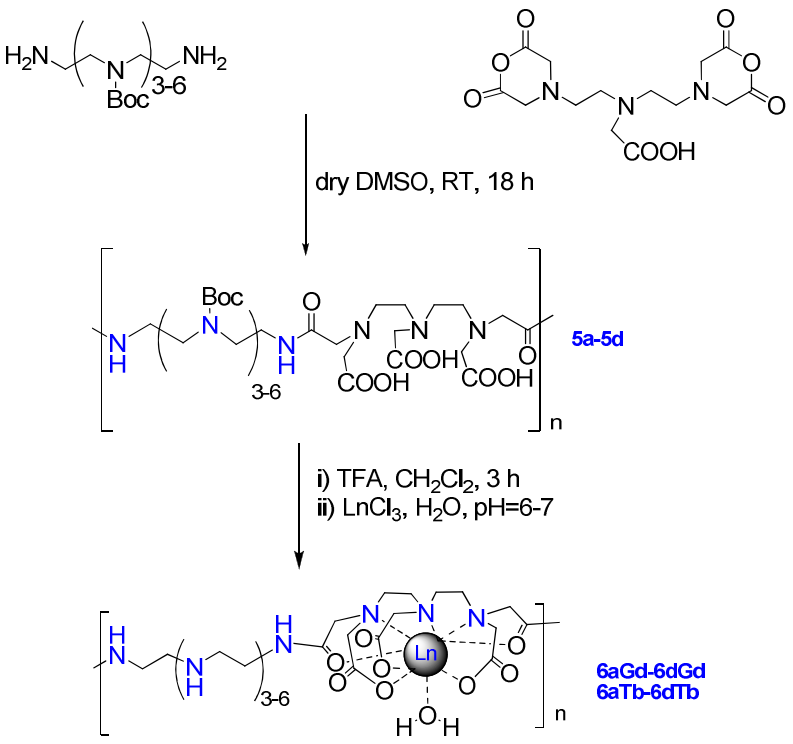

2.4. *Polymer and Polyplex Characterization*

2.4.1. *Size Exclusion Chromatography (SEC):*

Polymers **6a-6d** (**Gd** and **Tb**) were characterized using SEC to determine the weight average molecular weights and polydispersity indices. SEC was performed in an aqueous mobile phase- 0.45 M sodium acetate in water with 20v% Acetonitrile, pH 7 (adjusted using acetic acid), flow rate 0.6 mL/min. Polymer dissolved in the mobile phase was separated using $GMPW_{xL}$ and $G2500PW_{xL}$ (Tosoh Bioscience) columns. This system was equipped with- a Waters 2489 UV/vis detector (l ¼ 274 nm), a Wyatt Optilab rex refractometer (l ¼ 658 nm), and a Wyatt DAWN Heleos-II multiangle laser light scattering (MALLS) detector (l ¼ 662 nm). The data was recorded and analyzed using the ASTRA (version 5.3) software.

2.4.2. Gel Electrophoresis Shift Assay:

The pDNA binding ability of a polymer was studied using a gel electrophoresis shift assay. Agarose gel (0.6 w/v %) containing ethidium bromide (0.06 w/v %) was prepared in a Tris-acetate EDTA (TAE) buffer (40 mM Tris-acetate, 1 mM EDTA, pH 8). Polyplexes were formulated at N/P ratios (this ratio denotes: N= number of amines from the polymer backbone and p= number of phosphate units from DNA used to formulate the polyplexes) - 0, 2.5, 5, 10, 20, 30, 40 and 50 by mixing equal volumes (10 µL each) of polymer and pDNA (0.1 µg/µL, pcmv lacZ). Polymer solutions were prepared using nuclease-free water (Gibco, Invitrogen, Carlsbad, CA). After formulation, the polyplexes were incubated at room temperature for 30 min before addition of 2µL of gel loading buffer (Blue juice, Invitrogen, Carlsbad, CA). Next, 10µL of each N/P formulation was loaded into each well and an electrophoretic field (65 V, 60 min) was applied to study the inhibition of DNA migration toward anode in presence of polymer. The gel was visualized using UV light and a digital camera.

2.4.3. Dynamic Light Scattering:

Hydrodynamic diameter and zeta potentials of the polymer-pDNA complexes (polyplexes) were determined using a dynamic light scattering technique. First, the polyplexes were formulated at N/Ps- 5,10,20, and 40 in nuclease-free water by mixing equal volumes of pDNA (pcmv lacZ, 6-8000 bp, 0.02 mg/mL) and polymer. Polyplexes were incubated at room temperature for 30 min. Next, the polyplexes were diluted with 600 µL of water before size and zeta potential measurements. All the measurements were performed in triplicate and standard error bars represent standard deviation of the three measurements.

2.4.4. Determination of effect on longitudinal relaxation rate (R_1) of water:

The effect on T_1 relaxation times of water in the presence of **6a-6d Gd** polymers and polyplexes was studied with a Bruker Minispec (20 mq, 0.45 T and 60 mq, 1.41 T series) using an inversion recovery pulse sequence (180^0- d_t- 90^0- acquire). Solutions of **6a-6d** for the **Gd** polymers and Magnevist ® (a clinical contrast reagent) were prepared (1.0 mM) in ultrapure water (based on repeat unit molecular weight and on per 'Gd' basis). For the polyplex samples, equal volumes of polymer and pDNA were mixed in order to achieve 1mM concentration on per Gd basis. All the measurements were performed in triplicate and error bars represent the standard deviation of the three measurements.

2.4.5. Determination of number of water coordination sites (q) for Tb polymers:

Determination of number of water coordination sites (q) per chelate was performed by measuring the luminescence lifetimes of the **6a-6d Tb** polymers (**N3-N6Tb**) in D_2O and H_2O using a Cary Eclipse fluorescence spectrometer (Agilent Technologies, USA; formerly Varian). The data was processed with Agilent Cary WinFLR software.

Each sample (polymers **6a-6d Tb**) was prepared at 0.5mM concentration (800µL) using D_2O and H_2O as a solvent and deposited into a small-volume quartz cuvette. Lifetime measurements were performed with the excitation wavelength of 350 nm (slit 5nm),emission wavelength of 550 nm (slit 10 nm), a delay time of 0.1ms, a gate time of 0.3 ms and a total decay time of 15 ms. All the measurements were performed in triplicate and each error bar represents a standard deviation of three measurements. The revised Horrocks[24,25] equation (eq. 1) was used to calculate the number of water coordination sites (q) per chelate unit. The number of water coordination sites was found to be ~1 for all the polymers.

$$q_{Tb} = 5\left[\left(\frac{1}{\tau_{H2O}} - \frac{1}{\tau_{D2O}}\right) - 0.06x\right] \quad (1)$$

x = number of N-H oscillator where oxygen on carbonyl of amide groups is coordinated to the Tb^{3+}.

*2.5. Cell Culture Studies**

**the experimental part for cell culture studies was written by Lian Xue*

2.5.1. General procedure for pDNA transfection of human glioblastoma (U87) cells:

Prior to transfection, U87 cells were seeded at 5×10^4 cells/well in 24-wellplates, and were incubated for 24 h to yield a confluency of above 80%. Polyplexes (N/P 40) were formulated by mixing equal volumes (150 µL) of each polymer solution (**6a-6d Gd** and **Tb**) with pDNA containing the Luciferase reporter gene (gWiz-Luc, 0.02 mg/mL) and incubated at room temperature for 1h. Jet-PEI polyplexes (positive control) were formulated at N/P 5 following the manufacturer's protocol. Along with the above mentioned samples, untransfected cells and cells transfected with pDNA only were used as negative controls. Next, each polyplex solution (**6a-6d** polymers, pDNA and Jet-PEI) was diluted to 900 µL with serum-free media (Opti-MEM, pH 7.2) and each well of cells was transfected with 300 µL of this polyplex solution containing 1 mg of gWiz-Luc pDNA.

Four hours after transfection, 800 µL of the supplemented DMEM was added to each well. Twenty-four hours after transfection, the media was replaced with fresh supplemented DMEM (1 mL). 48 hours after initial transfection, the media was removed and the cells were washed with 500 µL of PBS and treated with cell culture lysis buffer (Promega, Madison, WI). The amount of protein in the cell lysates (as mg of protein) was determined against a standard curve of bovine serum albumin (98%, Sigma, St. Louis, MO), using a Bio-Rad DC protein assay kit (Hercules,

CA). Cell lysates were analyzed for Luciferase activity with Promega's Luciferase assay reagent (Madison, WI). For each sample, luminescence was measured over 10 s in duplicate with a luminometer (GENios Pro, TECAN US, Research Triangle Park, NC), and the average was utilized. The gene delivery efficiency of each sample was characterized by firefly luciferase expression in U87 cells and denoted as relative light units (RLU)/mg protein. The cell viability profiles were characterized by the amount of protein in the cell lysates. The protein level of untransfected cells was used to normalize the data obtained for the protein levels of the cells transfected with naked pDNA and polyplexes formed with different polymers (**6a-6d** and Jet-PEI).

2.5.1. MTT assay to study cellular toxicity:

MTT reagent (3-(4, 5-dimethylthiazol-2-yl)-2, 5-diphenyltetrazolium bromide) was used to estimate the cytotoxicity of the formulations. MTT can be reduced to purple formazan in living cells under the catalysis of mitochondrial reductase. For this assay, U-87 Glioblastoma cells were seeded at 50,000 cells/well in 24-well plates 24 h prior to transfection. pDNA transfection was carried out as mentioned above and 1 mL of DMEM was added to each well 4h after tranfection. 24 h post-transfection, the media was aspirated and the cells were washed with PBS (500 µL/well). 1 mL of serum-containing DMEM with 0.5 mg/mL of MTT was added to each well and cells were incubated for another hour. The media was then replaced with 600 µL of DMSO for 15 min at room temperature. A 200 µL aliquot of the media was transferred to a well of a 96-well plate for analysis by colorimeter with wavelength at 570 nm. Samples of non-transfected cells were used for normalization.

3. Results and Discussion

3.1. Synthesis of monomers and polymers:

The synthesis of the monomers with highest purity was important before moving on to the step growth polymerization. Purity of diamine monomers was determined using LC-MS analysis and that of DTPA-BA monomer was determined using NMR integration. A series of polymers with different amine number (three to six, **6a-6d**) was synthesized via step growth polymerization of oligoethylene diamine monomers with DTPA-BA. Monomers were reacted in stoichiometric ratios to achieve highest degree polymerization. All the polymerizations were performed in dry DMSO (to prevent hydrolysis of the anhydride ring) for 18 h at room temperature to obtain polymers with similar DPs 18-26. The completion of every step during polymerization was monitored via NMR. For example, after first step of polymerization, N-H protons from newly formed amide bond can be observed around 8.5 ppm. Deprotection of Boc groups from the secondary amines along the polymer backbone can be confirmed by absence of tert-butyl resonances around 1.4 ppm. After each step, polymers were purified from the low molecular weight oligomers and unreacted monomers via dialysis.

3.2. SEC Characterization:

SEC analysis was performed on the polymer analogues (**6a-6d**, Gd and Tb) for all of the polymers to determine the absolute weight average molecular weight (Mw). The Mw was found to range from 14.3 to 18.9 kDa and the degree of polymerization was 18-26. The polydispersity index (ratio of Mw/Mn) was between 1.1-1.3. The significantly low PDI (uncharacteristic of step growth polymerization) can be attributed to several dialysis steps performed before achieving the final polymer structures.

(a)

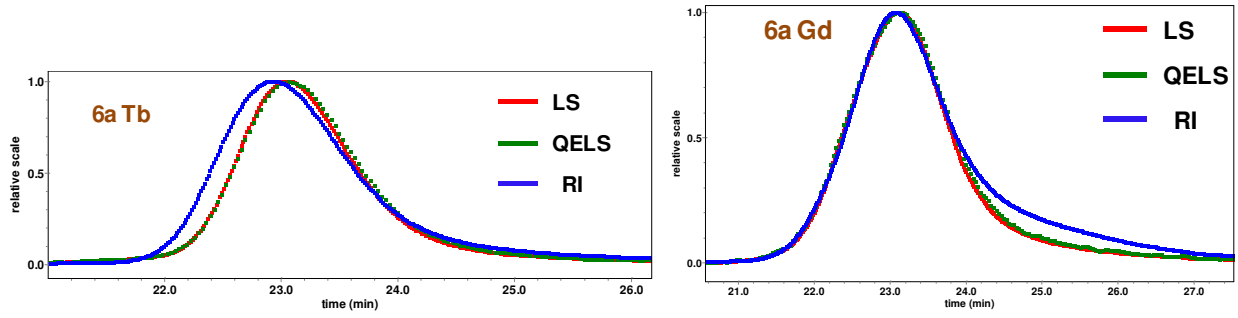
6a Tb
LS
QELS
RI
relative scale
time (min)
6a Gd
LS
QELS
RI
relative scale
time (min)

(b)

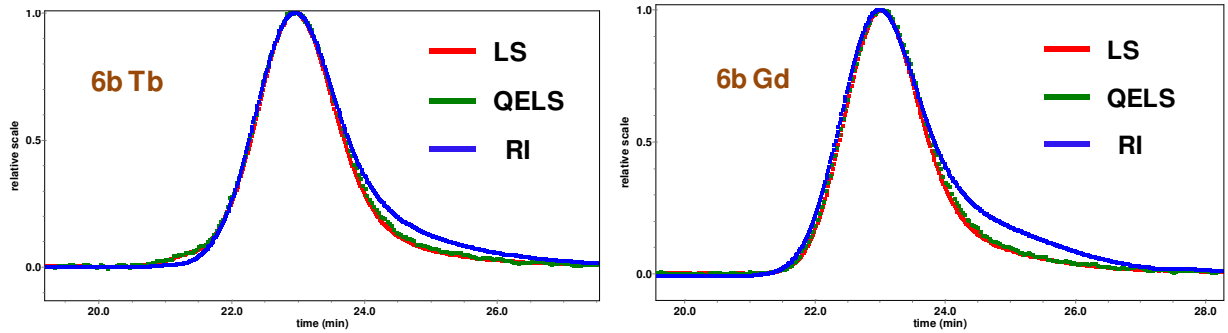
6b Tb
LS
QELS
RI
relative scale
time (min)
6b Gd
LS
QELS
RI
relative scale
time (min)

(c)

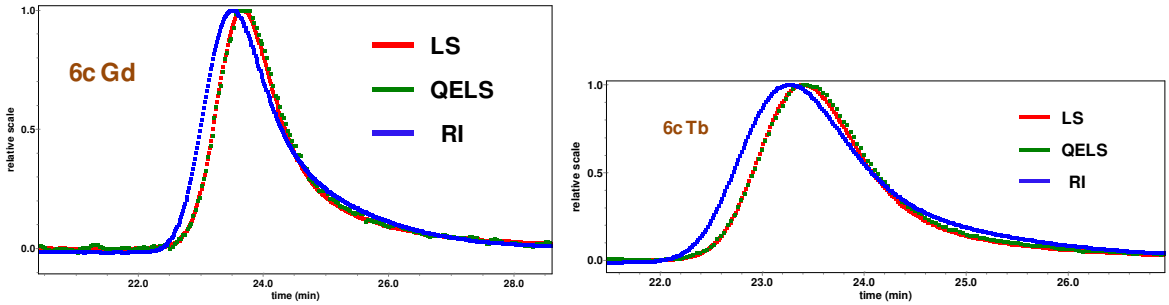
6c Gd
LS
QELS
RI
relative scale
time (min)
6c Tb
LS
QELS
RI
relative scale
time (min)

(d)

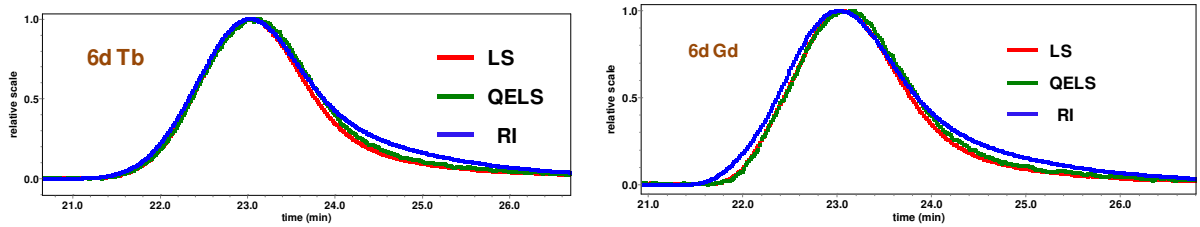
6d Tb
LS
QELS
RI
relative scale
time (min)
6d Gd
LS
QELS
RI
relative scale
time (min)

Figure 2-1: Overlay of light scattering (red), quasi-elastic light scattering (QELS) (green) and refractive index (blue) traces for lanthanide polymers (6a-6d) during size exclusion chromatographic separation.

Table 2-1: SEC characterization of **6a-6d** (Gd and Tb) polymers

Polymer	Mw (kDa)	Mw/Mn	DP
6a Gd	17.6	1.3	25
6a Tb	18.9	1.3	26
6b Gd	16.0	1.2	22
6b Tb	18.3	1.2	24
6c Gd	14.2	1.2	18
6c Tb	14.2	1.2	18
6d Gd	15.0	1.1	19
6d Tb	15.1	1.2	18

3.3. Gel Electrophoresis Shift Assay:

A gel electrophoresis assay was performed to determine a suitable ratio for formulation of pDNA and each of the polymers for polyplex formulation. Because previous results have shown that the N/P ratios of binding can be rather high for this polymer series (and highly dependent on ethyleneamine number).[19] The N/P ratio was found to decrease from N/P 40-50 to N/P 5-10 with the increase in amine number from 3-4 to 5-6 along the polymer backbone. It was also observed that the polymers with the higher amine numbers (5 and 6) were able to completely inhibit DNA migration at N/P 5 compared to analogues with 3 and 4 amines (which bound at N/P 30 or higher), indicated by absence of secondary band.

(a) (b)

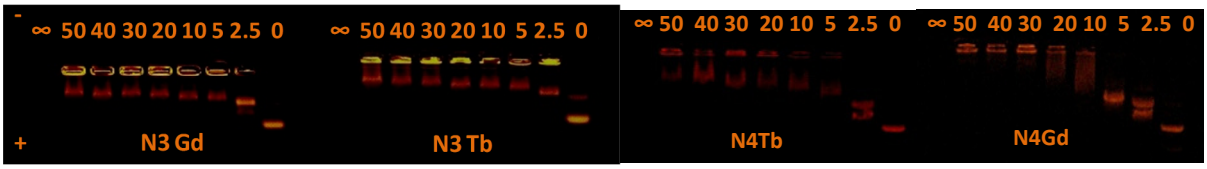

(c) (d)

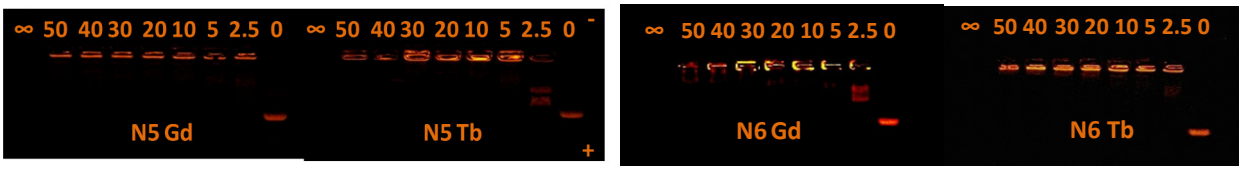

Figure 2-2: Gel electrophoresis assay was performed on 6a-6d (Gd and Tb) polymers to study the relative pDNA binding efficiencies. The binding ratio can be determined by absence of migration of DNA band toward positive electrode. The formulation ratios were varied from 0 to ∞ where 0 and ∞ indicate DNA and polymer only controls respectively. The binding ratio decreases from N/P 40 to N/P 5 with increase in amine number from three to six along the polymer backbone.

3.4. Particle Size and Zeta Potential Determination:

DLS was performed to determine the polyplex size and colloidal stability of the polyplexes in water and to compare of this may (or may not) differ between the structures. The hydrodynamic diameter of these polyplexes was found to be between 80-125 nm at an N/P of 5; however, at N/Ps of 10 to 40, the diameter decreased to 50-80 nm. The decrease in polyplex diameter was noticed with an increase in N/P ratio and can likely be attributed to an increase in pDNA compaction at higher N/Ps.

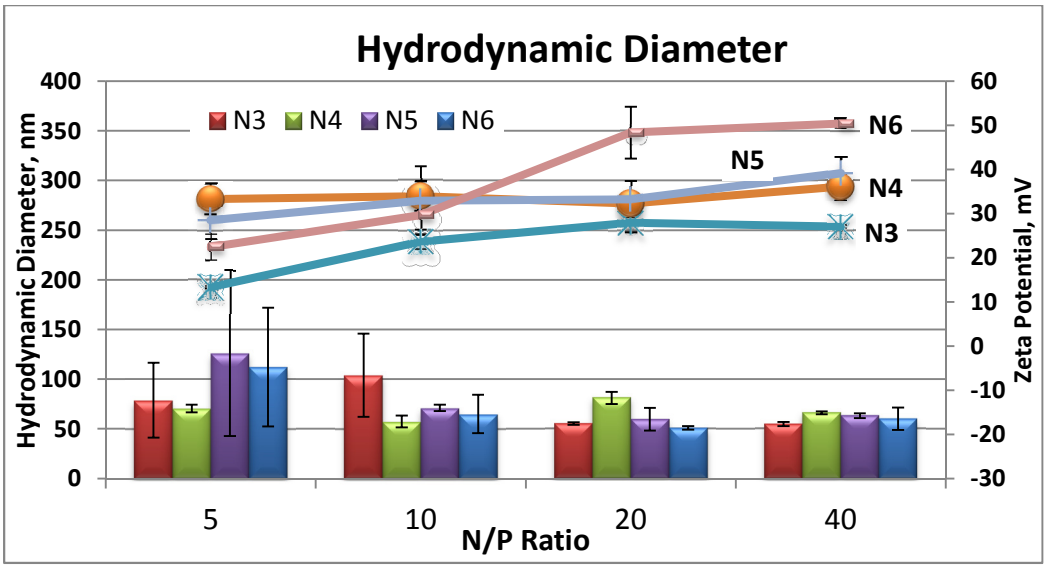

Figure 2-3: Hydrodynamic diameter was determined using dynamic light scattering for **6a-6d** Gd polyplexes formulated with pDNA at the N/P ratios indicated. The hydrodynamic diameters of the polyplexes formulated at different N/P ratios is plotted on the primary axis. Each bar 6a (red), 6b (green), 6c (purple), and 6d (blue) represents average of three hydrodynamic diameter measurements. The secondary axis represents the zeta potential values for **6a-6d** polyplexes. Each point on the line 6a (asterisks), 6b (orange spheres), 6c (blue solid line) and 6d (pink rectangles) represents average of three measurements with standard deviation indicated by an error bar.

3.5. Effect on T_1 relaxation times of water:

The effect on T1 relaxation times of water that both the polymers and the polyplexes induced was measured at two magnetic fields: 0.47 T and 1.41 T using a Minispec instrument. The relaxation rates (R_1) of water in the presence of **6a-6d Gd** polymers and the polyplexes were determined to be between 7.7-9.3 s^{-1} and no specific trend was observed corresponding to the number of amines along the polymer backbone. However, these relaxivities were at least 2X higher than Magnevist™, a clinical contrast agent at same concentration and compared on per

'Gd' basis. The increase in R_1 can be attributed to the increase in molecular weight, size and rotational correlation time of polymers compared to that of Magnevist, which is a small molecule contrast agent. The significant increase in relaxivity of polymer/polyplexes compared to that of Magnevist (on per Gd basis) can be translated into less amount of contrast agent being used to achieve the same image contrast.

(a) (b)

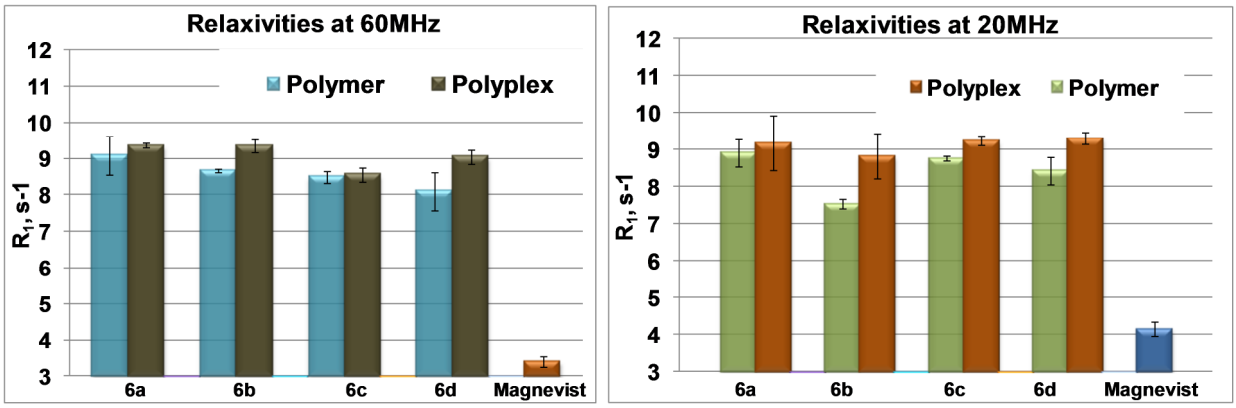

Figure 2-4: Effect on water relaxation rates (R_1) in presence of **6a-6d** Gd polymers and polyplexes at N/P of 40 was measured at 60MHz (a) and 20 MHz (b) and compared to Magnevist™. Each sample was prepared at 1mM Gd concentration and each bar repersents an average of three measurements. All the polymers and polyplexes showed at least 2X increase in relaxivity compared to Magnevist™.

3.6. Determination of number of water coordination sites (q) per repeat unit:

Luminescence lifetime measurements of polymers **6a-6d Tb** in D_2O and H_2O were performed to calculate the number of water molecules ('q') present in the first coordination sphere of the Tb-chelate. The rate of luminescence decay (k) was higher in H_2O compared to

D_2O due to quenching of luminescence through O-H bond vibrational overtones.[26,27] The N-H bond from the amide group also contributes to this non-radiative quenching of

luminescence and is accounted for in the equation (1) through term 0.06x to get more accurate value of 'q'. The 'q' value for 6a-6d polymers were found to be 0.73, 0.77, 0.73 and 0.80 respectively, which implies presence of ~1 water coordination site per repeat unit or per chelate structure. This information is interesting as it points to the fact that these structures have a similar water coordination number to Magnevist, yet, these polymers, on a per Gd basis, have 2 times the relaxivity profiles. This observation points to the fact that the polymer structure plays a large role in the observed imaging capability.

Table 2-2: Luminescence lifetimes of **6a-6d** Tb in H_2O and D_2O to calculate q

Sample	**τ_{D2O}, ms**	**τ_{H2O}, ms**	**q**
6a	2.895±0.035	1.614±0.022	0.77±0.041
6b	2.796±0.035	1.603±0.022	0.73±0.041
6c	2.695±0.023	1.569±0.015	0.73±0.027
6d	2.752±0.034	1.553±0.028	0.80±0.044

3.7. ICP-MS analysis to determine lanthanide content of the polymers:

Table 2-3: Lanthanide content on % mass basis was detemined using inductively coupled plasma mass spectrometer (ICP-MS).

Polymer	Calculated lanthanide content (%)	Observed lanthanide content (%)
6a Gd	22.4	17.1
6a Tb	22.6	17.5
6b Gd	21.1	18.3
6b Tb	21.3	17.7
6c Tb	20.1	17.4
6d Tb	19.1	16.2

3.8. Cell Culture Studies

3.8.1. Luciferase assay in U87 cells to monitor transfection efficiency:

U87 cells were transfected with polyplexes formulated with pDNA containing the Luciferase reporter gene (gWiz-Luc, 0.02 mg/mL) and series of lanthanide containing (Gd or Tb) polymers containing varying number of amines along polymer backbone (3-to-6 amines/repeat unit, 6a-6d). Transfection efficiency and viability of cells exposed to the lanthanide polymers (at N/P 40) was compared to cells transfected with G4 or Glycofect (N/P 20, positive control), naked pDNA (negative control) and untransfected cells. The luminescence (measured in relative light unit, RLU) from the protein expressed by the pDNA encoding firefly Luciferase was used to study transfection and amount of protein in cell lysates was used to determine viability relative to untransfected cells. The viability of all the lanthanide polymers and G4 was about 100% (Figure 2-5a). Transfection efficiency of the G4 polymer was highest among the samples tested. For the lanthanide polymers, there is no obvious trend, however, the transfection efficiency was

significantly higher for N6 (**6d**) series (for both Tb and Gd analogues) compared to N3-N5 polymers (**6a-6c**). The N3 (**6c**) and the N4 Gd (**6b** Gd) showed anomalous behavior. Currently, we are studying transfection efficiencies in different cell lines to investigate effect of amine number on transfection efficiency.

3.8.2. MTT assay to study cellular toxicity in U87cells:

The MTT assay was carried out to investigate toxicity profiles of different polymers (**6a-6d**, Gd and Tb) and compare them to naked pDNA (positive control) and untranfected cells. Cell viability of all the samples was determined via absorbance measurement of purple formazan at 595 nm in each well. All of the lanthanide containing polymers (**6a-6d** Gd and Tb) showed (Figure 2-5b) no toxicity (viability ~100%) in U87 cells at N/P 40. Jet-PEI (negative control at N/P 5) showed only 50% cell survival 24h post transfection. These results are promising to further pursue gene delivery studies of lanthanide polymers in different cell lines and potentially *in vivo*.

(a) (b)

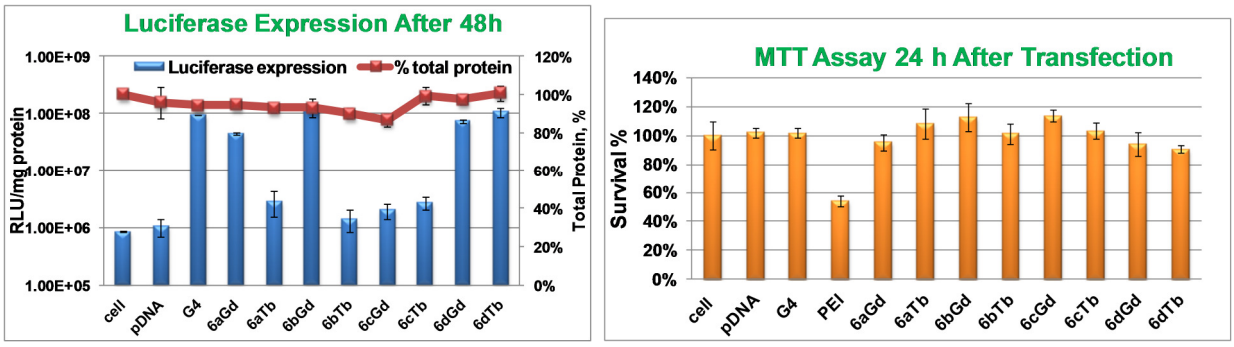

Figure 2-5: Luciferase expression (a) and MTT (b) assay were performed 48h after transfection in U-87 cell line to study transfection efficiencies and cytotoxicity of the different polymers (**6a-6d**, Gd and Tb analogues) at N/P 40, compared with Glycofect ™ or G4 (positive control at N/P 20), Jet-PEI (negative controls, N/P 5), naked pDNA and untransfected cells. (a) primary y-axis

(bar graph) represents RLU per mg of protein expressed whereas secondary y-axis (line graph) indicates total protein expressed which is an indicative of the cell viability; (b) all the samples except Jet-PEI had ~100% cell survival.

4. Discussion:

We have designed and developed novel lanthanide containing theranostic polymers with different amine number (three to six) and different lanthanide functionality (Gd or Tb) for pDNA delivery. These polymers contain oligoethylene amine domain which can bind to pDNA electrostatically and compact it into nanoparticle and lanthanide binding domain that can be utilized for diagnostic imaging. The Tb-chelated polymer can be used to study intracellular trafficking via fluorescence imaging and Gd-chelated polymer can be used as a contrast agent for MR imaging in vivo. These polymers were synthesized via step growth polymerization of oligoethylene diamine and DTPA-BA monomers and have degree of polymerization between 18-24.

The effect of amine number on pDNA binding ratio or N/P ratio was determined using gel electrophoresis assay. This assay revealed that the N/P binding ratio decreased from 40 to 5 with increase in amine number from three to six along the polymer backbone. The particle size as determined by DLS showed no change in particle size with amine number, however, there was a slight decrease in size with the increase in N/P ratio from 5 to 40 (due to more compact binding). All the polyplexes had hydrodynamic diameter between 50-80 nm. The zeta potential measurements indicated that at the same N/P ratio of 40, zeta potential values in pure water increased from +25 mV to +50 mV with increase in amine number. The effect on T_1 relaxivity of water in presence of Gd polymers was determined at 0.47 T and 1.41 T using a Minispec

instrument by measuring the R_1 (relaxation rate) values for **6a-6dGd** polymers and their complexes with pDNA at the N/P ratio of 40. The R_1 values when compared to that of Magnevist™ (a clinical contrast agent), were two times higher on per Gd basis at similar magnetic fields. The number of water coordination for all of these polymers (determined by Horrock's equation) is same as that of Magnevist™, which means that the increase in R_1 is primarily due to the polymer structure. These results are promising to use these polymers further for MR imaging. The MTT assay on cultured U-87 cells at 24 h after transfection indicated no significant toxicity (~ 100% cell survival) from both Gd and Tb analogues of all the polymers. The transfection efficiency determined using standard Luciferase expression assay at 48 h after transfection in U-87 cells indicated increase in transfection efficiency with the amine number with anomalies of **6aGd** and **6bGd** polymers. Current efforts are directed toward understanding the unusual trend in transfection of U-87 cells and exploring different cell types for the pDNA delivery.

5. Acknowledgements

This project was funded by National Science Foundation. Authors would like to thank Prof. Valerie Pierre at U of Minnesota (Cary Eclipse fluorescence spectrometer); Prof. Webster Santos (gel box) and Prof. Richey Davis (DLS) at Virginia Tech for use of instruments. S.K. would like to thank Dr. Karina Kizjakina, Dr. Antons Sizovs and Dr. Josh Bryson for helpful discussion with the synthesis. Authors would also like to thank Techulon Inc. for generous donation of Glycofect™.

References:

(1) Siegel, R.; Naishadham, D.; Jemal, A. *CA Cancer J Clin* **2012**, Cancer statistics, 2012, *62*, 10-29.

(2) Adams, D. J. *Trends Pharmacol. Sci.* **2012**, The Valley of Death in anticancer drug development: a reassessment, *33*, 173-180.

(3) Sizovs, A.; McLendon, P. M.; Srinivasachari, S.; Reineke, T. M. *Top. Curr. Chem.* **2010**, Carbohydrate polymers for nonviral nucleic acid delivery, *296*, 131-190.

(4) Mintzer, M. A.; Simanek, E. E. *Chem. Rev.* **2009**, Nonviral Vectors for Gene Delivery, *109*, 259-302.

(5) Davis, M. E.; Chen, Z.; Shin, D. M. *Nat. Rev. Drug Discovery* **2008**, Nanoparticle therapeutics: an emerging treatment modality for cancer, *7*, 771-782.

(6) Iyer, A. K.; Khaled, G.; Fang, J.; Maeda, H. *Drug Discovery Today* **2006**, Exploiting the enhanced permeability and retention effect for tumor targeting, *11*, 812-818.

(7) Maeda, H.; Greish, K.; Fang, J. *Adv. Polym. Sci.* **2006**, The EPR effect and polymeric drugs: A paradigm shift for cancer chemotherapy in the 21st century, *193*, 103-121.

(8) Lammers, T.; Aime, S.; Hennink, W. E.; Storm, G.; Kiessling, F. *Acc. Chem. Res.* **2011**, Theranostic Nanomedicines, *44*, 1029-1038.

(9) Kelkar, S. S.; Reineke, T. M. *Bioconjugate Chem.* **2011**, Theranostics: Combining Imaging and Therapy, *22*, 1879-1903.

(10) Perry, J. L.; Herlihy, K. P.; Napier, M. E.; DeSimone, J. M. *Acc. Chem. Res.* **2011**, PRINT: A Novel Platform Toward Shape and Size Specific Nanoparticle Theranostics, *44*, 990-998.

(11) Kunjachan, S.; Jayapaul, J.; Mertens, M. E.; Storm, G.; Kiessling, F.; Lammers, T. *Curr. Pharm. Biotechnol.* **2012**, Theranostic systems and strategies for monitoring nanomedicine-mediated drug targeting, *13*, 609-622.

(12) Villaraza, A. J. L.; Bumb, A.; Brechbiel, M. W. *Chem. Rev.* **2010**, Macromolecules, Dendrimers, and Nanomaterials in Magnetic Resonance Imaging: The Interplay between Size, Function, and Pharmacokinetics, *110*, 2921-2959.

(13) Chang, Y.-H.; Chen, C.-Y.; Singh, G.; Chen, H.-Y.; Liu, G.-C.; Goan, Y.-G.; Aime, S.; Wang, Y.-M. *Inorg. Chem.* **2011**, Synthesis and physicochemical characterization of carbon backbone modified [Gd(TTDA)(H2O)]2- derivatives, *50*, 1275-87.

(14) Chen, Y.; Chen, H.; Zhang, S.; Chen, F.; Sun, S.; He, Q.; Ma, M.; Wang, X.; Wu, H.; Zhang, L.; Zhang, L.; Shi, J. *Biomaterials* **2012**, Structure-property relationships in manganese oxide - mesoporous silica nanoparticles used for T1-weighted MRI and simultaneous anti-cancer drug delivery, *33*, 2388-2398.

(15) Bunzli Jean-Claude, G.; Piguet, C. *Chem. Soc. Rev.* **2005**, Taking advantage of luminescent lanthanide ions, *34*, 1048-77.

(16) Shen, J.; Zhao, L.; Han, G. *Adv. Drug Delivery Rev.* **2012**, Lanthanide-doped upconverting luminescent nanoparticle platforms for optical imaging-guided drug delivery and therapy, Ahead of Print.

(17) Doane, T. L.; Burda, C. *Chem. Soc. Rev.* **2012**, The unique role of nanoparticles in nanomedicine: imaging, drug delivery and therapy, *41*, 2885-2911.

(18) Selvin, P. R. *Annu. Rev. Biophys. Biomol. Struct.* **2002**, Principles and biophysical applications of lanthanide-based probes, *31*, 275-302.

(19) Bryson, J. M.; Fichter, K. M.; Chu, W.-J.; Lee, J.-H.; Li, J.; Madsen, L. A.; McLendon, P. M.; Reineke, T. M. *Proc. Natl. Acad. Sci. U. S. A.* **2009**, Polymer beacons for luminescence and magnetic resonance imaging of DNA delivery, *106*, 16913-16918.

(20) Srinivasachari, S.; Liu, Y.; Zhang, G.; Prevette, L.; Reineke, T. M. *J. Am. Chem. Soc.* **2006**, Trehalose Click Polymers Inhibit Nanoparticle Aggregation and Promote pDNA Delivery in Serum, *128*, 8176-8184.

(21) Kizjakina, K.; Bryson, J. M.; Grandinetti, G.; Reineke, T. M. *Biomaterials* **2012**

Cationic glycopolymers for the delivery of pDNA to human dermal fibroblasts and rat mesenchymal stem cells, *33*, 1851-1862.

(22) Prudencio, M.; Rohovec, J.; Peters, J. A.; Tocheva, E.; Boulanger, M. J.; Murphy, M. E. P.; Hupkes, H.-J.; Kosters, W.; Impagliazzo, A.; Ubbink, M. *Chem. Eur. J.* **2004**, A caged lanthanide complex as a paramagnetic shift agent for protein NMR, *10*, 3252-3260.

(23) Carpino, L. A. *Accounts Chem. Res.* **1973**, New amino-protecting groups in organic synthesis, *6*, 191-8.

(24) Supkowski, R. M.; Horrocks, W. D., Jr. *Inorg. Chim. Acta* **2002**, On the determination of the number of water molecules, q, coordinated to europium(III) ions in solution from luminescence decay lifetimes, *340*, 44-48.

(25) Thibon, A.; Pierre, V. C. *Anal. Bioanal. Chem.* **2009**, Principles of responsive lanthanide-based luminescent probes for cellular imaging, *394*, 107-120.

(26) Hemmila, I.; Laitala, V. *J Fluoresc* **2005**, Progress in lanthanides as luminescent probes, *15*, 529-42.

(27) Horrocks, W. D., Jr.; Sudnick, D. R. *J. Am. Chem. Soc.* **1979**, Lanthanide ion probes of structure in biology. Laser-induced luminescence decay constants provide a direct measure of the number of metal-coordinated water molecules, *101*, 334-40.

Chapter 3 : Monitoring polyplex dissociation in vitro using lanthanide resonance energy transfer (LRET)

Abstract:

Monitoring of intracellular trafficking and cargo release is crucial for designing new and efficient vehicles for gene and drug delivery. This has traditionally been done by labeling nucleic acids with fluorescent dyes such as cyanine, rhodamine, and APC dyes, however, these methods do not examine trafficking of vehicle or its release kinetics. Fluorescent resonance energy transfer has been developed to study release kinetics of polyplexes/nanoparticle by labeling them with "FRET pair" dyes. Lanthanide resonance energy transfer (LRET) possesses several advantages over FRET and has been used to study protein-protein interactions or changes in protein conformation. Herein, this is the first study to expand LRET techniques to examine polyplex formation-dissociation in solution.

We have designed novel lanthanide (Gd, Tb or La) containing polymers with oligoethyleneamine and lanthanide chelating units to incorporate DNA binding and imaging agent functionality. Protonable amines along the polymer backbone electrostatically interact with DNA and compact it into a nanoparticle. These nanoparticles can be imaged both *in vivo* (Gd analogues, magnetic resonance imaging) and intracellularly (Tb chelation, fluorescence spectroscopy). Polymers were synthesized (as described in Chapter 2) via step-growth polymerization to achieve a degree of polymerization of 18-24 for different analogues with varying amine number (three to six, N3-N6, **6a-6d**) along the backbone. Here, we describe LRET monitoring of terbium-chelated N5Tb (**6cTb**) polymer with pDNA containing its LRET pair, tetramethyl rhodamine (TMR) to study polyplex association and dissociation dynamics. For our studies *in vitro*, we have observed a significant decrease (~ 43%) in luminescence intensity

of the polymer in the presence of TMR labeled DNA at different N/P ratios. This effect is reversed upon the increase in distance between polymer-DNA (by addition NaCl) and dissociation of polyplexes (by competitive binding with heparin sulfate). This method allows us to understand the association and dissociation of these lanthanide polymers towards polyplex formation.

1. Introduction:

Monitoring every step (delivery, release and efficacy) involved in therapeutic (drug and nucleic acid) delivery is crucial to move forward translational research of nanomedicines biomaterials. Tracking of nanocomplexes containing polynucleotides from the extracellular matrix into the cell and their transport to the cytoplasm (for siRNA delivery) or the nucleus (for pDNA delivery) has traditionally been completed by labeling nucleic acids and cell organelles with suitable fluorescent markers and studying their co localization signals. [1] While this method gives information about trafficking pathways and kinetics, further methods to monitor polyplex dissociation-association would allow the detection of the onset of the dissociation but with the inherently low spatial resolution associated with fluorescence dye imaging. With the conventional fluorophores, the polymer and the nucleic acid have to diffuse quite far from each other to be considered dissociated, hence two fluorophores without any chemical/biological interaction could appear to have co-localized signals due to their spatial proximity and thus can provide misleading information about polyplex dynamics. [2]

Fluorescence resonance energy transfer (FRET), which relies on (nanometer range) distance-dependent non-radiative energy transfer between two chromophores (donor and acceptor), can provide useful insights into drug/gene delivery and the release of the vehicle from

the payload. [3, 4] The concept of fluorescence resonance energy transfer was first introduced by Förster about half a century ago.[5] Two chromophores with a spectral overlap and spatial proximity of 10-100Aº can act as "FRET" pairs.[6, 7] When FRET dyes are within a distance of 10-100 Aº, the donor fluorophore (when excited) will transfer its energy to an acceptor (not required to be fluorescent). This would result in a 'FRET ON' signal, a decrease or quenching of emission intensity and fluorescence lifetime of a donor and increase in "sensitized emission" intensity of an acceptor (if fluorescent). [8, 9] Conversely, when donor and acceptor molecules are separated, (beyond the 'FRET pair distance') the lack of energy transfer will cause the 'FRET OFF' effect. FRET is capable of resolving interactions on the molecular level and is a better tool to understand structural or conformational changes (in response to external stimuli) compared to any existing optical technique (which operates at larger distances).[10] Several methods that are used to measure the FRET efficiency include the measurement of donor and/or acceptor emission, donor lifetime, and/or fluorescence anisotropy. [11]

FRET studies performed using organic dyes have drawbacks such as photobleaching, short fluorescence lifetimes (prohibits use of time-lapse studies), and spectral cross-talk (emission of one fluorophore being detected in the filter for the other due to spectral overlap). To overcome these limitations, inorganic nanoparticles based on semiconductor quantum dots or luminescent lanthanides are currently being examined for this purpose and posses narrow emission peaks, do not photobleach, have large Stoke's shifts and fluorescence lifetimes, and finally, can offer tunable emission wavelengths in the near-IR to delete background autofluorescence.[12]

There are several examples[3, 13-15] of QD-based FRET systems for monitoring of nucleic acid delivery and unpackaging with polymeric and lipid-based carriers. Leong and coworkers[16]

have studied polyplex dynamics (polyplex formation and release and DNA degradation) with Chitosan and polyethylene glycol-polyphosphoramidate block copolymer (PEG-b-PPA). They used tri-color FRET consist of QD and cyanine dye- (BOBO-3 or Cy3) labeled pDNA and Cy5-labeled polymer. Turning 'ON' and 'OFF' of fluorescence (FRET) signal was used to monitor intracellular release and degradation of pDNA.

Luminescent lanthanides can be used as FRET donors to organic dyes or QDs. Since, lanthanide luminescence is technically not a fluorescence signal (i.e. not arising from singlet to singlet transitions), lanthanide-based resonance energy transfer is known as "lanthanide or luminescence energy transfer" (LRET). [9] LRET has been used to study protein-protein interactions in high-throughput screening of antibacterial drugs.[17] In this study, the binding between europium labeled sigma factor (σ-70) and Cy-5 labeled RNA polymerase was studied by monitoring change in LRET signal from Cy-5 (acceptor) emission. Even though the underlying mechanism for LRET is same as FRET, LRET provides several advantages over FRET such as- larger measurable distances (>100Aº), higher signal to noise ratio and long fluorescence lifetimes.

Europium and terbium are considered highly luminescent among the series of luminescent lanthanide ions (europium, terbium, samarium, dysprosium, ytterbium, neodynamium, and erbium) due to significantly longer luminescence lifetimes (100-1500 μs vs 0.03-50 μs). Lanthanide chelates as termed by Zhang et al.[18] are "next generation fluorophores" for live cell imaging and monitoring intracellular trafficking.[11, 19] The long luminescence lifetimes of the lanthanide ions is attributed to spectral characteristics of f-f shell orbital transitions that are spin and Laporte forbidden.[20] Terbium chelates have four distinct emissions bands- 490 nm ($^5D_4$-$^7F_6$), 545 nm ($^5D_4$-$^7F_5$), 583 nm ($^5D_4$-$^7F_4$) and 620 nm ($^5D_4$-$^7F_3$) that can be

used for multicolor and multifluorophore FRET detections with common organic dyes.[21] For example, Tb can transfer energy to Fluorescein through $^5D_4$-$^7F_6$ transition (490 nm) whereas Cy3, phycoerythrin, rhodamine derivatives or Alexa® dyes can be acceptors for 545 nm emission.[19]

In this study, we have developed a LRET-based method to monitor polyplex unpackaging *in vitro* using a Tb-chelated polymer (donor fluorophore) and tetramethyl rhodamine (TMR, acceptor)-labeled pDNA (7-8 kbp). Terbium-TMR 'LRET pair' has been used to study a change in protein conformations, and protein-protein interactions; however, to the best of our knowledge, this is the first study to monitor polyplex unpackaging using LRET.[22-24] In this report, LRET efficiency was monitored via change in donor (Tb) intensity upon formation and dissociation/destabilization of polyplexes. Studies were performed at different N/P ratios (ratio of number of nitrogens on polymer to number of phosphate groups on DNA backbone) of polymer N5 Tb (polymer analogue with five amines per repeat unit). Change in donor intensity was monitored using time-delayed (100μs) measurement to avoid any background autofluorescence or direct excitation of acceptors. Results obtained with *in vitro* preliminary work are promising and suggest pursuit of further research in live or fixed cells.

(a) (b)

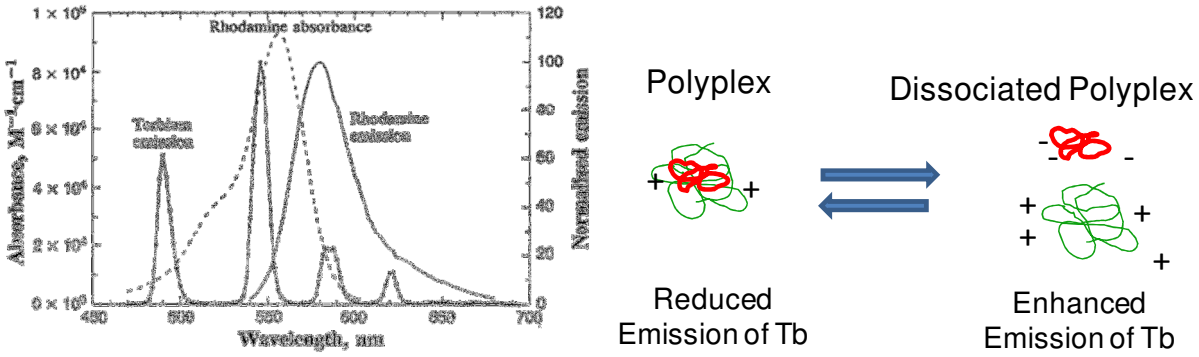

Figure 3-1: (a) Graphical representation of "high spectral overlap" between Tb and TMR. Figure adapted from reference[25] (b) Vehicle unpackaging for polyplexes can be monitored using decrease or increase in Tb emission.

2. Experimental

2.1. Materials:

$TbCl_3$ and HEPES salt were obtained from Sigma Aldrich (USA) and used without further purification. 20mM HEPES buffer was prepared with ultrapure MiliQ water and the solution pH 7 was adjusted using saturated solution of sodium bicarbonate. The plasmid DNA used in this study, gWiz-Luc, was purchased from Alderveron (Fargo, ND). TMR labeling kit was purchased from Invitrogen (Carlsbad, CA) and labeled using the manufacturer's protocol to achieve a 1:5 labeling ratio between pDNA and the TMR dye. Sodium chloride was obtained from Fisher Scientific and Heparin Sodium salt was obtained from Alfa Aesar. **6cTb** polymer (DP= 24) was synthesized *via* step-growth polymerization as described in Chapter 2. **6cTb** polymer was chosen as a model to investigate the hypothesis of monitoring polyplex association and dissociation via LRET between Tb and TMR dye.

All luminescence/fluorescence measurements were performed on Spectra-Max –M2 micro plate-reader from Molecular Devices (Sunnyvale, CA) or Cary Fluorescence Spectrometer (Agilent Technologies, USA; formerly Varian) and analyzed on Spectra-Max or WinFLR software respectively.

2.2. Methods:

2.2.1. General procedure for preparation of polyplexes with Tb polymer and TMR-labeled DNA:

Polyplexes were formed at N/Ps 20 and 40 by mixing equal volumes (50 µL) of Tb polymer and TMR DNA (0.1µg/µL) at room temperature and incubated for 30 min. Control samples were as follows: polymer only (50 µL of polymer + 50 µL of water), pDNA only (50µL of pDNA + 50 µL of water), and unlabeled polyplexes (polyplexes formed with Tb polymer and unlabeled pDNA).

2.2.2. Monitoring change in Tb emission intensity upon polyplex formation:

30 min after polyplex formation, 90 µL of each polyplex solution was pipetted into each well of a 96-well plate and analyzed for luminescence intensity of Tb using a microplate reader. Luminescence intensity in each well was measured with a 90-100 µs delay time using end point (excitation 350 ± 5 nm, emission at 545 ± 5 nm) and full-spectral scan (400-700 nm) type measurements. Time delayed (90-100 µs) measurements were performed to avoid signal interference from direct excitation of TMR and short-lived background fluorescence.

2.2.3. Gel electrophoresis shift assay for polyplex destabilization:

Polyplexes were formulated by mixing equal volumes (10 µL) of polymer solution and (unlabeled) pDNA (0.1 mg/mL) to achieve an N/P ratio of 40 for the polyplexes; the polyplex solutions were subsequently incubated at room temperature for 30min to allow binding. Next, 10

µL of NaCl (1.0 M in 20mM HEPES buffer) or Heparin sulfate solution (100-1000 µg/mL) was added to each polyplex and incubated further for 15 min. Control samples were prepared by mixing 10 µL of water with N/P 40 and N/P 0 (pDNA only) polyplexes. Gel loading buffer (1 µL, Blue juice, Invitrogen, Carlsbad, CA) was added to each solution before depositing 10 µL of each solution into the well. Dissociation of pDNA from polyplexes was studied *via* gel electrophoresis shift assay. Agarose gel (0.6 w/v %) containing ethidium bromide (0.06 w/v %) was prepared in Tris-acetate EDTA (TAE) buffer (40 mM Tris-acetate, 1 mM EDTA, pH 8) and migration of DNA toward anode was observed under applied electrophoretic field (65 mV, 60 min).

2.2.4. Particle size measurement upon addition of NaCl and Heparin:

Change in particle size upon addition of NaCl and Heparin was monitored *via* DLS. Polyplexes were formulated by mixing equal volumes (200 µL) of polymer (6cTb) and (unlabeled) pDNA at N/P 40. The polyplex size was measured before and after addition of 200 µL of 1M NaCl solution (in 20mM HEPES buffer) or Heparin solution (500 µg/mL in water). Dynamic light scattering was performed using Zetasizer Nanoseries from Malvern Instruments (Malvern, UK) equipped with 633nm wavelength laser at 25°C .

2.2.5. Monitoring change in Tb emission upon NaCl and Heparin addition:

The electrostatic interactions between polymer and pDNA can be disrupted by addition of inorganic salt (1M NaCl) or a competitive polyanion such as heparin. NaCl destabilizes the interaction between the polymer and pDNA[26] leads to swelling or aggregation of nanoparticles (section 2.2.4.) Heparin, a polyanion can compete with DNA to form nanoparticles with polymer[27] and thus disrupts the polymer-DNA binding. Both of these events cause a change in the distance between the donor (Tb) and acceptor (TMR), which can be monitored *via* LRET.

The concentration of Heparin at which the dissociation takes place was determined to be 500 µg/mL *via* a gel electrophoresis assay (section 2.2.3.). For both the destabilization experiments, polyplexes were formulated at N/P ratios of 40 and 20. Polyplexes at different N/Ps and control samples were formulated as described above (section 2.2.1.). After 30 min, 90 µL of each of the solution was pipetted into 96-well plate and Tb emission was monitored with time delayed (90-100 µs) end point measurement (excitation 350 ± 5 nm, emission at 545 ± 5 nm).

Next, 50 µL of 1M NaCl in HEPES buffer (20 mM) or Heparin solution (500 µg/mL concentration) was added to each polyplex and control samples-containing wells. All the samples were incubated further for 15 min and analyzed for change in Tb luminescence intensity.

3. Results and Discussions

*3.1. Change in luminescence intensity upon formation of polyplexes***:**

Luminescence intensity of terbium polymer decreased significantly upon formation of polyplexes with TMR labeled DNA due to non-radiative energy transfer (figure 3-2). Lanthanide luminescence (at 490, 545, 590 and 620 nm) was quenched (43%) upon polyplex formation as compared to control samples of polymer and polyplexes with unlabeled pDNA at the same N/P ratio of 40 (Figure 3-2a), indicating that DNA by itself is not an effective acceptor in this energy transfer process. Luminescence quenching of Tb polymer was also observed at N/Ps 20, 10 and 5 compared to the controls.

(a) (b)

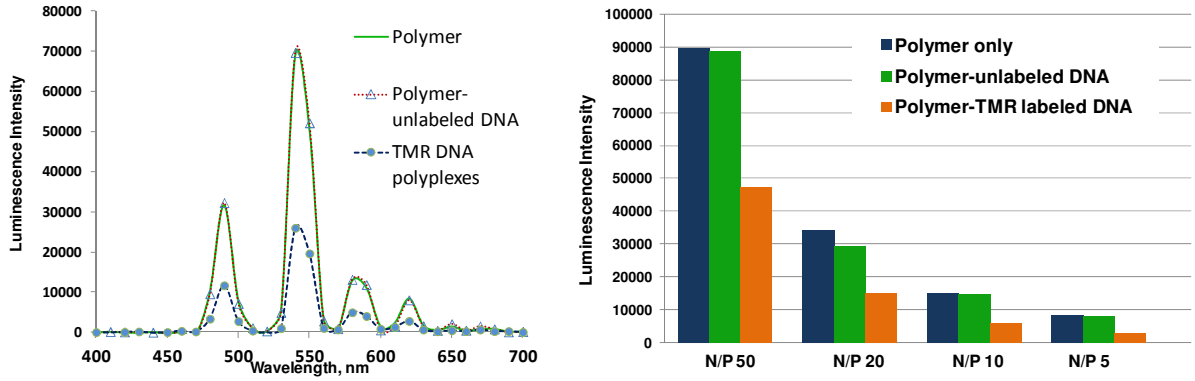

Figure 3-2: (a) An overlay of the luminescence spectra of the lanthanide polymer **6cTb** (ex=350 nm) (green solid line), the **6cTb** polymer complexed to unlabeled pDNA at an N/P ratio of 40 (pink dotted line with triangles), and the **6cTb** polymer complexed with TMR labeled pDNA at an N/P ratio of 40 (blue dotted line with circles). (b) A plot of the change in luminescence intensity (at 545 nm) of the **6cTb** polymer (blue bars), **6cTb** polymer complexed with unlabeled pDNA (green bars), and the **6cTb** polymer complexed with TMR labeled pDNA (orange bars) as monitored at different N/P ratios.

3.2. Gel electrophoresis shift assay and DLS studies after Heparin and NaCl addition:

Polyplexes formulated with N5Tb at N/P 40 were subjected to gel electrophoresis after treating with different concentrations of heparin (100-500 µg/mL) and 1M NaCl. The heparin began to disrupt the polymer-DNA binding at about 450 µg/mL heparin concentration, however, NaCl was not able to completely release DNA from the polyplex (Figure 3-3). This indicates that the polyplex formation is stable and a multivalent anion (such as heparin) is needed to fully dissociate the polyplexes. These data are interesting as they indicate that the polyplexes are likely stable in the physiological salt conditions from dissociation and that a strong interaction with biological polyanions are needed to facilitate pDNA release.

DLS data shows (Figure 3-4) that the addition of NaCl to the polyplexes at N/P 40 results in significant increase in size (from 60 nm to 100 nm). This can be attributed to disruption of electrostatic interaction between polymer and DNA which can lead to swelling or aggregation of nanoparticles. However, in the case of heparin, no significant variation in size was observed (Figure 5). This was further investigated by comparing the size of polymer-DNA and polymer-heparin complexes (Figure 3-5) and both the complexes possess similar particle size (60-80 nm). The addition of heparin to polyplexes leads to a complex system consisting of polymer-DNA, polymer-heparin and polyplex-heparin interactions that cannot be distinguished easily by DLS measurement. The results from gel electrophoresis assays (Figure 3-3, indicated by migration of unbound DNA toward anode) provide convincing evidence of disruption of polymer-DNA binding.

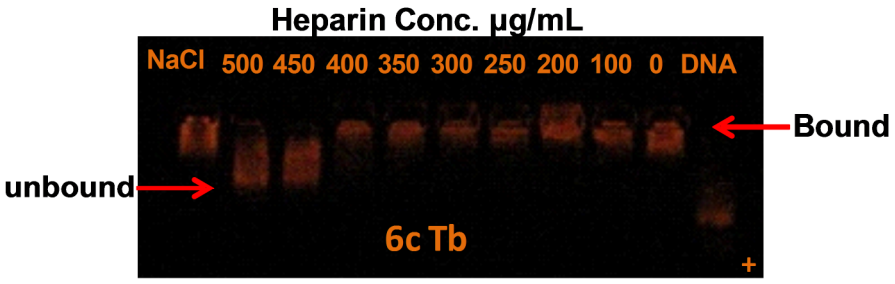

Figure 3-3: Gel electrophoresis shift assay was performed on 6cTb polyplexes formulated at N/P ratio of 40 after addition of different concentrations of heparin (indicated by numbers from 0-500 µg/mL) and NaCl (at 1M concentration). The binding of pDNA to the polymer is indicated by the inhibition of migration of the orange colored band toward positive electrode.

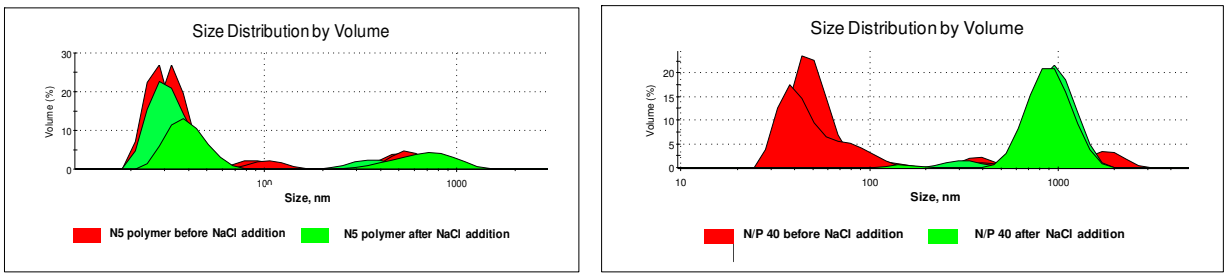

Figure 3-4: A graph of size distribution by volume (measured by DLS) for **6cTb** polymer (left) and **6cTb** complexed with pDNA at N/P ratio 40 (right) before (red) and after (green) addition of 1M NaCl (in 20mM HEPES) is shown. The size distribution for **6cTb** polymer remains unchanged (overlayed green and red graphs) upon addition of NaCl, whereas, distribution of **6cTb** polyplexes at N/P ratio of 40 shifts (from red graph around 50 nm) toward the higher particle size distribution (~1000nm, green) upon addition of NaCl.

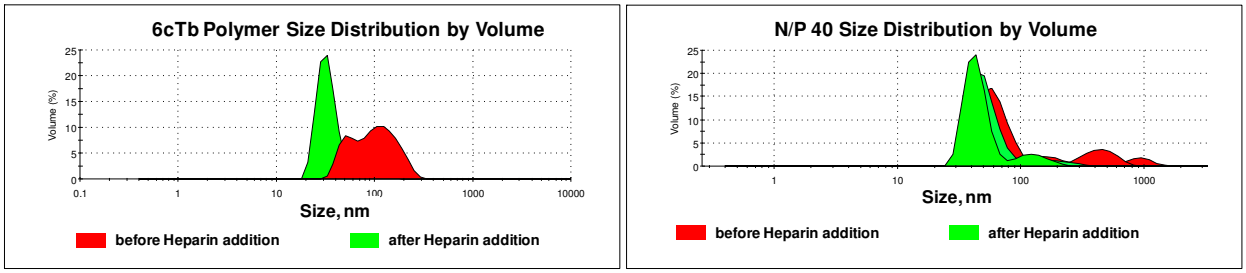

Figure 3-5: A graph of size distribution by volume (measured by DLS) for **6cTb** polymer (left) and **6cTb** complexed with pDNA at N/P ratio 40 (right) before (red) and after (green) addition of 500 µg/mL heparin solution (in pure water) is shown. The size distribution for **6cTb** polymer and **6cTb** polyplexes at N/P ratio of 40 remain unchanged (overlayed green and red graphs) upon addition of heparin solution.

3.3. Change in terbium emission upon polyplex destabilization:

According to LRET theory,[6, 25, 28] when the donor and acceptor are separated by more than 100 A^0, the 'LRET' effect is reversed (i.e. no change in donor emission intensity in presence of acceptor). This phenomenon was tested by monitoring the change (or increase) in

the donor (Tb) emission upon polyplex dissociation/destabilization by addition of 1 M NaCl (in 20mM HEPES buffer) or heparin solution (500 µg/mL in water). The addition of NaCl disrupts the electrostatic interaction between polymer and DNA resulting in a larger particle size (Figure 3-4), however, it does not release DNA from the polyplex (Figure 3-3). The monitoring of LRET (via increase in Tb emission intensity) upon addition of NaCl is possible due to increase in distance between the LRET pairs (Tb chelated polymer and TMR labeled pDNA) (DLS data in figure 3-4). In the case of heparin addition, due to competitive binding between the cationic polymers and pDNA or heparin, the pDNA is released from the polyplex (Figure 3-3). Both of these events change the distance between donor and acceptor and thus can be monitored via change in emission of Tb.

Polyplexes were formulated at N/Ps 40 and 20 and Tb emission was measured at 545 nm before and after addition of heparin and NaCl. For polyplexes at N/P 40 and 20, all the quenching was released back after addition of heparin (Figure 3-6). For polyplexes treated with NaCl, the increase in intensity was about 80% of the original (Figure 3-7).

(a) (b)

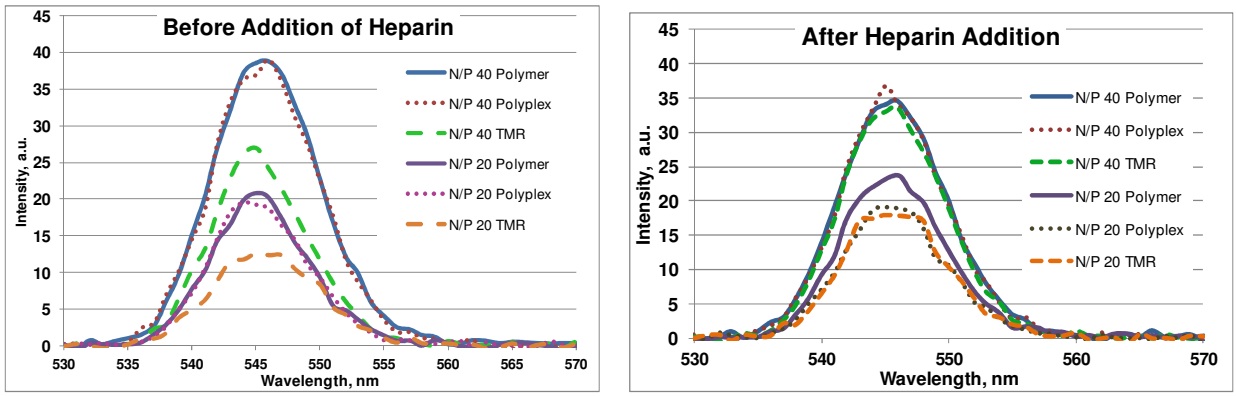

Figure 3-6: An overlay of the change in luminescence intensity (emission at 545 nm) of **6cTb** polymer (ex=350 nm)(blue and purple solid curves), **6cTb** polymer complexed with unlabeled pDNA at N/P ratios of 40 and 20 (red and pink dotted curves respectively), and **6cTb** polymer complexed with TMR labeled pDNA at N/P ratios of 40 and 20 (green and orange dotted curves respectively) before (a) and after (b) addition of 500 µg/mL heparin solution.

(a) (b)

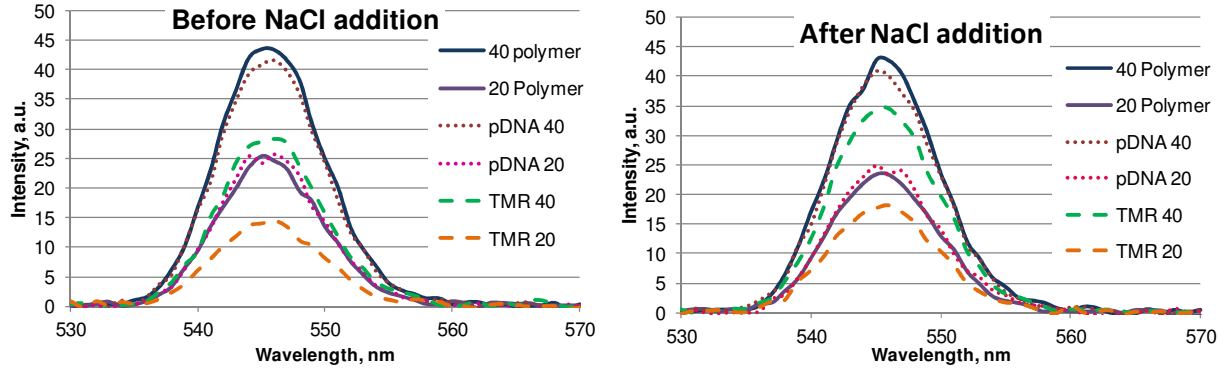

Figure 3-7: An overlay of the change in luminescence intensity (emission at 545 nm) of **6cTb** polymer (ex=350 nm)(solid blue and purple curves), **6cTb** polymer complexed with unlabeled pDNA at N/P ratios of 40 and 20 (red and pink dotted curves respectively), and **6cTb** polymer complexed with TMR labeled pDNA at N/P ratios of 40 and 20 (green and orange dotted curves respectively) before (a) and after (b) addition of 1M NaCl solution.

In this study, we have shown that changing the distance between donor and acceptor can be detected by monitoring change in emission intensity of the donor. FRET has been used to study association and dissociation of the polyplexes in vitro by monitoring change in emission of the donor or the acceptor.[6, 10, 16] For our studies, we observed significant decrease in emission intensity of the Tb-chelated polymer (~43%) when complexed with TMR pDNA at different N/P ratios. This effect was reversed (increase in Tb emission intensity) upon addition of NaCl or heparin sulfate, which destabilize the polyplexes by weakening the electrostatic interaction between polymer and DNA and begin its dissociation.

4. Discussion:

In this study, we have developed LRET based tool to monitor polyplex association and dissociation. We have synthesized Tb-chelated polymer with five number of amines along the polymer backbone and labeled TMR dye onto a pDNA. We have monitored significant decrease in emission of Tb (`43%) at 545 nm upon formation of complexes with TMR pDNA at different N/P ratios: 50, 40, 20, 10 and 5. However, the emission intensity of Tb polymer remained unchanged in polyplexes formulated with unlabeled pDNA, indicating that the pDNA itself if not a LRET acceptor. This effect was reversed upon addition of NaCl or heparin solution. These reagents can destabilize polyplex by weakening the electrostatic interaction between cationic polymer and anionic DNA. This causes increase in distance between donor and the acceptor which can be monitored. During our study, we observed complete recovery of Tb emission upon addition of heparin and 80% recovery with NaCl addition. Thus, we have shown that both polyplex formation and destabilization/dissociation can be monitored by change in emission of Tb polymer (donor).

Lanthanide resonance energy transfer is a promising tool in the area of therapeutic delivery due to its inherent benefits such as longer luminescence lifetimes, elimination of background fluorescence and high signal to noise ratio. In this report, we have developed LRET-based method to distinguish compact vs. destabilized polyplexes *in vitro*. During our studies, we were able to measure dramatic change in luminescence intensity of Tb polymer in presence/ absence of TMR DNA, which can be attributed to the integrity of the polyplex structure. This was the first effort to monitor polyplex dissociation using LRET and this opens up avenues to investigate vehicle unpackaging *in cellulo* in future.

5. Acknowledgements

This work was funded by National Science Foundation. I would like to thank Prof. Tim Long and Prof. Tijana Grove for microplate reader usage and Drs. Nilesh Ingle and Giovanna Grandinetti for labeling of pDNA.

References:

(1) Kelkar, S. S., and Reineke, T. M. *Bioconjugate Chem.* **2011**, Theranostics: Combining Imaging and Therapy. *22*, 1879-1903.

(2) Chen, H. H., Ho, Y.-P., Jiang, X., Mao, H.-Q., Wang, T.-H., and Leong, K. W. *Mol. Ther.* **2008**, Quantitative Comparison of Intracellular Unpacking Kinetics of Polyplexes by a Model Constructed From Quantum Dot-FRET. *16*, 324-332.

(3) Cheng, S.-H., Chen, N.-T., Wu, C.-Y., Chung, C.-Y., Hwu, Y., Mou, C.-Y., Yang, C.-S., and Lo, L.-W. *J. Chin. Chem. Soc.* **2011**, Recent advances in dynamic monitoring of drug release of nanoparticle using Forster resonance energy transfer and fluorescence lifetime imaging. *58*, 798-804.

(4) Redy, O., and Shabat, D. *J Control. Release* **2012**, Modular Theranostic Prodrug based on a FRET-Activated Self-Immolative Linker.

(5) Forster, T. *Discussions of the Faraday Society No.* **1959**, Transfer mechanisms of electronic excitation. *27*, 7-17.

(6) Selvin, P. R. *Nature Structural Biology* **2000**, The renaissance of fluorescence resonance energy transfer. *7*, 730-734.

(7) Periasamy, A. *J. Biomed. Optics* **2001**, Fluorescence resonance energy transfer microscopy: a mini review. *6*, 287-291.

(8) Selvin, P. R. *Methods Enzymol.* **1995**, Fluorescence resonance energy transfer. *246*, 300-334.

(9) Selvin, P. R. *Annu. Rev. Biophys. Biomol. Struct.* **2002**, Principles and biophysical applications of lanthanide-based probes. *31*, 275-302.

(10) Chen, K.-J., Chiu, Y.-L., Chen, Y.-M., Ho, Y.-C., and Sung, H.-W. *Biomaterials* **2011**, Intracellularly monitoring/imaging the release of doxorubicin from pH-responsive nanoparticles using Foerster resonance energy transfer. *32*, 2586-2592.

(11) Kokko, T. **2009**, Lanthanide Chelates as Donors in Fluorescence Resonance Energy Transfer: Exciting Prospects for Bioaffinity Assay Detection, in *Biochemistry and Food Chemistry*, p 68, University of Turku, Turku, Finland.

(12) Xiao, M., and Selvin, P. R. *J. Am. Chem. Soc.* **2001**, Quantum Yields of Luminescent Lanthanide Chelates and Far-Red Dyes Measured by Resonance Energy Transfer. *123*, 7067-7073.

(13) Chen, A. A., Derfus, A. M., Khetani, S. R., and Bhatia, S. N. *Nucleic Acids Res.* **2005**, Quantum dots to monitor RNAi delivery and improve gene silencing. *33*, e190/191-e190/198.

(14) Tan, W. B., Jiang, S., and Zhang, Y. *Biomaterials* **2007**, Quantum-dot based nanoparticles for targeted silencing of HER2/neu gene via RNA interference. *28*, 1565-1571.

(15) Bagalkot, V., Zhang, L., Levy-Nissenbaum, E., Jon, S., Kantoff, P. W., Langer, R., and Farokhzad, O. C. *Nano Lett.* **2007**, Quantum Dot-Aptamer Conjugates for Synchronous Cancer Imaging, Therapy, and Sensing of Drug Delivery Based on Bi-Fluorescence Resonance Energy Transfer. *7*, 3065-3070.

(16) Chen, H. H., Ho, Y.-P., Jiang, X., Mao, H.-Q., Wang, T.-H., and Leong, K. W. *Nano Today* **2009**, Simultaneous non-invasive analysis of DNA condensation and stability by two-step QD-FRET. *4*, 125-134.

(17) Bergendahl, V., Heyduk, T., and Burgess, R. R. *Appl. Environ. Microbiol.* **2003**, Luminescence resonance energy transfer-based high-throughput screening assay for inhibitors of essential protein-protein interactions in bacterial RNA polymerase. *69*, 1492-1498.

(18) Guo, H., Idris, N. M., and Zhang, Y. *Langmuir* **2011**, LRET-Based Biodetection of DNA Release in Live Cells Using Surface-Modified Upconverting Fluorescent Nanoparticles. *27*, 2854-2860.

(19) Hemmila, I., and Laitala, V. *J Fluoresc* **2005**, Progress in lanthanides as luminescent probes. *15*, 529-542.

(20) Charbonniere, L. J., Hildebrandt, N., Ziessel, R. F., and Loehmannsroeben, H.-G. *J. Am. Chem. Soc.* **2006**, Lanthanides to Quantum Dots Resonance Energy Transfer in Time-Resolved Fluoro-Immunoassays and Luminescence Microscopy. *128*, 12800-12809.

(21) Kim, S. H., Gunther, J. R., and Katzenellenbogen, J. A. *J. Am. Chem. Soc.* **2010**, Monitoring a Coordinated Exchange Process in a Four-Component Biological Interaction System: Development of a Time-Resolved Terbium-Based One-Donor/Three-Acceptor Multicolor FRET System. *132*, 4685-4692.

(22) Sculimbrene, B. R., and Imperiali, B. *J. Am. Chem. Soc.* **2006**, Lanthanide-Binding Tags as Luminescent Probes for Studying Protein Interactions. *128*, 7346-7352.

(23) Heyduk, T. *Methods (San Diego, CA, United States)* **2001**, Luminescence resonance energy transfer analysis of RNA polymerase complexes. *25*, 44-53.

(24) Getz, E. B., Cooke, R., and Selvin, P. R. *Biophys. J.* **1998**, Luminescence resonance energy transfer measurements in myosin. *74*, 2451-2458.

(25) Selvin, P. R., and Hearst, J. E. *Proc. Natl. Acad. Sci. U. S. A.* **1994**, Luminescence energy transfer using a terbium chelate: improvements on fluorescence energy transfer. *91*, 10024-10028.

(26) Liu, Y., and Reineke, T. M. *Bioconjugate Chem.,***2007,** Poly(glycoamidoamine)s for Gene Delivery. Structural Effects on Cellular Internalization, Buffering Capacity, and Gene Expression. *18*, 19-30.

(27) Liu, Y., and Reineke, T. M. *J. Am. Chem. Soc*.,**2005,** Hydroxyl Stereochemistry and Amine Number within Poly(glycoamidoamine)s Affect Intracellular DNA Delivery. *127*, 3004-3015.

(28) Selvin, P. R., Rana, T. M., and Hearst, J. E., *J. Am. Chem. Soc.,* **1994** Luminescence Resonance Energy Transfer. *116*, 6029-6030.

Chapter 4 : Quantifying Free vs. Bound Polymer in Polyplex Formulations Using NMR*

*This work is a collaborative effort between dissertation author, Dr. Lou Madsen and Xiaoling (Cocoa) Wang at Virginia Tech. Cocoa performed NMR experiments, processed data and performed integral calculations. Dissertation author designed experiments, synthesized N4La polymer, characterized nanoparticles and polymers, and prepared samples for NMR.

Abstract:

In the field of non-viral gene delivery, accurate characterization of therapeutic formulations to determine composition of each species is crucial for FDA approval. Currently, there is no method to determine amount of free vs. bound polymer in a formulation without any synthetic modification (isotope or fluorescent labeling). Several reports highlight the importance of using higher N/P ratio (or presence of excess free polymer) to achieve high transfection efficiency in cells; however, presence of excess free polymer can cause *in vivo* toxicity in some cases.

We have developed an NMR method to quantify free vs. bound polymer by integrating broad resonances (from nanometer sized particles) with narrow peaks from free polymer chains. In this report, three polymer systems- polyethyleneimine (PEI, commercial transfection agent), G4 (sold as Glycofect™ transfection agent) and N4La (synthesized by step-growth polymerization) under investigation demonstrate increase in percentage of free polymer with increase in N/P ratio (ratio of protonable nitrogens on polymer to phosphates on DNA). This relative integration method (integrating broad and narrow resonances) is supported by an internal

reference method which we have developed to quantify amount of free polymer (from narrow resonances) with known internal reference concentration.

1. Introduction

The emerging field of non-viral polymeric vehicles holds promise to rapidly translate the bench side research of gene therapy into the clinics.[1-3] Polycationic vehicles used for gene delivery compact down large nucleic acids (DNA or siRNA) into nanoparticles.[4,5] This facilitates their uptake into the cell via endocytosis where it (nanoparticle) interacts with the cellular machinery to produce desired therapeutic effect.

The molar ratio of polymer to DNA denoted as N/P ratio (ratio of number of protonable nitrogens on the polymer to number of phosphate groups on DNA) plays important role in optimizing transfection efficiency. Several reports[6-8] have shown that transfection efficiency increases with increase in N/P ratio and presence of excess of polymer facilitates cellular uptake and transfection. Vuorimaa and coworkers[9] have illustrated using time-resolved spectroscopy that in case of branched and linear polyethyleneimine (PEI), presence of excess of free polymer significantly affects the cellular transfection. During their studies, they observed decrease in transfection upon removal of free polymer from the polyplex solution using size exclusion based purification. This effect was reversed upon addition of excess of free polymer.

Our group has developed carbohydrate-based cationic polymeric gene delivery vehicles, poly(glycoamidoamine)s (PGAAs), that contain oligoethyleneamine units (similar to PEI) with different carbohydrate moieties.[10-12] These polycation in most of the cases have better gene transfection efficiency and low cytotoxicity than commercial agent PEI.[12] Previous studies performed on PEI and poly(amidogalactaramine) G4 (commercialized as Glycofect™ by

Techulon Inc.) indicate that the free polymer can permeabilize nuclear membrane and plays important role in polyplex trafficking. [13,14]

Presence of excess of free polymer *in vivo* can raise toxicity concerns. So far, there is no method to reliably quantify this free polymer in a given formulation. This information can play important role for FDA approval process. In this report, we have developed a NMR method to quantify free vs. bound polymer in a polyplex dispersion. Relative amount of free vs. bound polymer was determined by comparing integrals of broad resonances from nano-sized (polymer-DNA complex) particles to that of narrow lines from free polymer chains. Polymers under investigation include a commercial transfection agents- PEI and G4 and newly synthesized non-paramagnetic (lanthanum, La) analogue of previously described[15] theranostic polymeric vehicle N4 La.

Dynamics of polyplexes or mechanism of DNA release are not commonly characterized with NMR.[16] Several reports exists for characterizing biomolecules such as proteins, nucleic acids[17] in-cell or cell free[18,19] environment using NMR, almost all of them are performed by using ^{15}N, ^{31}P or ^{2}D labeling to increase signal to noise ratio. NMR studies to study polyplex dynamics without any labeling has not been done before possibly due to high concentrations required that may lead to aggregation or precipitation. In our systems, for concentrations > 0.4 mg/mL we saw aggregation or cloudiness in the solution. For all of the studies in this report, we have maintained a low concentration (0.1-0.3 mg/mL) to mimic biological formulations and to avoid any precipitation.

2. Experimental

2.1. Materials:

25 kDa linear PEI was purchased from Alfa Aesar. Glycofect™ (G4, 5.6kDa) was obtained from Techulon Inc. and plasmid DNA (1.0 mg/mL, 7.5kbp, pcmv, lacz) was purchased from Aldevron. All the reagents were used without any further purification unless specified otherwise DNAse and RNAse free water used to make polyplexes was purchased from Gibco, Invitrogen (Carlsbad, CA). $LaCl_3 .7H_2O$ was purchased from Sigma Aldrich.

NMR solvents D_2O and 0.75 wt% solution of 3-(trimethylsilyl)propionic-2,2,3,3-d_4 acid, sodium salt in D_2O were purchased from Sigma Aldrich. Tris buffer used to formulate PEI polyplexes was purchased from Fisher Scientific.

2.2. Methods:

2.2.1. Synthesis of N4La polymer:

N4 La polymer was synthesized *via* step-growth polymerization of Boc-protected pentaethylenehexamine with diethylenetriamine pentaacetic acid bisanhydride (DTPA-BA) in dry DMSO as described in Chapter 2. After the polymerization, the polymer was made water-soluble by deprotection of Boc groups using trifluoroacetic acid, followed by chelation with $LaCl_3$ in equivalent molar ratio. Dialysis was performed (3500 MWCO dialysis bags) in pure water after each step during synthesis, to remove any low molecular weight oligomers/excess monomers and excess of $LaCl_3$. Pure polymer was obtained after freeze-drying of the dialyzed solution to yield white fluffy polymer.

2.2.2. SEC characterization of polymers:

The average molecular weights of PEI and N4La was determined using SEC. SEC was performed in aqueous mobile phase- 0.45 M sodium acetate in water with 20v% Acetonitrile, pH 7 (for N4La) or pH 5 (for PEI) (adjusted using acetic acid), flow rate 0.6 mL/min. Polymer dissolved in mobile phase was separated using $GMPW_{xL}$ and $G2500PW_{xL}$ (Tosoh Bioscience) columns. This system was equipped with- Waters 2489 UV/vis detector (l ¼ 274 nm), Wyatt Optilab rex refractometer (l ¼ 658 nm), and Wyatt DAWN Heleos-II multiangle laser light scattering (MALLS) detector (l ¼ 662 nm). The data were recorded and analyzed using ASTRA (version 5.3) software.

2.2.3. General procedure for formulation of polyplexes:

All the polyplexes except PEI were formulated in nuclease-free water. For formation of polyplexes, solvents were chosen based on best method to simulate the ideal transfection conditions and to avoid any aggregation. In case of PEI, similar sized polyplexes were formed in tris buffer (10 mM, pH 7). However, in case of G4 and N4La, water was found to be suitable than tris buffer due to significantly larger polyplexes in tris buffer. NMR studies were performed in pure water for G4 and N4 La and in 10 mM, pH 7 tris buffer for PEI.

Polyplexes were formulated by mixing equal volumes (200 µL) of polymer and pDNA at 37°C to achieve required N/P ratios. Polyplexes were prepared at different N/Ps, with different total concentrations (table 1) and compared with polymer solutions.

Table 4-1: Formulation concentrations for different polymer systems at different N/P ratios studied.

Polymer, N/P	Concentration of Polymer, mg/mL	Concentration of pDNA mg/mL	Total concentration, mg/mL
PEI	0.173	0	0.173
PEI @ N/P 5	0.173	0.265	0.438
PEI@ N/P 10	0.173	0.135	0.308
PEI@ N/P 20	0.173	0.066	0.239
PEI@N/P 120	0.173	0.011	0.184
N4 La	0.367	0	0.366
N4La@N/P 10	0.184	0.033	0.216
N4La@ N/P 40	0.367	0.016	0.383
G4	0.173	0	0.173
G4@N/P 5	0.173	0.113	0.286
G4 @N/P 10	0.173	0.056	0.229
G4@ N/P 20	0.173	0.028	0.201

2.2.4. Gel shift assay to determine pDNA binding ratio:

DNA binding ability of PEI and N4La was studied using gel electrophoresis shift assay. Agarose gel (0.6 w/v %) containing ethidium bromide (0.06 w/v %) was prepared in Tris-acetate EDTA (TAE) buffer (40 mM Tris-acetate, 1 mM EDTA, pH 8). Polyplexes were formulated at N/P ratios (N= number of amines long polymer backbone and p= number of phosphate units on DNA)- 0, 2.5, 5, 10, 20, 30, 40 and 50 by mixing equal volumes (10 µL each) of polymer and

pDNA (0.1 µg/µL, pcmv lacZ). After formulation, polyplexes were incubated at room temperature for 30 min before addition of 2 µL of gel loading buffer (Blue juice, Invitrogen, Carlsbad, CA). 10 µL of each N/P formulation was loaded into a well and electrophoretic field (65 V, 60 min) was applied to study the inhibition of DNA migration toward anode in presence of polymer. The gel was visualized using UV light and digital camera.

2.2.5. ^{1}H NMR of polyplexes

Polyplexes were formulated as described above by mixing equal volumes (200µL each) of polymer and DNA. Next, 0.05 mL (10% of total volume) of D_2O containing 0.75 wt% solution of 3-(trimethylsilyl)propionic-2,2,3,3-d_4 acid, sodium salt was added to this solution. All NMR experiments were performed on a Bruker Avance spectrometer operating at 600 MHz for ^{1}H equipped with a 5-mm triple resonance broad band probe. The radio-frequency pulse sequence used is based on presaturation solvent suppression. A continuous wave irradiation of 8 mW was applied on H_2O resonance at around 4.7 ppm for 200 ms during the pre-scan delay, followed by a ^{1}H 90 degree transmitter pulse. The pre-scan delay and acquisition time were set to 13.5 s and 2.5 s, respectively. All experiments were performed at 310 K with 512 scans. Postacquisition processing included 0.3 Hz line broadening and Fourier transformation.

2.2.6. Quantification of free vs. bound polymer in polyplexes:

Percentage of free polymer was determined by comparing integrals of broad vs. sharp resonances in 1D spectrum (Equation 1). This integration method was accompanied with internal reference method where, a known amount of above mentioned internal reference (water soluble TMS) was added to quantify moles of free polymer.

$$\%\ free\ polymer = \frac{Integration\ of\ free\ polymer\ resonances\ around\ 3ppm}{Integration\ of\ free\ polymer\ resonances + broad\ resonances} \times 100 \ldots\ldots\ldots (1)$$

where, integration of broad resonances (I_B)

$$I_B = total\ integration\ (\pm 50\ ppm) - H_2O\ proton\ integration - sum\ of\ all\ sharp\ peaks\ integration$$

3. Results

3.1. Synthesis and characterization of polymers:

N4La polymer was synthesized in high yield and purity using step-growth polymerization. SEC characterization performed on N4 La and PEI (Figure 4-1 and Table 2) showed relatively narrow molecular weight distributions (<1.2 PDI) (due to extensive dialysis in case of N4La). PEI and N4La had molecular weights of 26.2 and 18.0 kg/mol respectively whereas, Glycofect ™ purchased from Techulon Inc. had Mw of 5.6 g/mol (DP =12).

(a) (b)

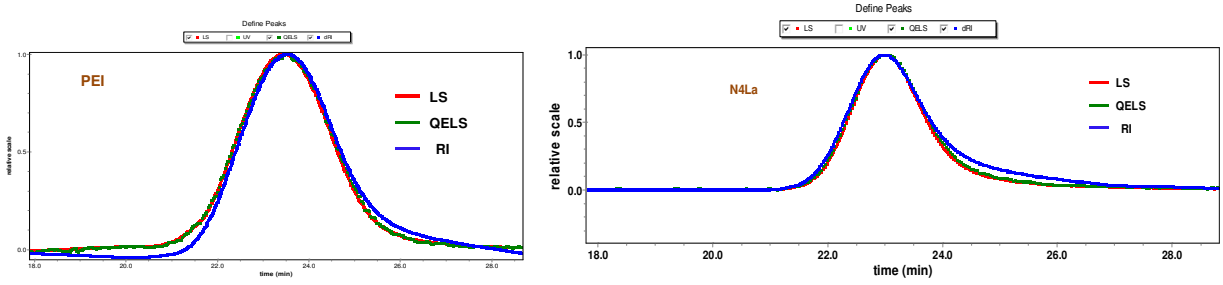

Figure 4-1: Overlay of light scattering (red), refractive index (blue) and QELS (green) traces for PEI (a) and N4La (b) polymers.

Table 4-2: SEC analysis of N4La G4 and PEI to determine weight average (Mw), number average (Mn) molecular weights and polydispersity of the polymers.

	N4La	PEI	G4
Mw (kg/mol)	18.0	26.2	5.6
Mn (kg/mol)	17.1	25.3	-
Mw/Mn	1.1	1.04	-
DP	23	609	11

3.2. Characterization of polyplexes using gel shift assay and DLS:

Before running any NMR studies, polymers and polyplexes were analyzed with gel shift assay and dynamic light scattering to study their DNA binding and compaction properties. Gel binding assay was performed on PEI and N4La at different N/P ratios (Figure 4-2) to indentify the ratio at which migration of DNA to anode is inhibited. In case of PEI, at N/P ratio 2.5, complete binding was observed, however, in case of N4La, it was around N/P 5 or higher. N4La was not able to compact DNA as efficiently as PEI, indicated by presence of secondary band indicative of unbound DNA. Gel electrophoresis data for G4 published by our group in several publications[11,12] was used as a reference to select N/P ratios for NMR studies.

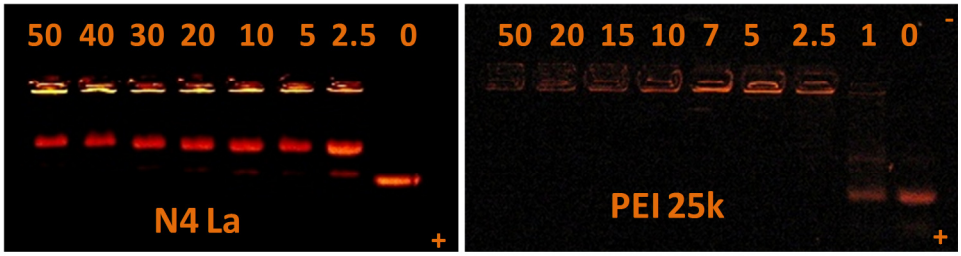

Figure 4-2: Gel electrophoresis shift assay performed on N4La and PEI at different N/P ratios to determine optimum binding ratio.

Dynamic light scattering was performed at same concentrations used for NMR experiments. G4 and N4 La polymer aggregate up to size of 100-1000nm in water (Figure 4-3 and 4-5), however, PEI chains stayed as 'unimers' in tris buffer (Figure 4-4). PEI polyplexes

exhibited particle size from 80 nm to 170 nm with decrease in N/P ratio from 120 to 5. G4 polyplex size varied between 80-90 nm and a small fraction of ~200 nm sized particles was also observed. N4La polyplexes changed from 60 to 90 nm with decrease in N/P ratio from 40 to 10.

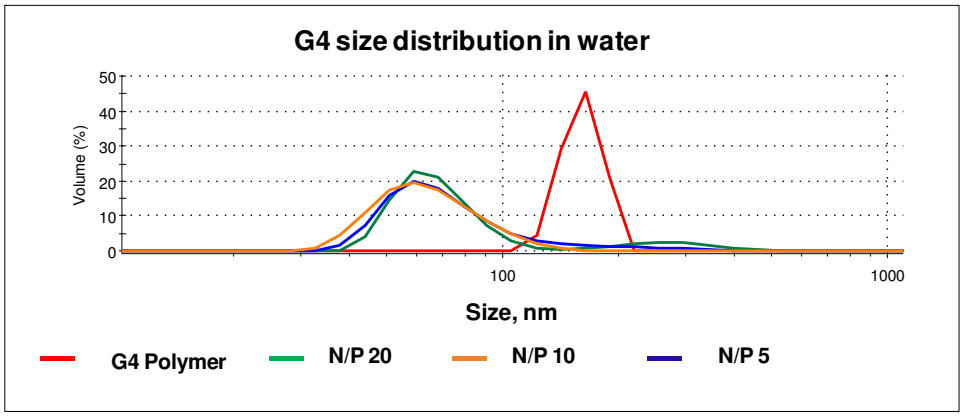

Figure 4-3: Size measurements for G4 polymer (red) and its complexes with pDNA at N/P ratios: 20 (green), 10 (orange) and 5 (purple) in water were performed using DLS.

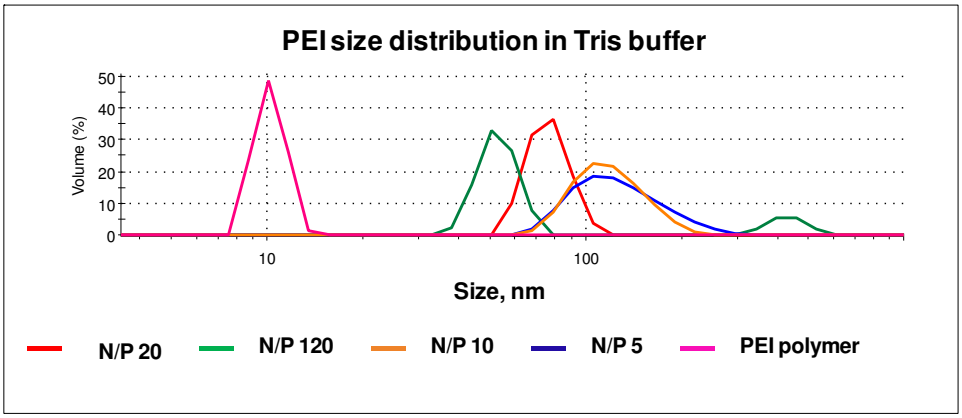

Figure 4-4: Size measurements for PEI polymer (pink) and its complexes with pDNA at N/P ratios: 120 (green), 20 (red), 10 (orange and 5 (purple) in tris buffer were performed using DLS.

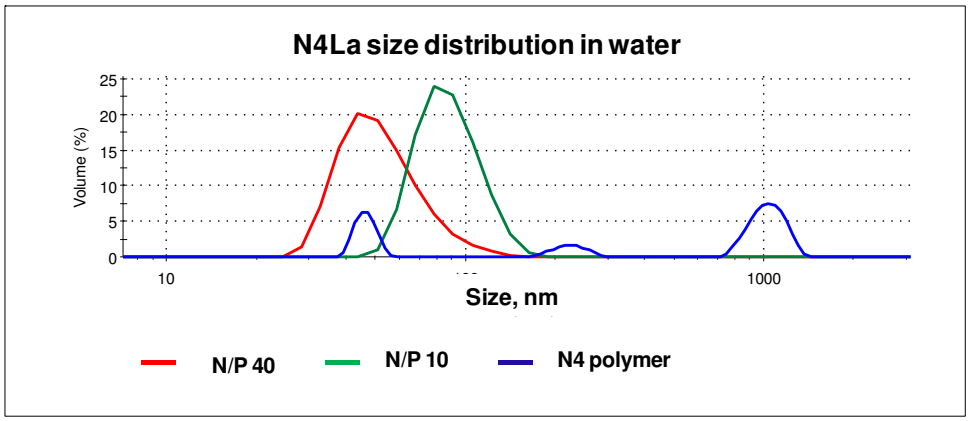

Figure 4-5: Size measurements for N4La polymer (purple) and its complexes with pDNA at N/P ratios: 40 (red) and 10 (green) in water were performed using DLS.

3.3. ^{1}H characterization of polyplexes and quantifying free vs. bound amount of polymer:

Polymer and polyplexes at different N/Ps were analyzed using ^{1}H NMR to determine amount of free polymer in a solution. Two methods- relative integration method (comparing integral of free polymer to total integration) and internal reference method (quantifying amount of free polymer from known quantity of TMS standard) were compared for PEI, G4 and N4 polymer systems. PEI polymer in tris buffer showed no broad peak and the entire polymer was present in a form of free polymer chains with no aggregation. With increase in N/P ratio (from 10 to 120) amount of free polymer increased from 16% to 27% (Figure 4-7 and 4-9) for relative integration method and from 15% to 26% for internal reference method.

G4 showed aggregation in pure water, with only 35% of free polymer present in a solution (Figure 4-9). With relative integration method, increase in N/P ratio (from 5 to 20) of G4 polyplexes changed percentage free polymer (Figure 4-8 and 4-9) from 17% to 35%. With internal reference method, it varied from 20-38%. Both the methods agree well and follow a common trend of increase in amount of free polymer with N/P ratio.

N4 polymer aggregates in water and according to relative integration method, it has about 36% of free polymer in a solution (Figure 4-6). With N4 polyplexes, increase in N/P ratio from 10 to 40 amount of free polymer increases from 26% to 30% measured by relative integration method. However, there is a difference in amount of free polymer calculated with internal reference method at N/P 40. We think this might be due to less than 100% lanthanum loading per repeat unit, this is under investigation.

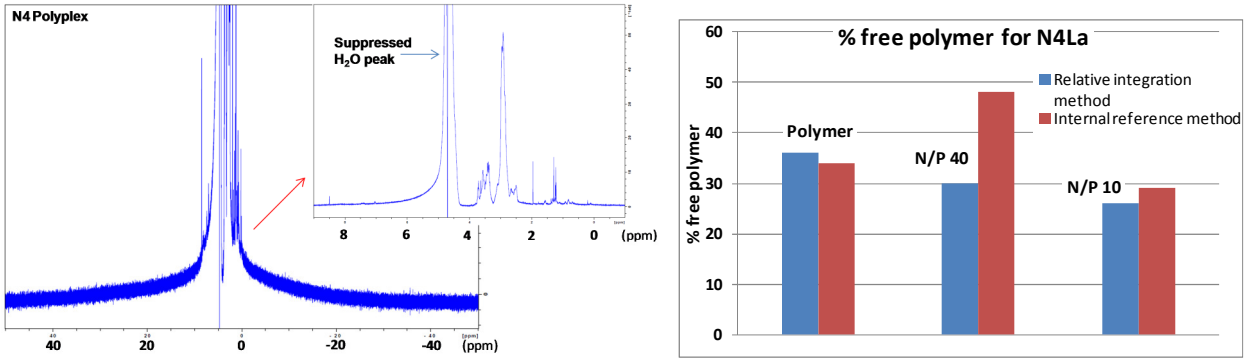

Figure 4-6: ^{1}H spectrum of N4 polyplex (left) shows presence of broad signal from nanometer sized particles and narrow peaks from smaller sized (<10 nm) polymer particles. Percentage of free polymer was calculated (right) using relative integration (blue bars) and internal reference method (red bars) for N4La polymer and polyplexes at N/P 40 and 10.

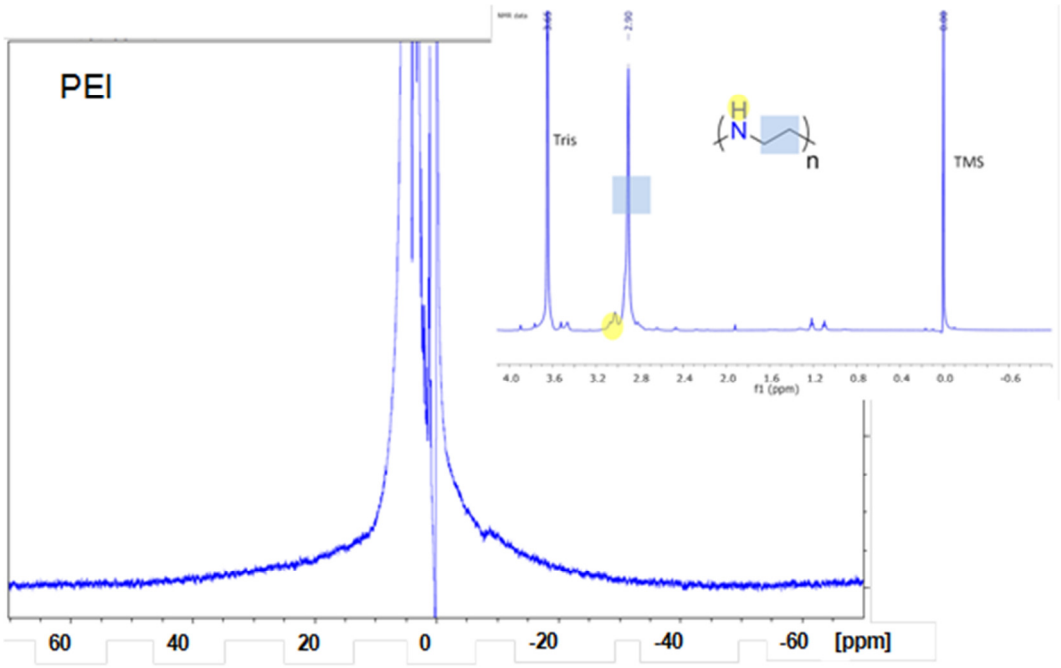

Figure 4-7: ^{1}H spectrum of PEI polyplexes at N/P 10 (in 10 mM tris buffer pH 7) indicating presence of broad and sharp peaks which can be attributed to polyplex and polymer particles respectively.

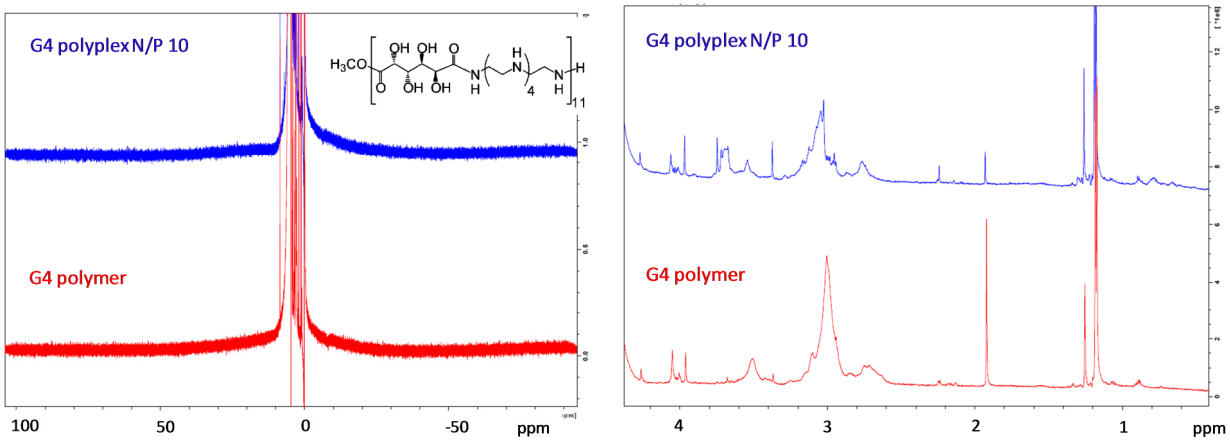

Figure 4-8: Comparing broad (left) and sharp (right) resonances in ^{1}H spectrum of G4 polymer and polyplexes at N/P 10 in water.

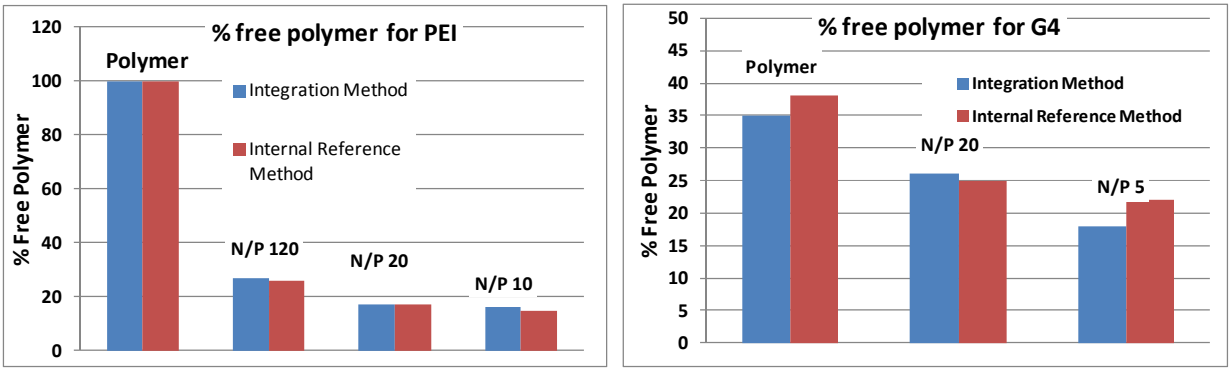

Figure 4-9: The percentage of free polymer in PEI (left) and G4 (right) polyplexes was determined using relative integration (blue bars) and internal reference (red bars) methods.

4. Discussion

Several reports in the field of gene delivery have demonstrated that the presence of excess of polymer plays important role in increasing transfection efficiency.[6-8] There are few studies performed to characterize polyplexes with the help of light scattering or fluorescence spectroscopy to determine the amount of polymer/DNA molecules per polyplex particle and to calculate amount of free polymer in the solution. [9,20,21]This is a first report to determine amount of free vs. bound polymer in a polyplex solution using NMR spectroscopy. We have used NMR integration to compare nanoparticles (polyplexes, free DNA and aggregated polymer) with free polymer chains in the solution.

Our studies with particle size of polyplexes of PEI in water and tris buffer using DLS were comparable, which lead us to perform all the studies in tris buffer. G4 polyplexes showed enhanced particle size and poor stability in tris buffer compared to water. This can be attributed to tendency to G4 to undergo faster degradation at higher pH.[22] Our studies for G4 performed in water showed a trend of increase in amount of free polymer with N/P ratio. For N4 polymer, overall increase in free polymer content with N/P ratio was observed with relative integration

method. However, there was slight variation in two methods in case of N/P 40. We think one of the possible reasons for the discrepancy can be due to less than 100% loading of lanthanide per polymer chain. Additionally, weak binding between polymer-DNA in case of N4 makes polyplex suspension more complex and polydisperse system comprising of polymer aggregates, free DNA and polymer-DNA complexes. Our current efforts are directed toward understanding this further.

Overall, we have developed a reliable NMR method to quantify free vs. bound polymer in polyplex formulation. This method is promising and enables us to characterize any gene delivery formulation in any solvent system.

5. Acknowledgements

Authors would like to thank NSF for funding of this project and Techulon Inc. for generous donation of Glycofect™. Dissertation author would like to thank Prof. Richey Davis (DLS) and Prof. Webster Santos (Gel Box) for instrument usage.

References

(1) Samal, S. K.; Dash, M.; Van Vlierberghe, S.; Kaplan, D. L.; Chiellini, E.; van Blitterswijk, C.; Moroni, L.; Dubruel, P. *Chem. Soc. Rev.* **2012**, Cationic polymers and their therapeutic potential, *41*, 7147-7194.

(2) Pack, D. W.; Hoffman, A. S.; Pun, S.; Stayton, P. S. *Nat. Rev. Drug Discovery* **2005**, Design and development of polymers for gene delivery, *4*, 581-593.

(3) Mintzer, M. A.; Simanek, E. E. *Chem. Rev.* **2009**, Nonviral Vectors for Gene Delivery, *109*, 259-302.

(4) Eickbush, T. H.; Moudrianakis, E. N. *Cell (Cambridge, MA, United States)* **1978**, The compaction of DNA helices into either continuous supercoils or folded-fiber rods and toroids, *13*, 295-306.

(5) Yue, Y.; Jin, F.; Deng, R.; Cai, J.; Chen, Y.; Lin, M. C. M.; Kung, H.-F.; Wu, C. *J. Controlled Release* **2011**, Revisit complexation between DNA and polyethylenimine - Effect of uncomplexed chains free in the solution mixture on gene transfection, *155*, 67-76.

(6) Brissault, B.; Kichler, A.; Guis, C.; Leborgne, C.; Danos, O.; Cheradame, H. *Bioconjugate Chem.* **2003**, Synthesis of linear polyethylenimine derivatives for DNA transfection, *14*, 581-587.

(7) Clamme, J. P.; Azoulay, J.; Mely, Y. *Biophys. J.* **2003**, Monitoring of the formation and dissociation of polyethylenimine/DNA complexes by two photon fluorescence correlation spectroscopy, *84*, 1960-1968.

(8) Kunath, K.; von Harpe, A.; Fischer, D.; Petersen, H.; Bickel, U.; Voigt, K.; Kissel, T. *J. Controlled Release* **2003**, Low-molecular-weight polyethylenimine as a nonviral vector for DNA

delivery: comparison of physicochemical properties, transfection efficiency and in vivo distribution with high-molecular-weight polyethylenimine, *89*, 113-125.

(9) Ketola, T.-M.; Hanzlikova, M.; Urtti, A.; Lemmetyinen, H.; Yliperttula, M.; Vuorimaa, E. *J. Phys. Chem. B* **2011**, Role of Polyplex Intermediate Species on Gene Transfer Efficiency: Polyethylenimine-DNA Complexes and Time-Resolved Fluorescence Spectroscopy, *115*, 1895-1902.

(10) Ingle, N., P.; Malone, B.; Reineke Theresa, M. *Trends Biotechnol.* **2011**, Poly(glycoamidoamine)s: a broad class of carbohydrate-containing polycations for nucleic acid delivery, *29*, 443-53.

(11) Liu, Y.; Reineke, T. M. *J. Am. Chem. Soc.* **2005**, Hydroxyl Stereochemistry and Amine Number within Poly(glycoamidoamine)s Affect Intracellular DNA Delivery, *127*, 3004-3015.

(12) Liu, Y.; Reineke, T. M. *Bioconjugate Chem.* **2007**, Poly(glycoamidoamine)s for Gene Delivery. Structural Effects on Cellular Internalization, Buffering Capacity, and Gene Expression, *18*, 19-30.

(13) Grandinetti, G.; Reineke, T. M. *Molecular Pharmaceutics* **2012**, Exploring the Mechanism of Plasmid DNA Nuclear Internalization with Polymer-Based Vehicles, *9*, 2256-2267.

(14) McLendon, P. M.; Fichter, K. M.; Reineke, T. M. *Molecular Pharmaceutics* **2010**, Poly(glycoamidoamine) Vehicles Promote pDNA Uptake through Multiple Routes and Efficient Gene Expression via Caveolae-Mediated Endocytosis, *7*, 738-750.

(15) Bryson, J. M.; Fichter, K. M.; Chu, W.-J.; Lee, J.-H.; Li, J.; Madsen, L. A.; McLendon, P. M.; Reineke, T. M. *Proc. Natl. Acad. Sci. U. S. A.* **2009**, Polymer beacons for luminescence and magnetic resonance imaging of DNA delivery, *106*, 16913-16918.

(16) Prevette, L. E.; Nikolova, E. N.; Al-Hashimi, H. M.; Banaszak Holl, M. M. *Molecular Pharmaceutics* **2012**, Intrinsic dynamics of DNA-polymer complexes: A mechanism for DNA release, *9*, 2743-2749.

(17) Feigon, J.; Sklenar, V.; Wang, E.; Gilbert, D. E.; Macaya, R. F.; Schultze, P. *Methods Enzymol* **1992**, 1H NMR spectroscopy of DNA, *211*, 235-53.

(18) Reckel, S.; Loehr, F.; Doetsch, V. *ChemBioChem* **2005**, In-cell NMR spectroscopy, *6*, 1601-1606.

(19) Huang, Z.; Tong, Y.; Wang, J.; Huang, Y. *Cancer Cell International* **2003**, NMR studies of the relationship between the changes of membrane lipids and the cisplatin-resistance of A549/DDP cells, *3*, No pp given.

(20) Lai, E.; Van Zanten, J. H. *Biophys. J.* **2001**, Monitoring DNA/poly-L-lysine polyplex formation with time-resolved multiangle laser light scattering, *80*, 864-873.

(21) Choosakoonkriang, S.; Lobo, B. A.; Koe, G. S.; Koe, J. G.; Middaugh, C. R. *J. Pharm. Sci.* **2003**, Biophysical characterization of PEI/DNA complexes, *92*, 1710-1722.

(22) Liu, Y.; Reineke, T. M. *Biomacromolecules* **2010**, Degradation of Poly(glycoamidoamine) DNA Delivery Vehicles: Polyamide Hydrolysis at Physiological Conditions Promotes DNA Release, *11*, 316-325.

Chapter 5 : Suggested Future Work

Lanthanide containing polymers studied in this dissertation are promising for the field of multifunctional 'theranostic' nanoparticles. We have shown that by switching the lanthanide metal chelated along the polymer backbone between gadolinium, terbium and lanthanum, functionality of these materials can be diversified from MR imaging agents and fluorescent markers to non-paramagnetic polymers. In this chapter, I propose some of the future directions that can be pursued to expand potential of these polymer systems even further.

1. *In vivo* studies and combination therapy:

Based on the results discussed in Chapter 2, I think the lanthanide polymers are promising to test for in vivo pDNA delivery. In addition to delivery formulations described in chapter 2, different formulations to achieve optimum performance and multifunctionality can be explored. For example, mixing of Gd and Tb labeled polymers or labeling same polymer with more than one lanthanide (Gd/Tb) can enable incorporation of MRI and luminescent agent functionality into one package. Title polymers can also be end-functionalized with suitable ligands such as small molecules, vitamins, antibodies, and proteins[1] for targeted delivery *in vivo*.

Chelation of polymers with radioactive isotopes of lanthanides such as ^{90}Y, ^{153}Sm or ^{177}Lu for radiation therapy[2] through same chelation chemistry would open up new dimension of cancer therapy (radiation therapy) and imaging (nuclear imaging). This can be done by modification only at the final step (chelation of lanthanides) during polymer synthesis as described in chapter 2. Combining different therapies (nucleic acid and radiation therapies) would cause significantly higher treatment efficiency.[3]

Employing combination therapy with these polymers would require lot of formulation work to achieve perfect balance between optimum/efficient therapeutic/diagnostic dosage and threshold to avoid any toxicity. Nevertheless, these materials definitely offer a promise to diversify mode of cancer therapy, by simple synthetic modification.

2. LRET monitoring *in cellulo*:

Based on studies performed in Chapter 3, I propose that Tb polymers can further be tested in cells to monitor vehicle unpackaging. Studies can be performed on cells transfected with 'LRET-paired' polyplexes (Tb polymer-TMR DNA) at different time points (0, 15min, 30min, 1h, 4h, 12h and 24h)[4] to monitor change in emission intensity of Tb and TMR. Increase in emission intensity of Tb polymer with time after transfection, would indicate onset of polyplex dissociation. This study will elucidate information on kinetics of polyplex trafficking and DNA release in cells. Additionally, different fluorophores such as fluoresceine and Alexa® dyes that can form bi-FRET system[5] with Tb can be used to label cell organelles to further understand mechanism of intracellular trafficking and location of polymer after pDNA delivery.

3. Studying polyplex diffusion in biological media and cells:

NMR method described in Chapter 4 to quantify amount of free polymer in a polyplex formulation can be extended to any type of polymer in a suitable medium. Several reports[6-8] have indicated that presence of excess of free polymer helps to improve transfection efficiency; however, excess polymer can aggregate with itself to cause severe toxicity *in vivo*. Next step for this project would be to quantify amount of free polymer and determine diffusion coefficient of these polyplexes in biological media with or without serum (OptiMEM, DMEM) and in cells. This will simulate conditions in cells and demonstrate difference in behavior between formulation vial and real transfection conditions. Understanding diffusion of polyplexes in

biological media or in cells would be helpful to understand kinetics of polyplex trafficking and can potentially be correlated to results from cellular microscopy with luminescent analogues. To perform NMR studies in cells, suitable nuclear labeling (^{15}N, or ^{31}P) of nucleic acid and/or polymers will be required to simplify NMR spectrum and increase signal to noise ratio for the peaks of interest.

References:

(1) Byrne, J. D.; Betancourt, T.; Brannon-Peppas, L. *Adv. Drug Delivery Rev.* **2008**, Active targeting schemes for nanoparticle systems in cancer therapeutics, *60*, 1615-1626.

(2) Liu, S. *Chem. Soc. Rev.* **2004**, The role of coordination chemistry in the development of target-specific radiopharmaceuticals, *33*, 445-461.

(3) Greco, F.; Vicent, M. J. *Adv. Drug Delivery Rev.* **2009**, Combination therapy: Opportunities and challenges for polymer-drug conjugates as anticancer nanomedicines, *61*, 1203-1213.

(4) Chen, H. H.; Ho, Y.-P.; Jiang, X.; Mao, H.-Q.; Wang, T.-H.; Leong, K. W. *Molecular Therapy* **2008**, Quantitative Comparison of Intracellular Unpacking Kinetics of Polyplexes by a Model Constructed From Quantum Dot-FRET, *16*, 324-332.

(5) Kim, S. H.; Gunther, J. R.; Katzenellenbogen, J. A. *J. Am. Chem. Soc.* **2010**, Monitoring a Coordinated Exchange Process in a Four-Component Biological Interaction System: Development of a Time-Resolved Terbium-Based One-Donor/Three-Acceptor Multicolor FRET System, *132*, 4685-4692.

(6) Brissault, B.; Kichler, A.; Guis, C.; Leborgne, C.; Danos, O.; Cheradame, H. *Bioconjugate Chem.* **2003**, Synthesis of linear polyethylenimine derivatives for DNA transfection, *14*, 581-587.

(7) Clamme, J. P.; Azoulay, J.; Mely, Y. *Biophys. J.* **2003**, Monitoring of the formation and dissociation of polyethylenimine/DNA complexes by two photon fluorescence correlation spectroscopy, *84*, 1960-1968.

(8) Kunath, K.; von Harpe, A.; Fischer, D.; Petersen, H.; Bickel, U.; Voigt, K.; Kissel, T. *J. Controlled Release* **2003**, Low-molecular-weight polyethylenimine as a nonviral vector for DNA delivery: comparison of physicochemical properties, transfection efficiency and in vivo distribution with high-molecular-weight polyethylenimine, *89*, 113-125.

Appendix A: Important ^{1}H NMR Spectra

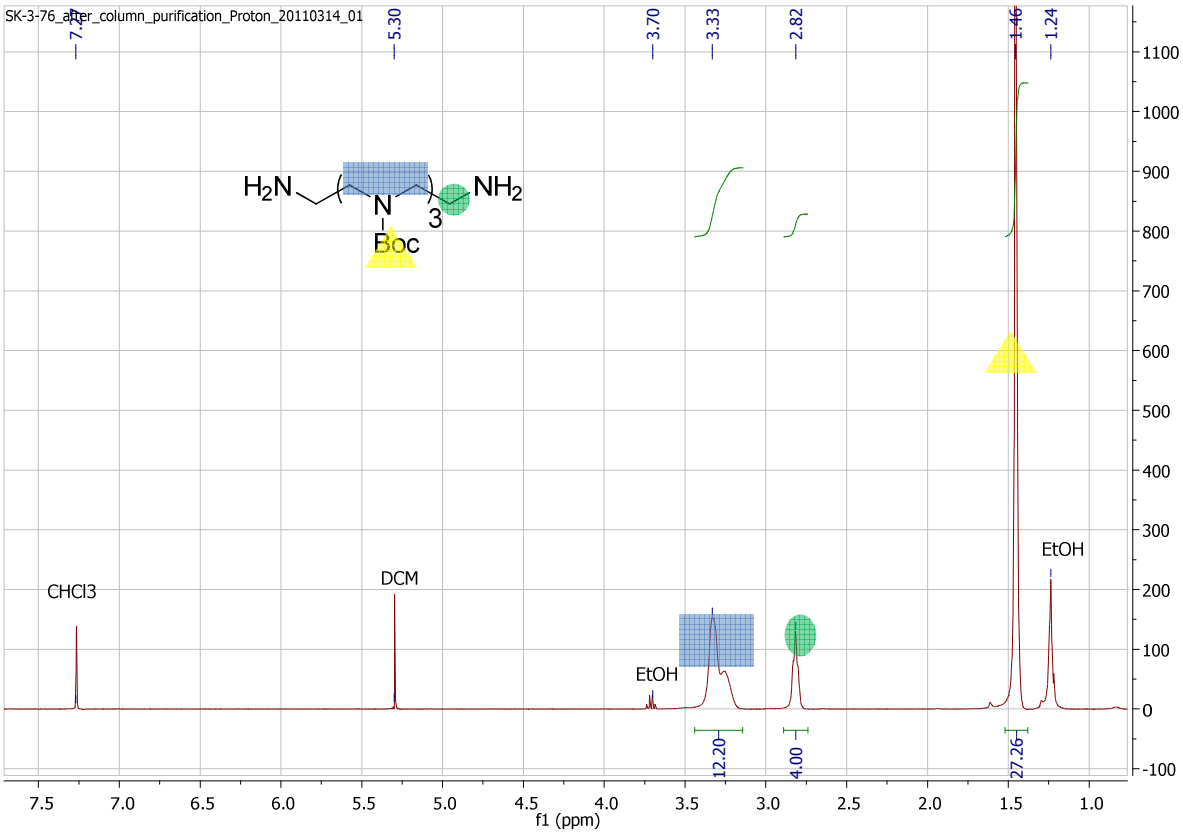
SK-3-76_after_column_purification_Proton_20110314_01
7.27
5.30
3.70
3.33
2.82
1.46
1.24
CHCl3
DCM
EtOH
EtOH
12.20
4.00
27.26
f1 (ppm)

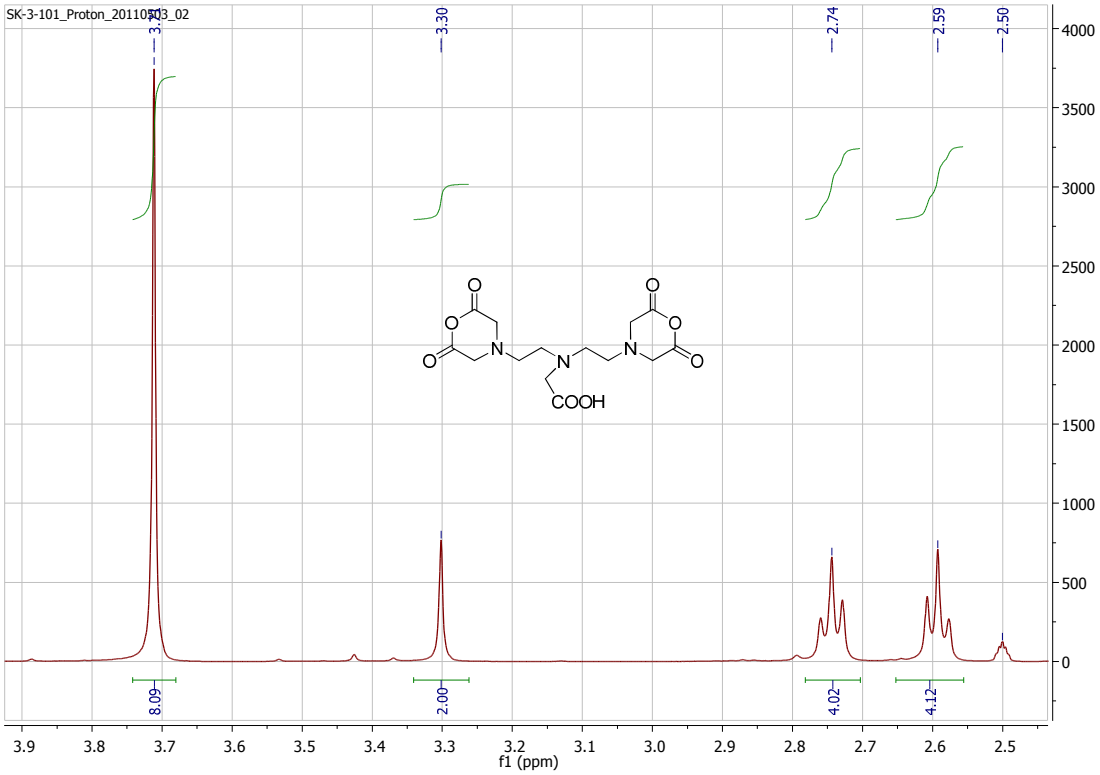
SK-3-101_Proton_20110503_02
3.71
3.30
2.74
2.59
2.50
COOH
8.09
2.00
4.02
4.12
f1 (ppm)

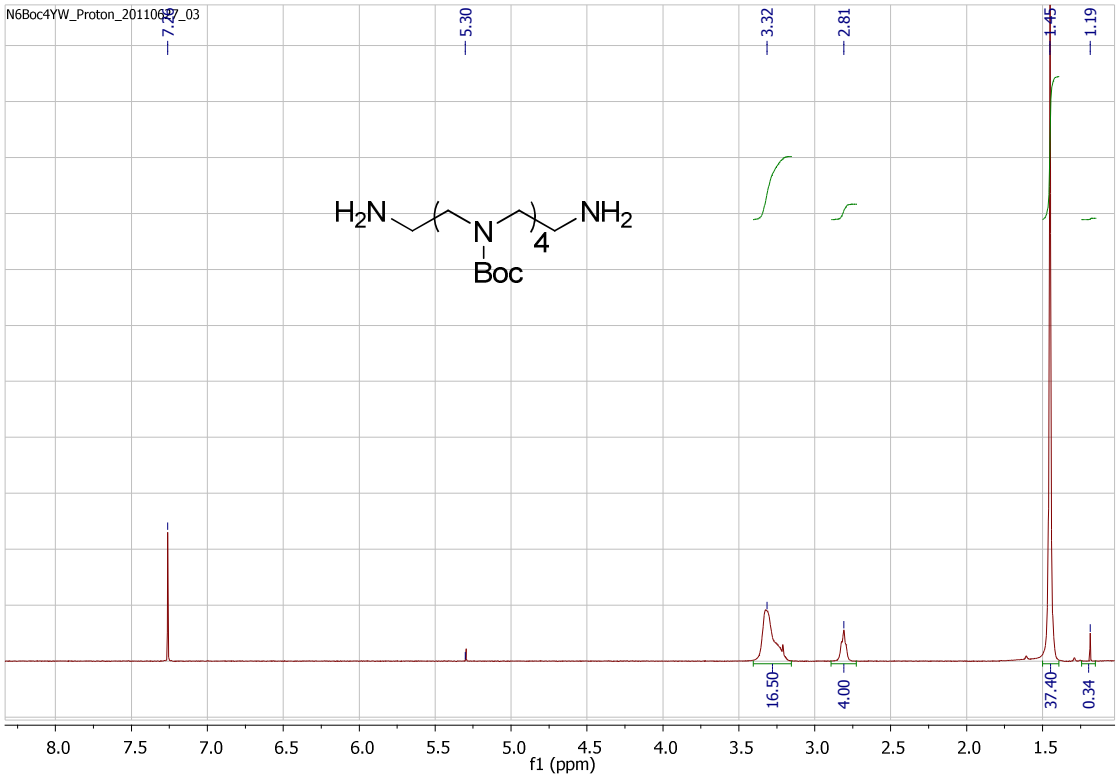
N6Boc4YW_Proton_20110407_03
7.27
5.30
3.32
2.81
1.45
1.19
H2N
NH2
N
4
Boc
16.50
4.00
37.40
0.34
8.0
7.5
7.0
6.5
6.0
5.5
5.0
4.5
4.0
3.5
3.0
2.5
2.0
1.5
f1 (ppm)

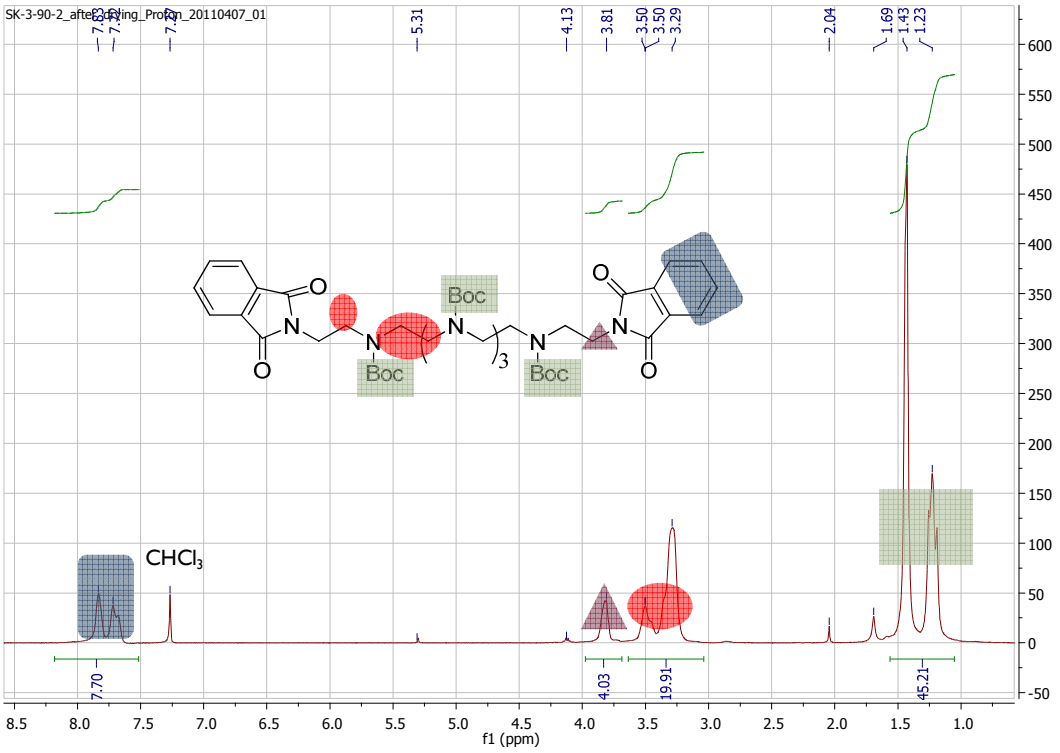
SK-3-90-2_after_Oxing_Proton_20110407_01
7.70
5.31
4.13
3.81
3.50
3.50
3.29
2.04
1.69
1.43
1.23
Boc
Boc
Boc
3
CHCl3
7.70
4.03
19.91
45.21
8.5
8.0
7.5
7.0
6.5
6.0
5.5
5.0
4.5
4.0
3.5
3.0
2.5
2.0
1.5
1.0
f1 (ppm)

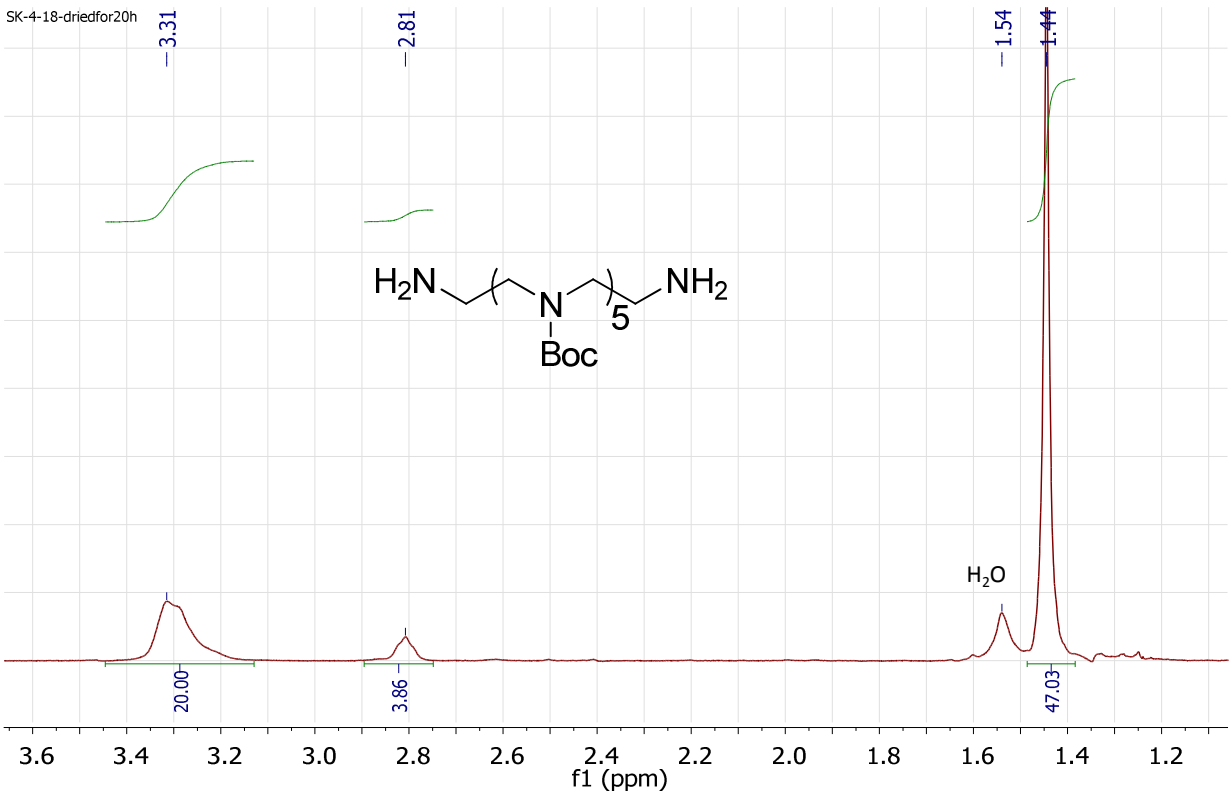
SK-4-18-driedfor20h
3.31
2.81
1.54
1.44
H2N
NH2
N
5
Boc
H2O
20.00
3.86
47.03
3.6
3.4
3.2
3.0
2.8
2.6
2.4
2.2
2.0
1.8
1.6
1.4
1.2
f1 (ppm)

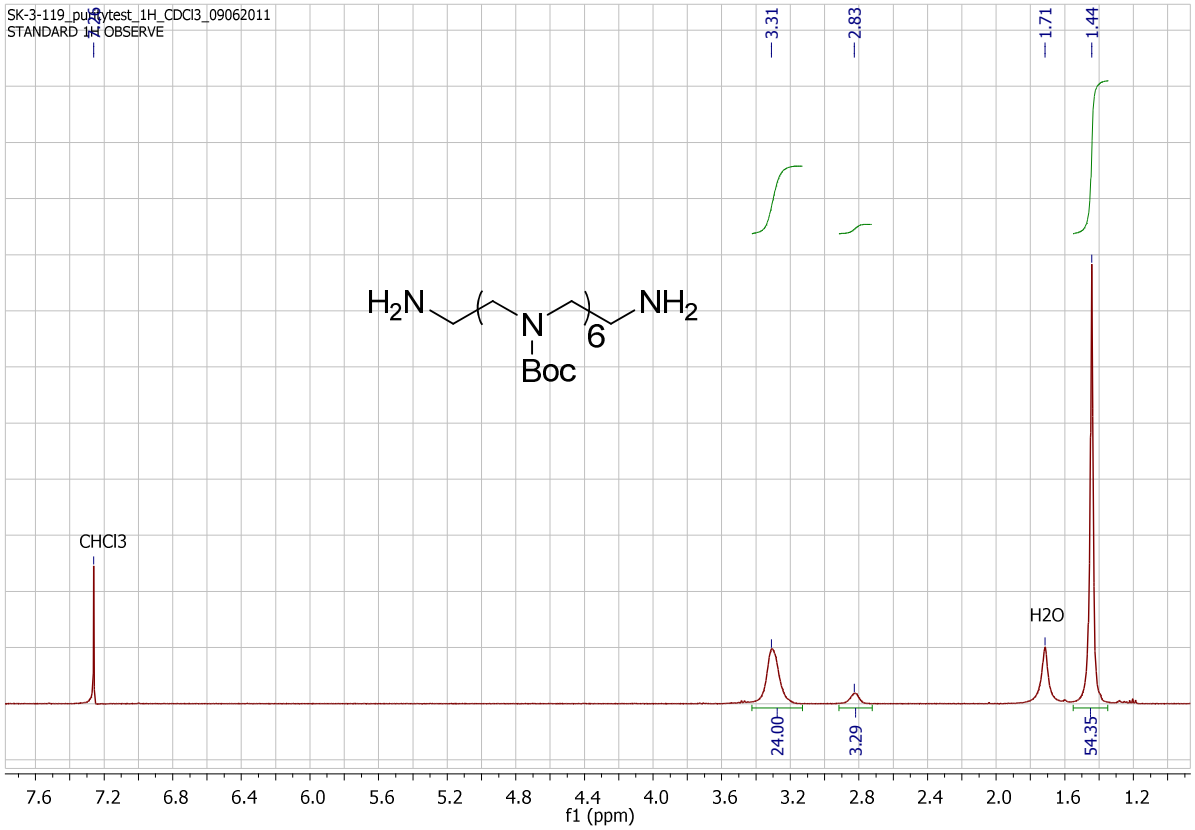
SK-3-119_purytest_1H_CDCl3_09062011
STANDARD 1H OBSERVE
3.31
2.83
1.71
1.44
H2N
NH2
N
6
Boc
CHCl3
H2O
24.00
3.29
54.35
7.6
7.2
6.8
6.4
6.0
5.6
5.2
4.8
4.4
4.0
3.6
3.2
2.8
2.4
2.0
1.6
1.2
f1 (ppm)

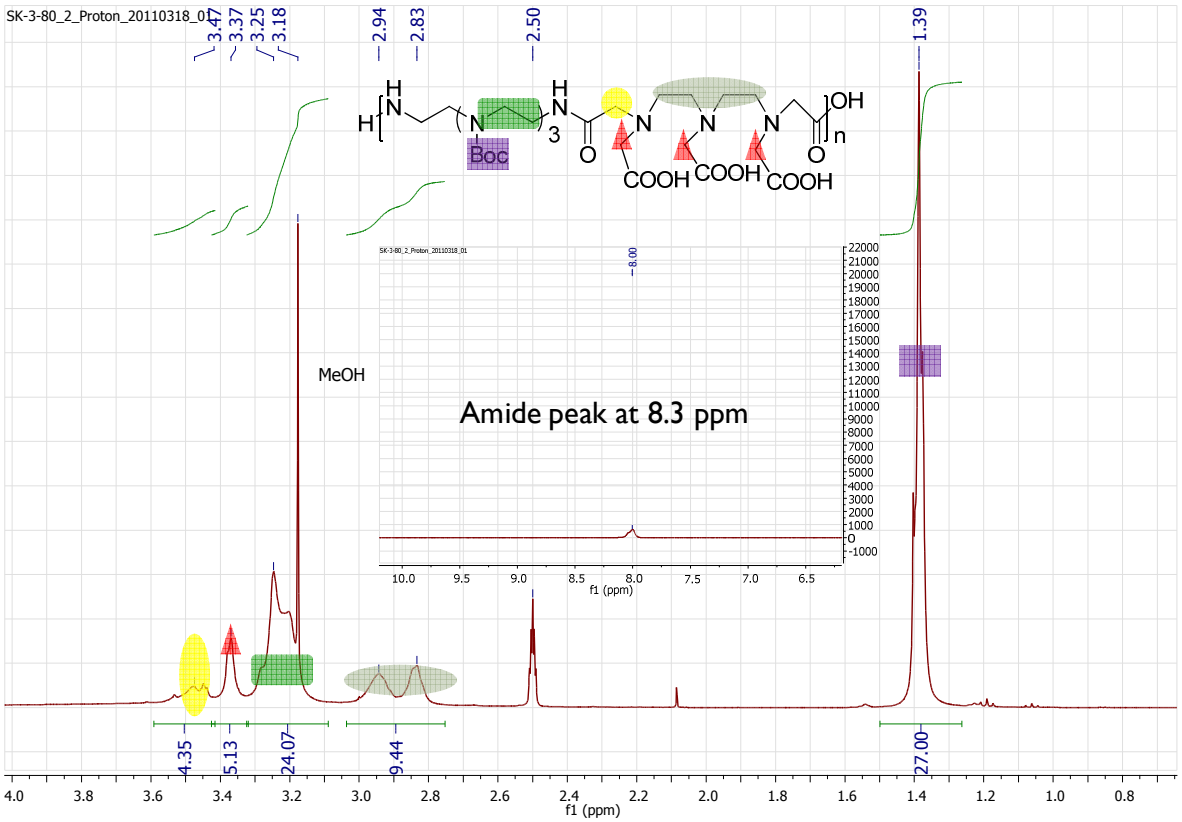
SK-3-80_2_Proton_20110318_01
3.47
3.37
3.25
3.18
2.94
2.83
2.50
1.39
MeOH
Amide peak at 8.3 ppm
4.35
5.13
24.07
9.44
27.00
f1 (ppm)

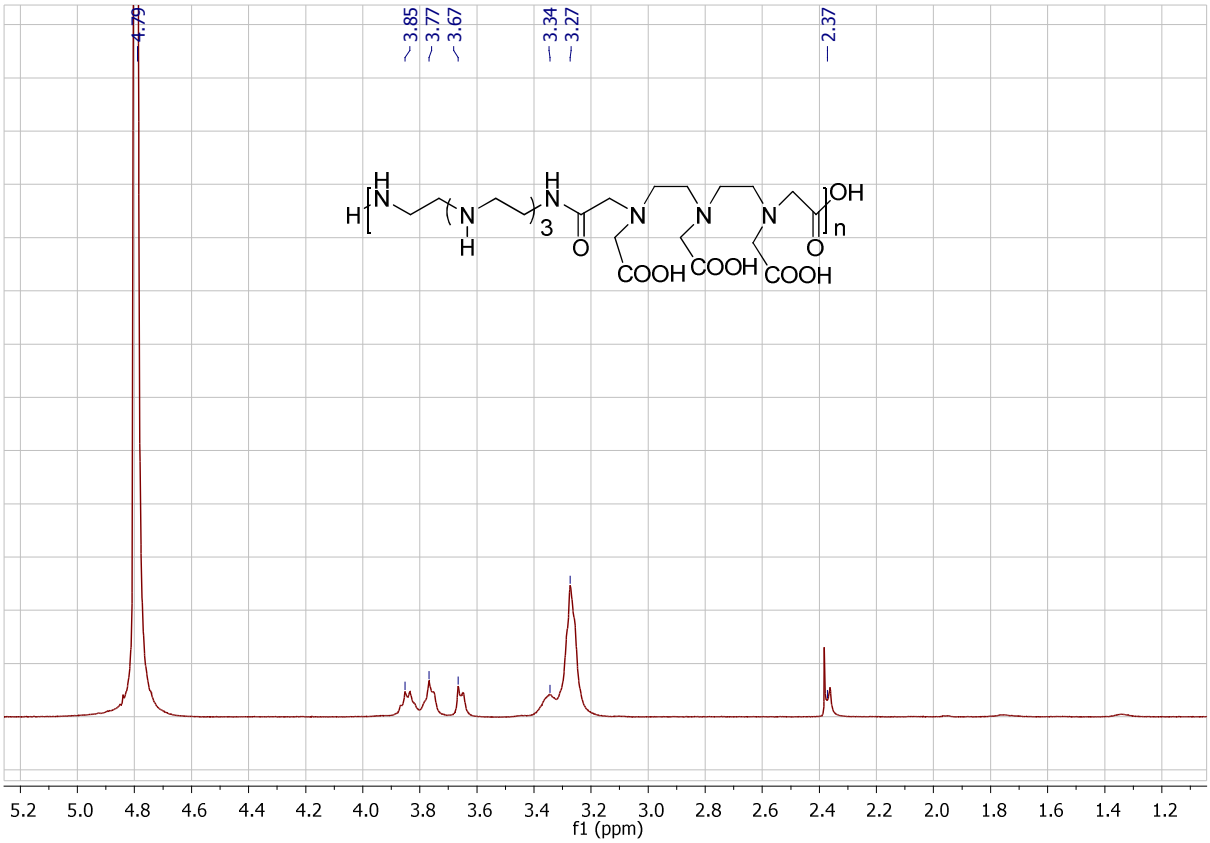
4.79
3.85
3.77
3.67
3.34
3.27
2.37
f1 (ppm)

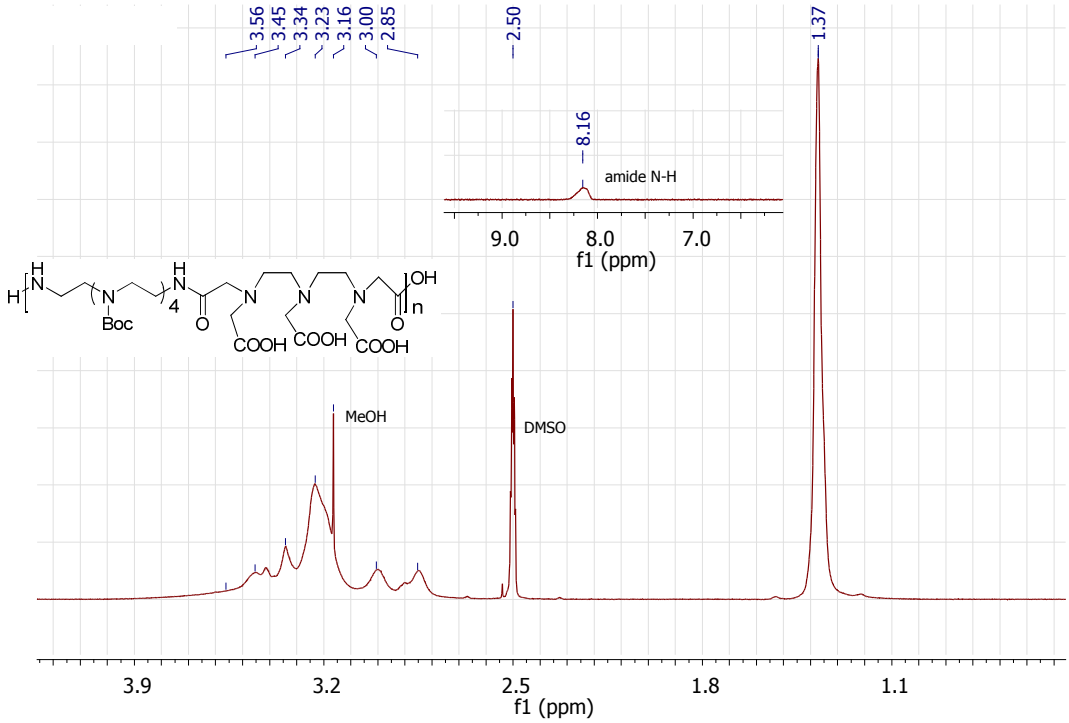
3.56
3.45
3.34
3.23
3.16
3.00
2.85
2.50
1.37
8.16
amide N-H
9.0
8.0
7.0
f1 (ppm)
Boc
COOH
COOH
COOH
OH
n
MeOH
DMSO
3.9
3.2
2.5
1.8
1.1
f1 (ppm)

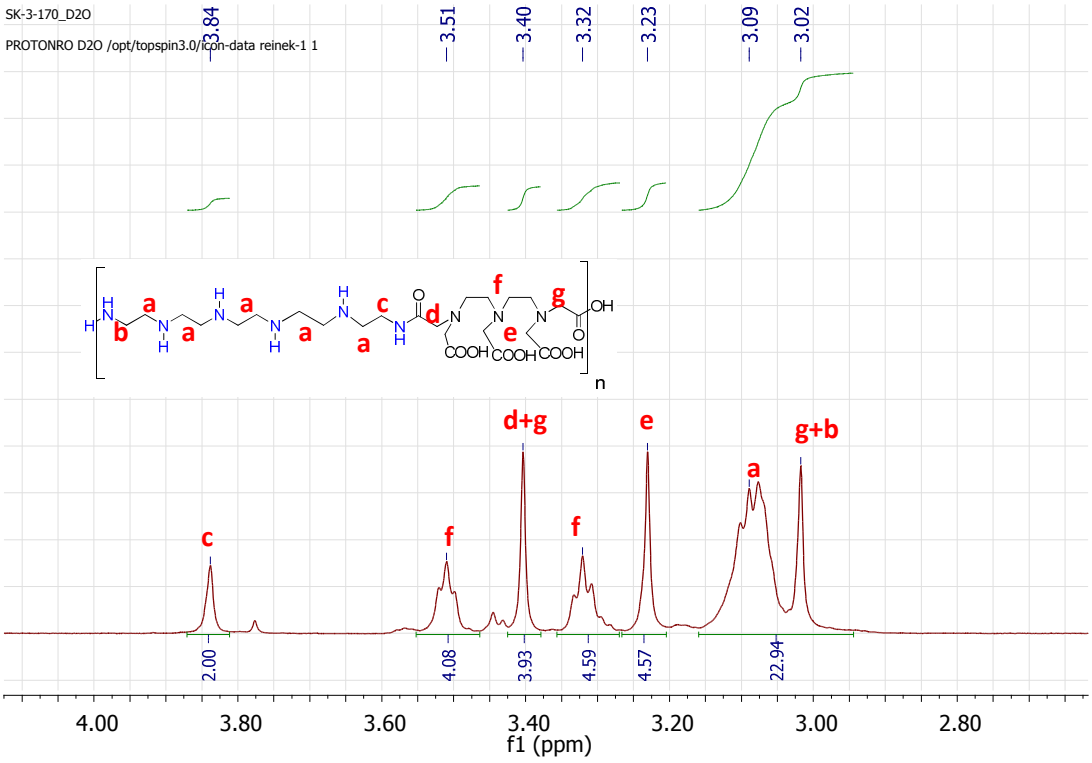
SK-3-170_D2O
PROTONRO D2O /opt/topspin3.0/icon-data reinek-1 1
3.84
3.51
3.40
3.32
3.23
3.09
3.02
a
b
c
d
e
f
g
COOH
COOH
COOH
OH
n
c
f
d+g
f
e
a
g+b
2.00
4.08
3.93
4.59
4.57
22.94
4.00
3.80
3.60
3.40
3.20
3.00
2.80
f1 (ppm)

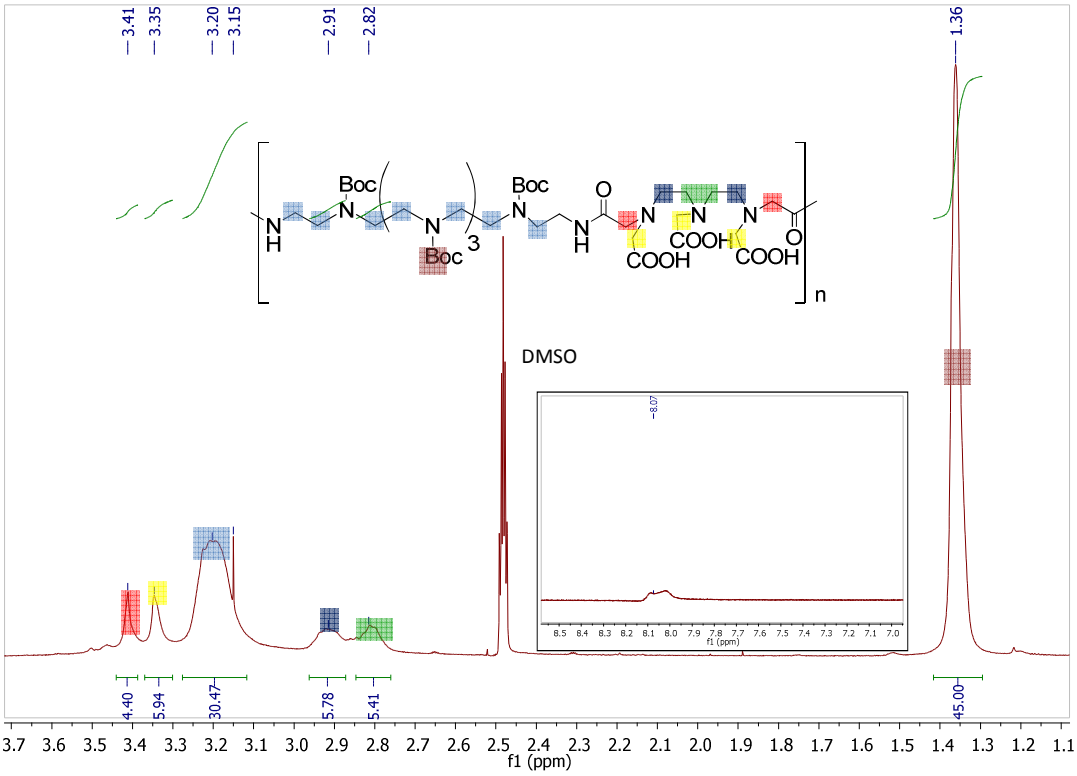
3.41
3.35
3.20
3.15
2.91
2.82
1.36
Boc
Boc
Boc
3
n
COOH
COOH
COOH
DMSO
8.07
4.40
5.94
30.47
5.78
5.41
45.00
f1 (ppm)

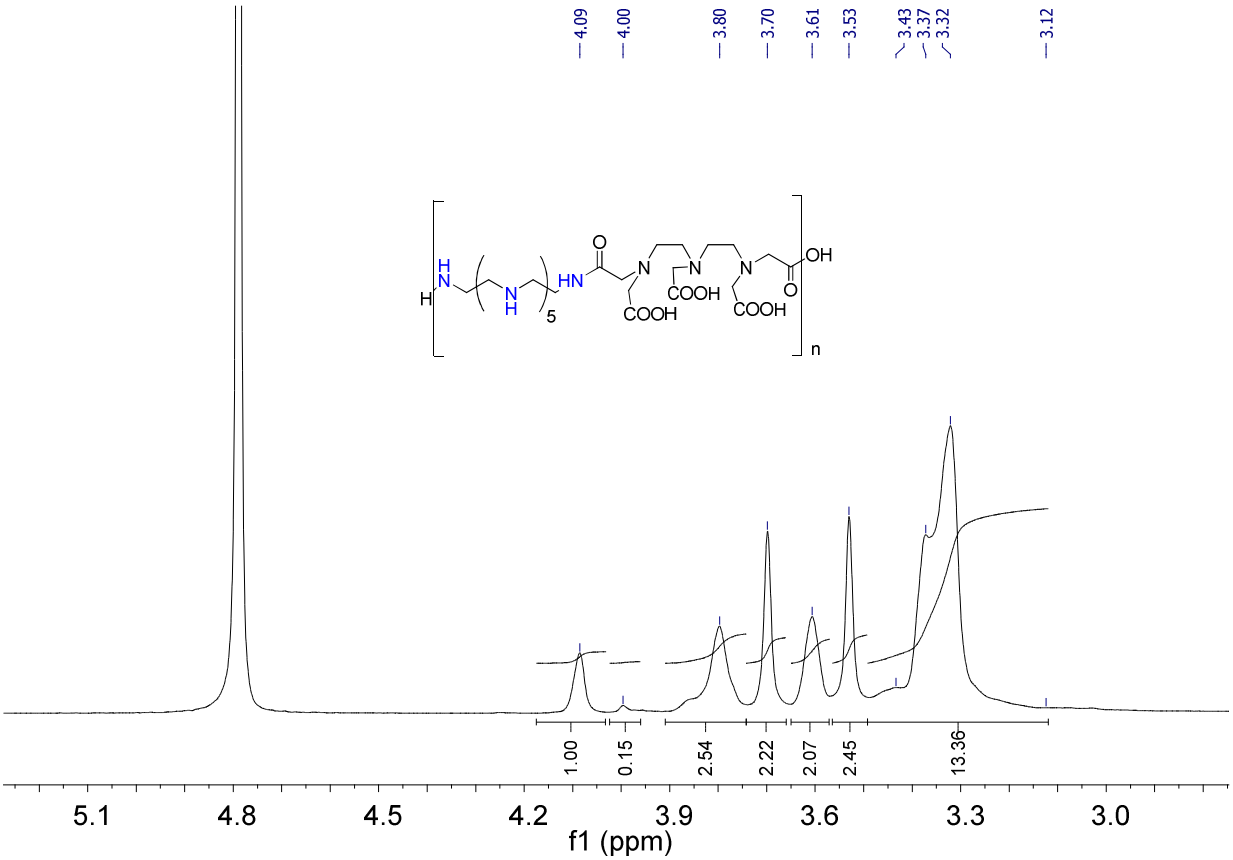
4.09
4.00
3.80
3.70
3.61
3.53
3.43
3.37
3.32
3.12
OH
COOH
COOH
COOH
5
n
1.00
0.15
2.54
2.22
2.07
2.45
13.36
f1 (ppm)

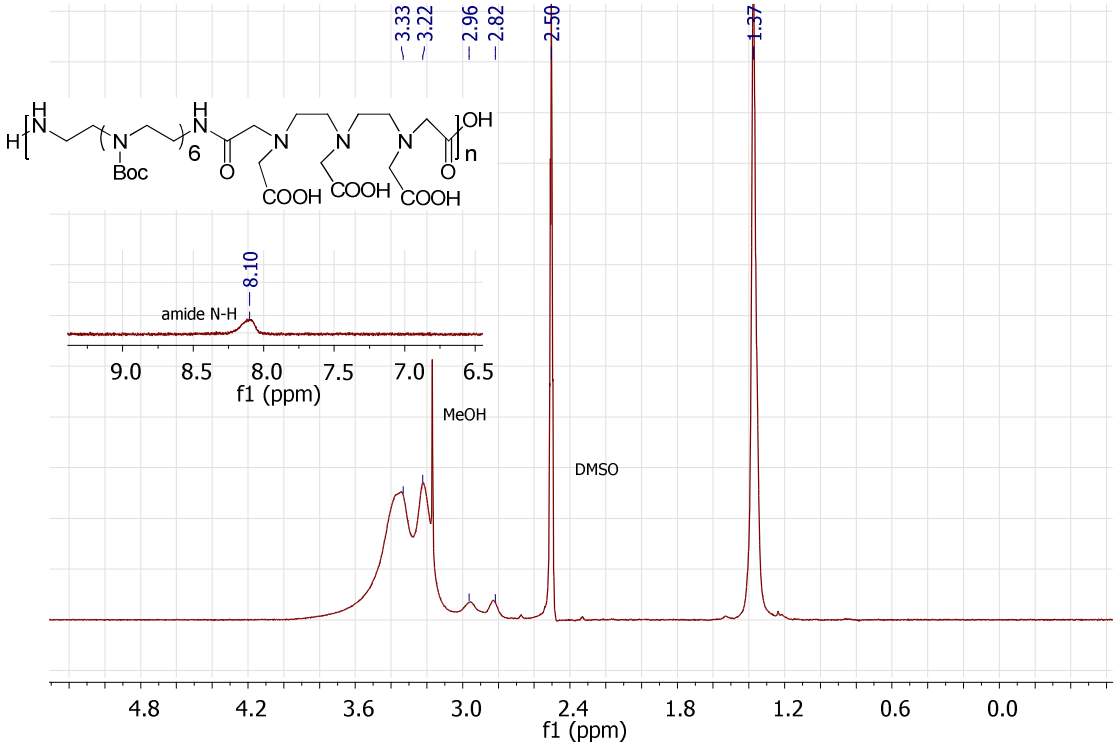
3.33
3.22
2.96
2.82
2.50
1.37
Boc
COOH
COOH
COOH
OH
n
8.10
amide N-H
9.0
8.5
8.0
7.5
7.0
6.5
f1 (ppm)
MeOH
DMSO
4.8
4.2
3.6
3.0
2.4
1.8
1.2
0.6
0.0
f1 (ppm)

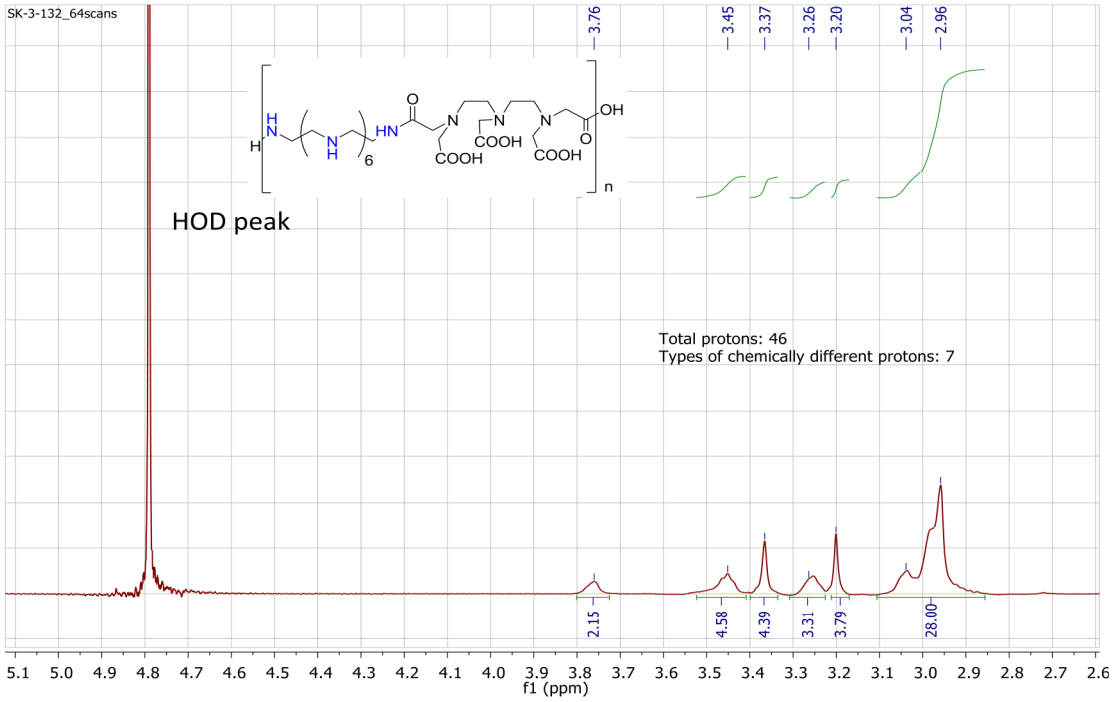
SK-3-132_64scans
3.76
3.45
3.37
3.26
3.20
3.04
2.96
HOD peak
Total protons: 46
Types of chemically different protons: 7
2.15
4.58
4.39
3.31
3.79
28.00
5.1
5.0
4.9
4.8
4.7
4.6
4.5
4.4
4.3
4.2
4.1
4.0
3.9
3.8
3.7
3.6
3.5
3.4
3.3
3.2
3.1
3.0
2.9
2.8
2.7
2.6
f1 (ppm)

Appendix B: Important ^{13}C NMR Spectra

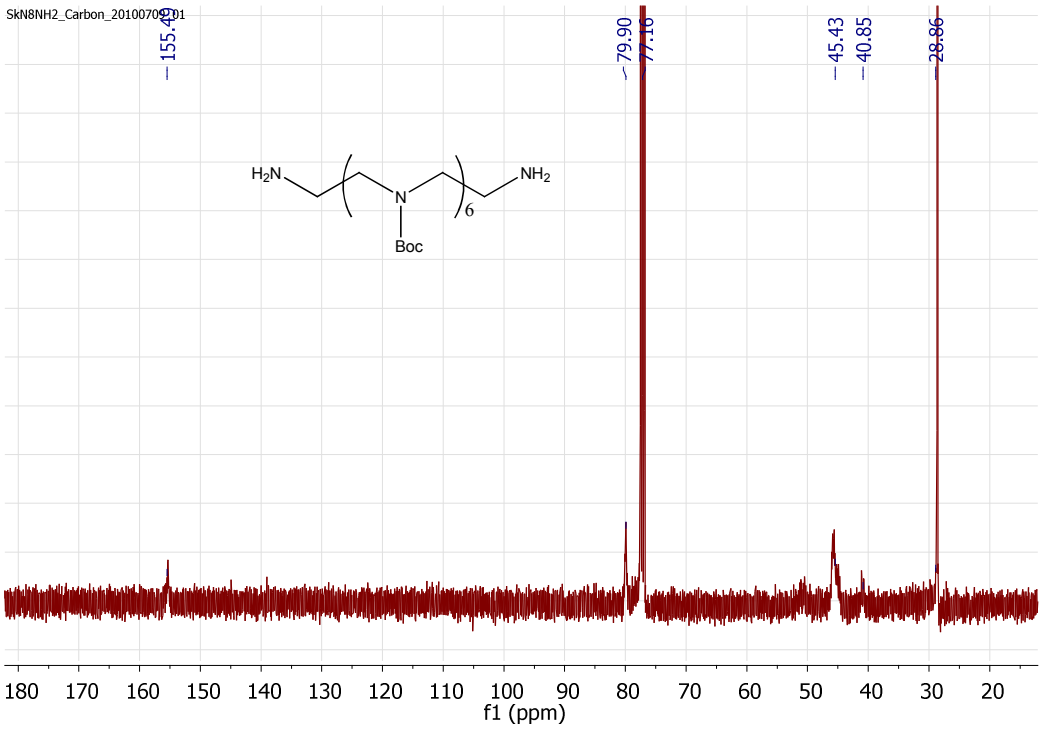
SkN8NH2_Carbon_20100709_01
155.49
79.90
77.16
45.43
40.85
28.86
H2N
NH2
N
6
Boc
180 170 160 150 140 130 120 110 100 90 80 70 60 50 40 30 20
f1 (ppm)

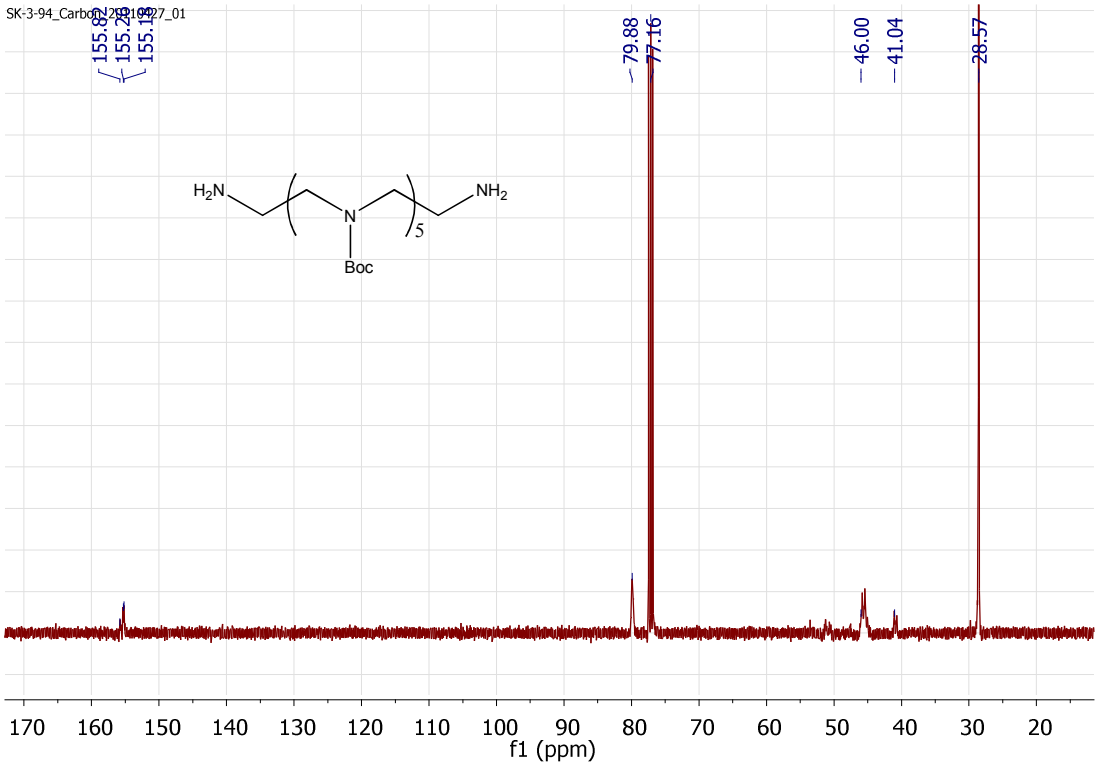
SK-3-94_Carbon_20101027_01
155.82
155.21
155.13
79.88
77.16
46.00
41.04
28.57
H2N
NH2
N
5
Boc
170 160 150 140 130 120 110 100 90 80 70 60 50 40 30 20
f1 (ppm)

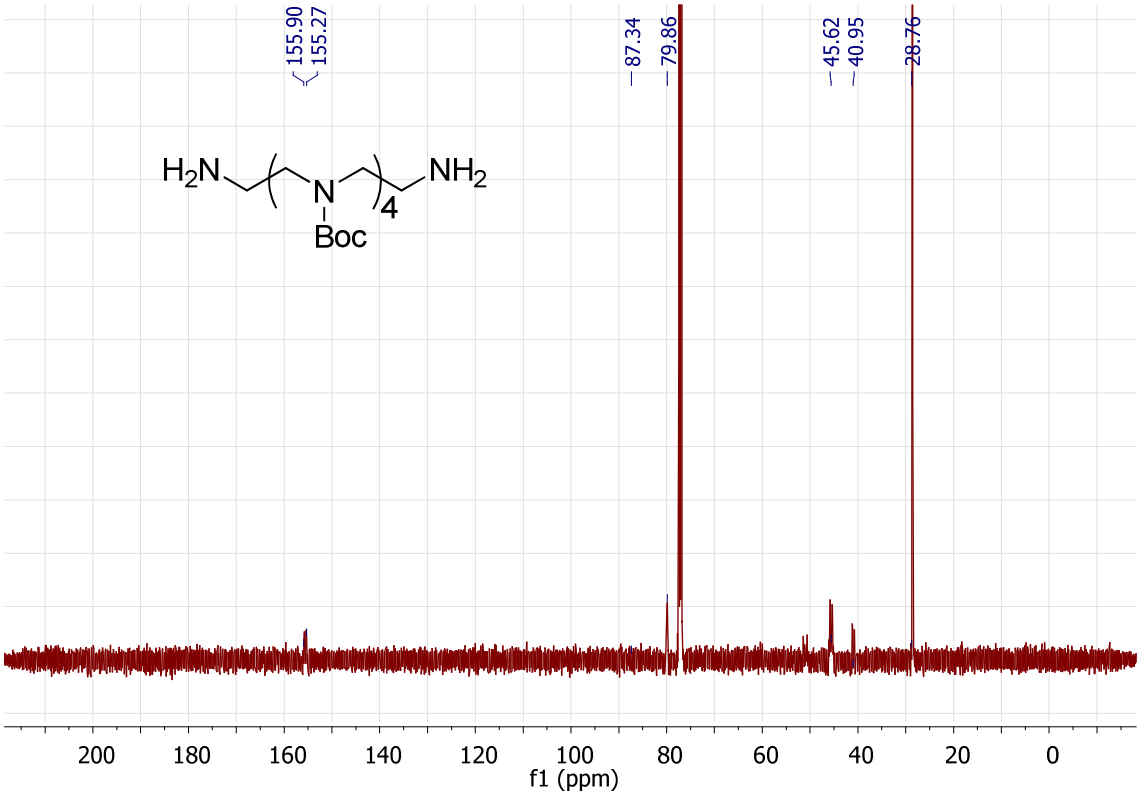
155.90
155.27
87.34
79.86
45.62
40.95
28.76
H2N
NH2
N
4
Boc
200
180
160
140
120
100
80
60
40
20
0
f1 (ppm)

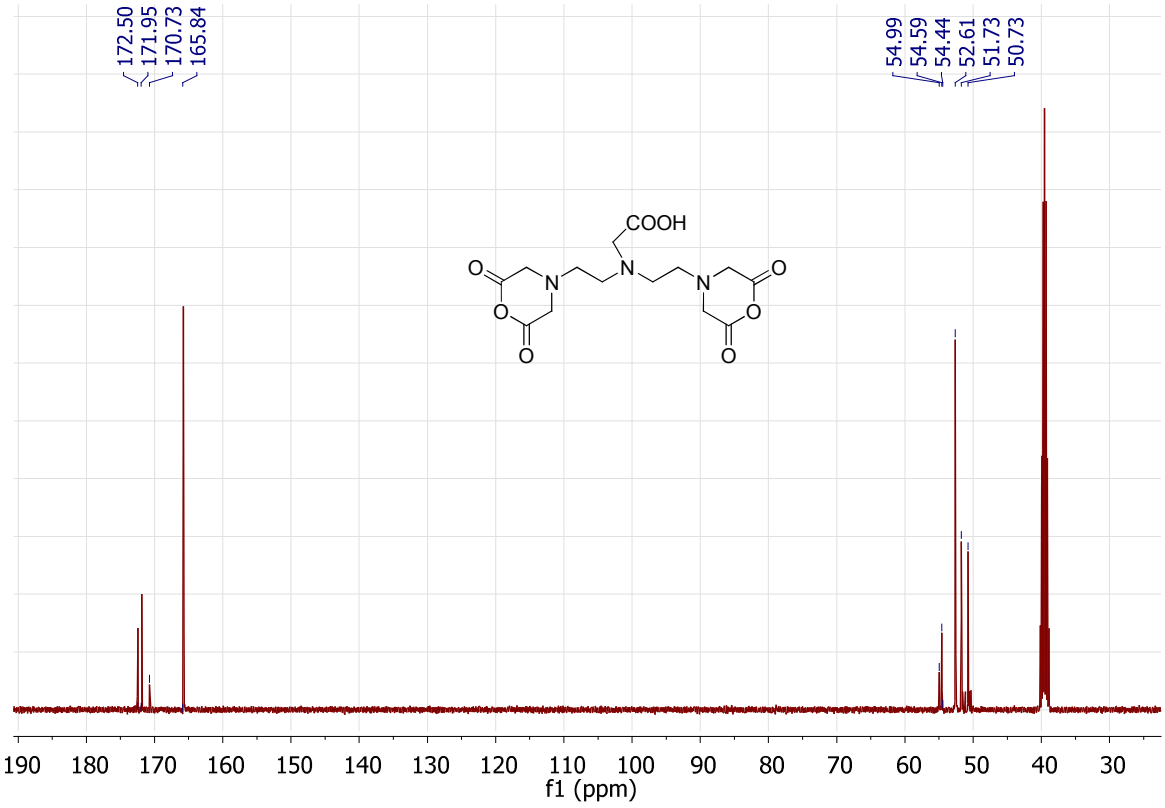
172.50
171.95
170.73
165.84
54.99
54.59
54.44
52.61
51.73
50.73
COOH
N
N
N
O
O
O
O
O
O
190
180
170
160
150
140
130
120
110
100
90
80
70
60
50
40
30
f1 (ppm)

Appendix C: Important LC-MS Spectra

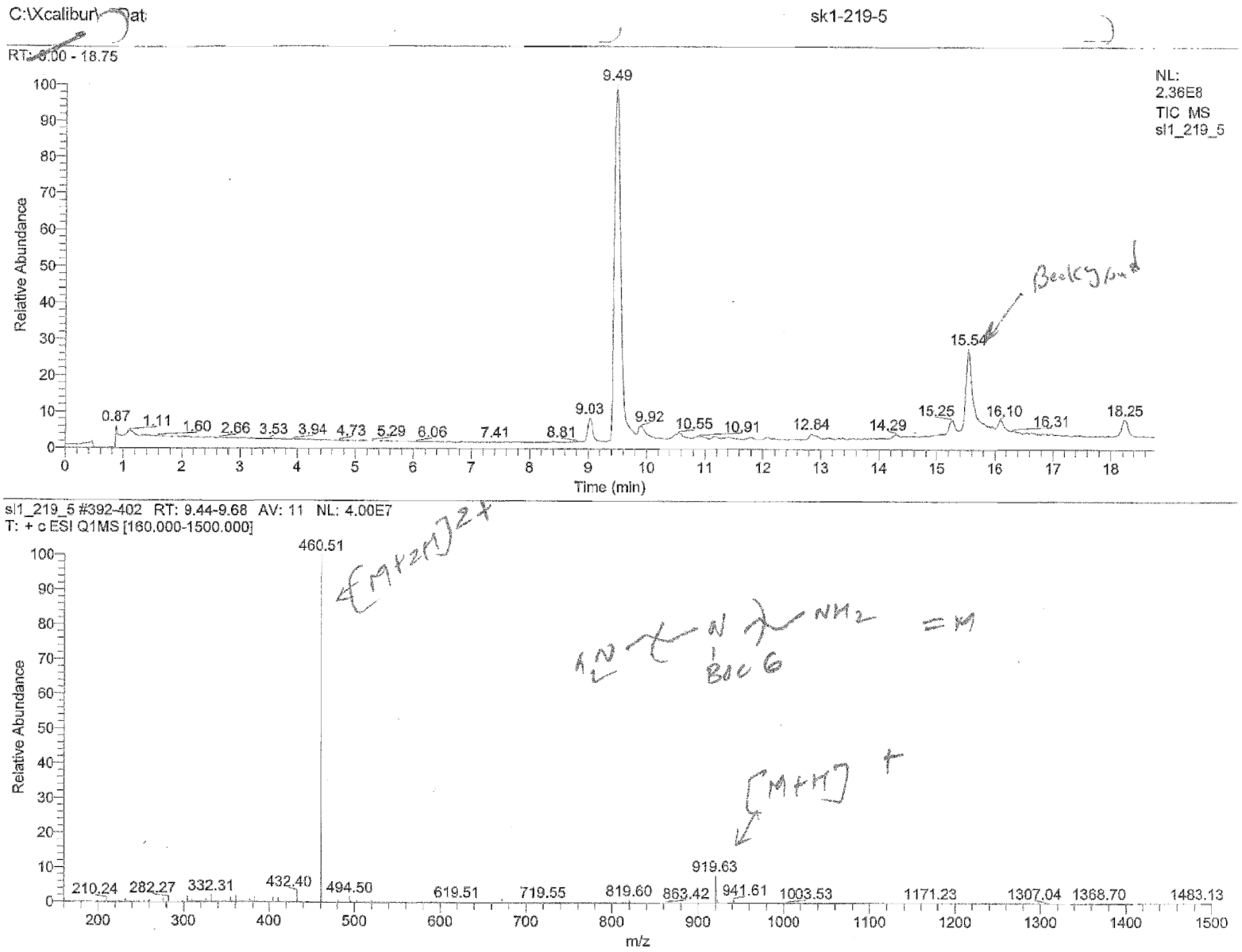
C:\Xcalibur\...\at
sk1-219-5
RT: 0.00 - 18.75
NL:
2.36E8
TIC MS
sl1_219_5
Relative Abundance
Time (min)
9.49
15.54
Background
0.87
1.11
1.60
2.66
3.53
3.94
4.73
5.29
6.06
7.41
8.81
9.03
9.92
10.55
10.91
12.84
14.29
15.25
16.10
16.31
18.25
sl1_219_5 #392-402 RT: 9.44-9.68 AV: 11 NL: 4.00E7
T: + c ESI Q1MS [160.000-1500.000]
460.51
[M+2H]2+
[M+H]+
919.63
210.24
282.27
332.31
432.40
494.50
619.51
719.55
819.60
863.42
941.61
1003.53
1171.23
1307.04
1368.70
1483.13
m/z

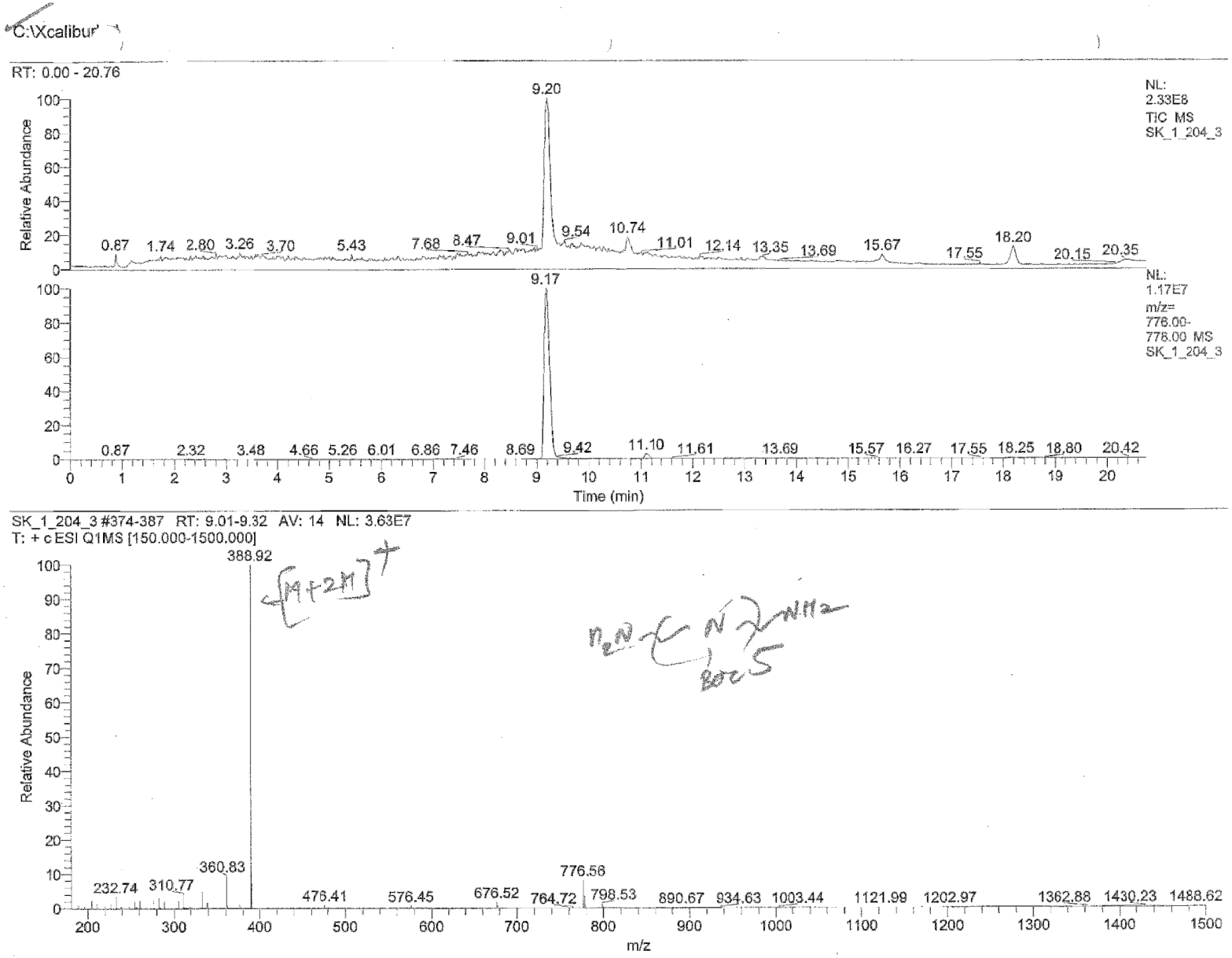
C:\Xcalibur
RT: 0.00 - 20.76
Relative Abundance
9.20
NL:
2.33E8
TIC MS
SK_1_204_3
0.87 1.74 2.80 3.26 3.70 5.43 7.68 8.47 9.01 9.54 10.74 11.01 12.14 13.35 13.69 15.67 17.55 18.20 20.15 20.35
9.17
NL:
1.17E7
m/z=
776.00-
778.00 MS
SK_1_204_3
0.87 2.32 3.48 4.66 5.26 6.01 6.86 7.46 8.69 9.42 11.10 11.61 13.69 15.57 16.27 17.55 18.25 18.80 20.42
Time (min)
SK_1_204_3 #374-387 RT: 9.01-9.32 AV: 14 NL: 3.63E7
T: + c ESI Q1MS [150.000-1500.000]
388.92
[M+2H]+
360.83
232.74 310.77 476.41 576.45 676.52 764.72 776.56 798.53 890.67 934.63 1003.44 1121.99 1202.97 1362.88 1430.23 1488.62
m/z

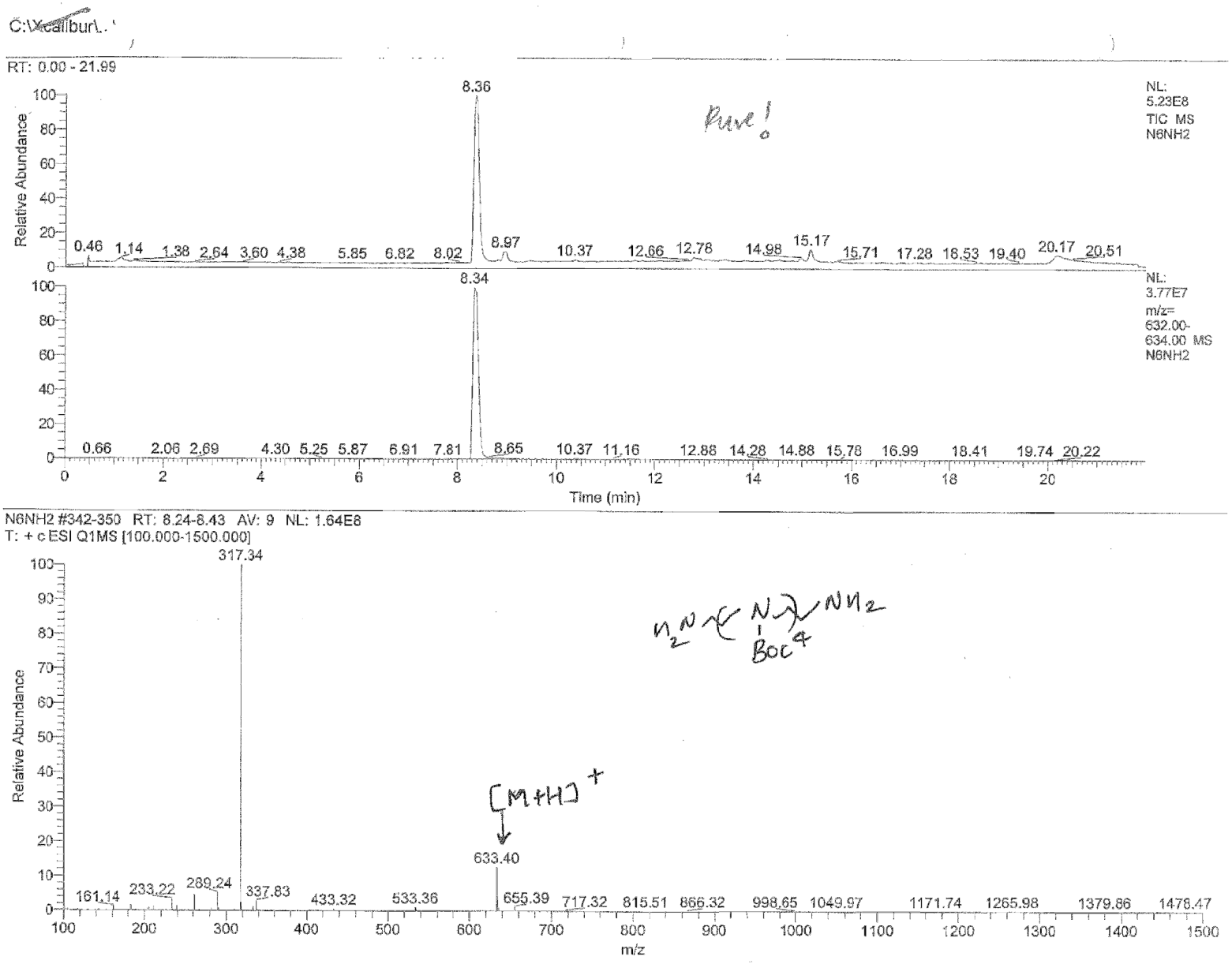
C:\Xcalibur\...
RT: 0.00 - 21.99
8.36
Pure!
NL:
5.23E8
TIC MS
N6NH2
Relative Abundance
0.46 1.14 1.38 2.64 3.60 4.38 5.85 6.82 8.02 8.97 10.37 12.66 12.78 14.98 15.17 15.71 17.28 18.53 19.40 20.17 20.51
8.34
NL:
3.77E7
m/z=
632.00-
634.00 MS
N6NH2
0.66 2.06 2.69 4.30 5.25 5.87 6.91 7.81 8.65 10.37 11.16 12.88 14.28 14.88 15.78 16.99 18.41 19.74 20.22
Time (min)
N6NH2 #342-350 RT: 8.24-8.43 AV: 9 NL: 1.64E8
T: + c ESI Q1MS [100.000-1500.000]
317.34
Relative Abundance
[M+H]+
633.40
161.14 233.22 289.24 337.83 433.32 533.36 655.39 717.32 815.51 866.32 998.65 1049.97 1171.74 1265.98 1379.86 1478.47
m/z